Universidade do Minho
Escola de Engenharia

Andreia Raquel Sampaio Faria

Eddy Current Angular Position Sensor for Automotive

fevereiro de 2022

Eddy Current Angular Position Sensor for Automotive
Andreia Raquel Sampaio Faria
UMinho | 2022

REPÚBLICA PORTUGUESA
CIÊNCIA, TECNOLOGIA E ENSINO SUPERIOR
FCT Fundação para a Ciência e a Tecnologia
NORTE2020
CENTRO 2020
ALENTEJO 2020
POCH
PORTUGAL 2020
UNIÃO EUROPEIA
Fundo Social Europeu

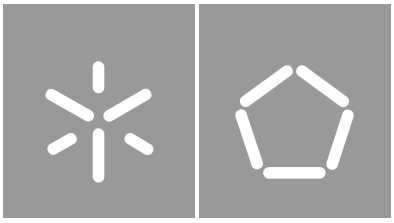

Universidade do Minho
Escola de Engenharia

Andreia Raquel Sampaio Faria

Eddy Current Angular Position Sensor for Automotive

Tese de Doutoramento
Programa Doutoral em Líderes para Indústrias Tecnológicas

Trabalho efetuado sob a orientação do
Professor Doutor Jorge Miguel Nunes dos Santos Cabral
Doutor João Gaspar

fevereiro de 2022

Acknowledgement

Este documento apresenta os resultados de muitos anos de trabalho e dedicação, com o apoio incondicional de várias pessoas e instituições. Quero começar por agradecer ao Professor Luís Alexandre Rocha, por me desafiar a apostar num projeto como este. Apesar de não me ter acompanhado fisicamente até ao final, sinto que sempre tive a sua orientação. Em especial quero agradecer ao meu orientador Jorge Cabral, pela sua ajuda, dedicação, por me fazer acreditar que eu era capaz mesmo apesar de todas as adversidades. Deixo também um agradecimento especial ao professor Luís Silvino Marques, pela sua prontidão e disponibilidade em me ajudar com os conceitos físicos do modelo desenvolvido. Quero agradecer também ao Filipe Serra Alves e ao meu co-orientador João Gaspar por todos os contributos ao longo deste percurso.

Quero ainda agradecer à Fundação para a Ciência e Tecnologia (FCT) pela bolsa de doutoramento que me foi atribuída (PD/BD/128142/2016), sem a qual este trabalho não poderia ter sido realizado, e ao programa MIT Portugal pela oportunidade que me concedeu em realizar o programa doutoral LTI. Assim como ao centro Algoritmi pelo apoio na investigação.

E quero deixar um agradecimento especial aos meus familiares e amigos, sem eles ultrapassar todas as frustrações, desafios e desânimos teria sido muito mais desafiante. Quero começar por agradecer ao meu marido, José Neiva, por sempre me ter compreendido e me apoiado em todas as etapas deste doutoramento. Quero também agradecer à minha mãe e ao meu pai, por todos os concelhos e por sempre acreditarem que eu era capaz. Obrigada à minha companheira desta grande jornada, Flávia Barbosa, foi fantástico o que vivemos e superamos juntas. Obrigada aos meus colegas do laboratótio Vasco Lima, Rui Machado e Luís Vale pela paciência, e por sempre arranjarem um espaço na agenda para me ajudar. Obrigada à minha couch Carminda por sempre me ajudar a ter uma visão mais completa das coisas e a me focar no que realmente queria para mim. E termino com um agradecimento ao meu irmão Rafael, pelas nossas conversas pela noite fora, por me ouvires e pelo teu carinho e apoio incondicional.

Andreia Raquel Sampaio Faria

February 14th, 2022

STATEMENT OF INTEGRITY

I hereby declare having conducted this academic work with integrity. I confirm that I have not used plagiarism or any form of undue use of information or falsification of results along the process leading to its elaboration.

I further declare that I have fully acknowledged the Code of Ethical Conduct of the University of Minho.

Resumo

Os sensores angulares usados em aplicações automóveis, requerem uma boa resolução, fiabilidade, baixa manutenção, baixo custo de produção e capacidade de trabalhar sob condições adversas. Devido a estes requisitos, os sensores mais utilizados são os magnéticos, indutivos e magneto-indutivos. Outro fator crítico é a dimensão do sensor, quanto mais reduzido e compacto, maior é o número de aplicações em que pode ser aplicado. No caso dos sensores magneto-indutivos e indutivos, uma forma de reduzir o seu tamanho é através do uso de a bobines planares impressas em placas de circuito impresso (PCB). Estas, para além de mais compactas, conseguem também reduzir os custos de produção, otimizar a repetibilidade e assemblagem, e permitir que o seu desenho seja facilmente adaptado às suas aplicações.

No desenvolvimento de sensores indutivos, obter a indutância das bobinas, que funcionam como elemento transdutor, é essencial e desafiador no caso de bobinas planas. Atualmente, há duas abordagens no estado da arte: fórmulas de aproximação (para geometrias regulares), e simulações de modelos de elementos finitos (FEM). As simulações são demoradas e recorrem a ferramentas de software dispendiosas e que exigem muitos recursos computacionais. Esta tese tem como objetivo desenvolver uma ferramenta de cálculo analítico para obter a indutância de bobinas planas genéricas, reduzindo o tempo de desenvolvimento. A ferramenta possibilita ainda o cálculo da interferência que um alvo planar condutivo tem na indutância da bobine, tornando assim possível obter a resposta de um sensor indutivo baseado em eddy currents durante a sua fase de desenvolvimento.

Esta tese, além de detalhar o desenvolvimento da ferramenta mencionada, também descreve todos os processos de validação implementados, através de simulações FEM e testes experimentais. A metodologia proposta foi aplicada com sucesso no desenvolvimento de um sensor de posição angular automotivo baseado em eddy currrents. Foi possível comprovar que a precisão da ferramenta desenvolvida está de acordo com as metodologias usualmente utilizadas, com a vantagem de ser mais rápida e económica.

Palavras-chave: Indutância, bobine planar, currentes de eddy, sensores de posição angular.

Abstract

Angular sensors used in automotive applications require good precision, reliability, low maintenance, low production costs and the ability to work in harsh conditions. Due to these requirements, magnetic, inductive and magneto-inductive sensors are preferred and are used in current generations of automotive angular position sensors. The size of the sensors is another relevant factor in the development of new solutions. The smaller and more compact, the larger the number of applications in which they can be applied. In the case of magneto-inductive and inductive sensors, one way to reduce their size is to use planar coils printed on printed circuit boards (PCBs). These, in addition to occupy a smaller volume when compared to solenoids, also reduce production costs and optimize repeatability and simplify assembly.

When developing inductive sensors, knowing the required inductance value of its coils is essential and this task can be challenging in the case of planar coils. Currently, two approaches are used to calculate the inductances of planar coils. When the coils have regular geometry approximation formulas are used, configuring some parameters. When they have irregular geometry or a more accurate result is desired, simulations using finite element methods (FEM) are chosen. These simulations have the disadvantage of being time-consuming, requiring expensive software applications and a huge computing resources. In view of the budget and the reduction of development time, this thesis provides an analytical calculation tool for the inductance of generic multi-layer planar coils. In this way, it is possible to develop dedicated applications in reduced time. The tool also allows to calculate the interference that a planar conductive target, of arbitrary geometry, can have on the coil inductance. Thus, it is possible to obtain the response of an inductive sensor based on eddy currents during its development phase.

This thesis, in addition to detailing the development of the aforementioned tool, also describes all the validation processes implemented using FEM simulations and experimental tests. The proposed methodology was successfully applied in the development of an automotive angular position sensor based on eddy currents. It was possible to prove that the precision of the developed analytical tool is in concordance with the methodologies usually used, with the advantage of being faster and open source.

Keywords: Inductance, planar coil, eddy currents, angular position sensor.

Table of Contents

List of Figures

List of Tables

List of Acronyms

AMR	Anisotropic Magnetoresistance.
APS	Angular Position Sensor.
CAGR	Compound Annual Growth Rate.
EMC	Electromagnetic Compatibility.
EMI	Electromagnetic Interference.
FEM	Finite-Element Method.
GMR	Giant Magnetoresistance.
HMIExcel	Human Machine Interface Excellence.
INNOVCAR	INNOVATIVE Car HMI.
MTJ	Magnetic Tunneling Junction.
PCB	Printed Circuit Board.
RF	Radio Frequency.
RVDT	Rotary Variable Differential Transformer.
TMR	Tunneling Magnetoresistive.
VR	Variable Reluctance.

Chapter 1

Introduction

The need to interact with the real world, requires the development of input transducers, also known as sensors. They are used in several industries, from aerospace, automotive, electronic, healthcare, industrial, to entertainment, security, among others. In addition, with the implementation of Industry 4.0 and the increase of the levels of security and communication between systems, it is expected that sensors will be used in any device or instrument developed.

The main goal of this thesis was to develop an analytical tool to potentiate the innovative application of eddy current's technology to automotive position sensor, with a use case being the Angular Position Sensor (APS). Currently to determine the inductances of planar coils in the presence of a conductive plate simulations of Finite Element Methods (FEM) are used. This approach has the disadvantage of being time consuming and requires expensive and high computational resources. The tool that is been proposed is focused on mitigating the disadvantages of both methodologies, offering an analytical solution versatile, fast, user friendly and that does not require high-computational resources.

In order to understand and quantify the potentiality of eddy current technology, it is important to clarify and explore how the position sensors market is growing, and how the automotive industry is positioned in this market and in which way it is investing in this type of sensors. It is also important to know the advantages of an eddy current sensor over other existing automotive position sensors that use a different physical principle. This chapter introduces the relevance of this study, which research questions it must answer, and describes how the information is compiled in this document.

In the next section the trends in the global and automotive APS markets are detailed, comparing these predictions with the quantity of these sensors produced annually by Bosch Car Multimedia Braga, Portugal. Section 1.2 introduces the main preferences by the automotive industry for new APS sensors and the current technologies in use. Section 1.3 explains the motivation to develop an analytical tool for an

eddy current sensor, the scope of the thesis, its research questions, main objectives, and methodologies adopted to achieve its main goal. Section 1.4 presents the thesis contributions and the publications made during the research, and Section 1.5 details the structure of this thesis.

1.1 Sensor Market Trend

The growth of the different markets, for example at the level of monitoring and automation of production processes, and at the level of the intelligence and communication of the devices with the surrounding systems, has contributed to the increase in investment in the area of sensors. Even the legislation in some countries, for example regarding the safety and environmental impact of vehicles, has contributed to this demand. According to [1.1], since 2017, the global sensor market has grown significantly. In 2017 it was valued at about $135.5 billion and in 2018 at around $152.2 billion, being expected to reach $283.4 billion in 2023. As depicted in Figure 1.1 [1.1], until 2023, it is expected a market growth of all types of referenced sensors, which concerns the particular case of position sensors a Compound Annual Growth Rate (CAGR) from 2018 to 2023 of 9.2% is predicted. [1.1].

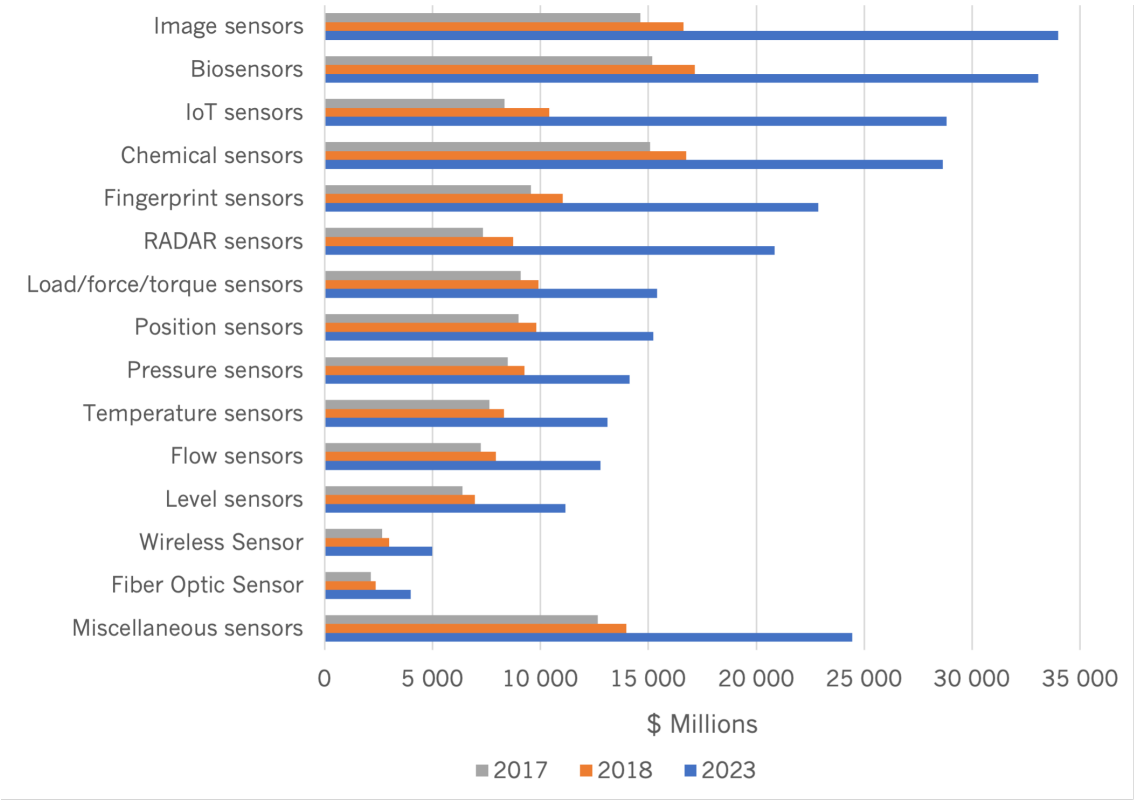

Figure 1.1: Global market for sensors, by type of sensor,2017-2023 ($ Millions) [1.1].

Based on the information detailed before, it is clear the value of the position sensor's market. However, there are several types of position sensors, and it becomes relevant to understand which category could result in a good investment. Inside the category of position sensors there are sensors that detect the presence of an object, called proximity sensors, and others that measure the distance to an object, known as displacement sensors. The latter can be further classified as linear or angular, depending on their ability to detect position changes. Generally, according to the reports from BCC Research [1.1], [1.2], position sensors are classified as:

- Linear displacement sensors;
- Proximity sensors;
- Rotary/angular position sensors;
- MEMS position sensors;
- Other miscellaneous types of position sensors.

According to the graphic of Figure 1.2 [1.1], it can be concluded that MEMS position sensors, linear displacement sensors and rotary position sensors, are the ones with the higher market value. It is expected that rotary position sensors will reach over $2.970 billion by 2023 from almost $1.83 billion in 2017 [1.1].

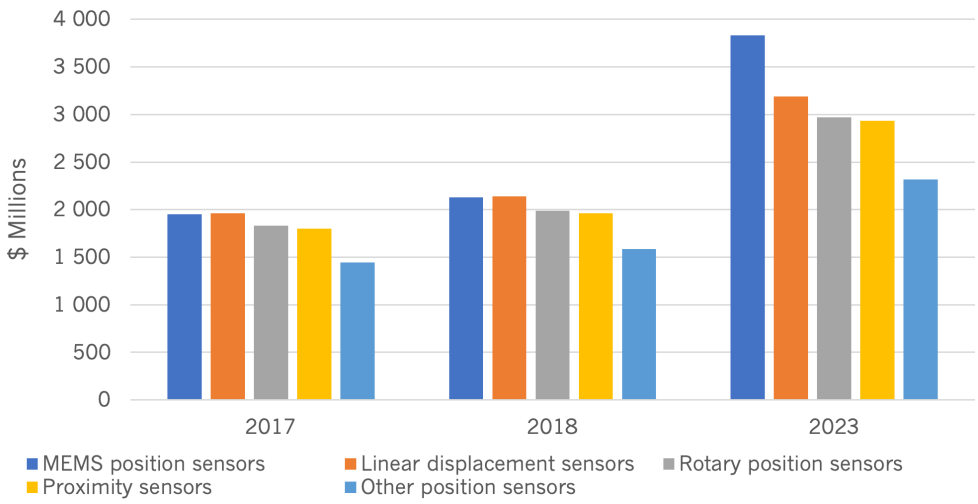

Figure 1.2: Global market for position sensors, by type of sensor,2017-2023 ($ Millions) [1.1].

With the previous information, it can be concluded that developing new angular/rotary position sensors is well aligned with the market trends. However, it makes sense to analyse which industries are more interested in this type of sensors in order to validate completely the investment in this development.

There are many industries, from production to manufacturing, that require position sensors in large quantities. Although, through the analysis of Figure 1.3 [1.2], it becomes explicit that the automotive sector is the main market for position sensors. Despite that, the sectors that are expected to have greater value growth than the automotive sector (CAGR of 9.1%) are the medical with a predicted CAGR of 10.7%, and the machine tools sector with 9.3% CAGR [1.2]. Having this significant difference between the automotive market and the rest in consideration, it makes it the preferred market for the sensor under development.

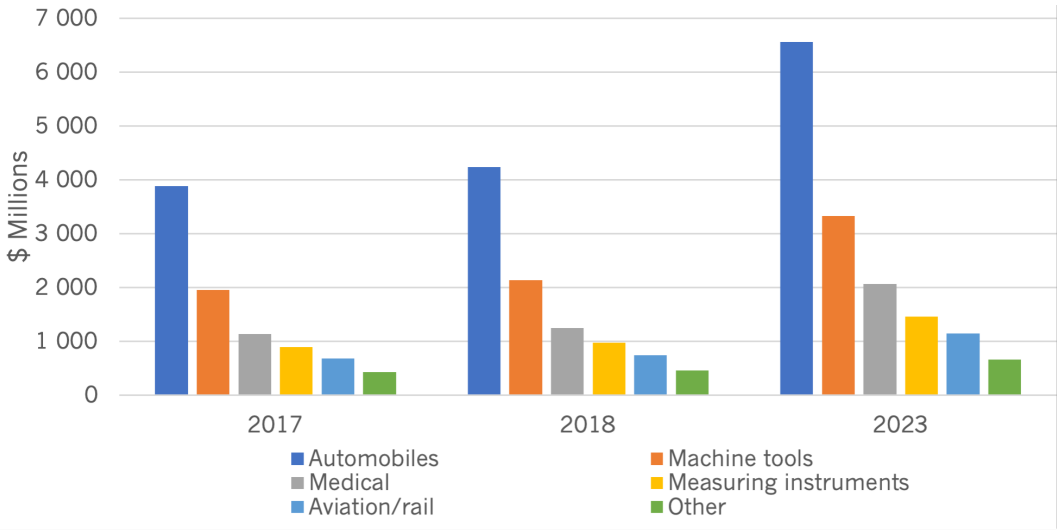

Figure 1.3: Global market for position sensors applications, by type of sensor,2017-2023 ($ Millions) [1.2].

This thesis was developed within the scope of a research project in partnership with the company Bosch Car Multimedia. So, to verify the trends identified by the reports mentioned before, the company was asked about its annual values for the production of angular position sensors. Accordingly to data provided by Bosch Car Multimedia Braga, around 1.7 million angular position sensors are produced every year.

1.2 Preferences for new automotive APS

According to [1.3], new angular position sensors should combine the following criteria: measure mechanical angles; be contactless; offer immunity to external electromagnetic fields; reduced need for external

components; target costs (comparing with the current approaches); high accuracy and robustness; calibration free (ready to use); and be suitable for more automotive applications.

In automotive applications, there are angular and linear position sensors working within displacements ranges from less than 1 micron to more than 200 millimeters, however it becomes relevant to clarify that the displacement working range for angular position sensors under development is between 0.5 mm and 2.0 mm. This include sensors based on potentiometer, Anisotropic Magnetoresistance (AMR), optical encoder, and Hall-effect [1.3]. The potentiometers are the most used due to their lower cost, simplicity, immunity and linearity, despite their measurements being made by physical contact, having lower accuracy and being limited by its physical size in the range of the measurement. Concerning enconders, the position sensing can be done through different physical methods, it can be of contact (mechanical) or non-contact (optical, magnetic, inductive) also, they can be incremental encoders or absolute position encoders. In general, depending on the type of encoder chosen and the sensing method selected, magnetic and optic sensing methods end up being the most preferable since they offer more robustness. However, an ordinary disadvantage to all type of encoders is that to achieve higher resolution its size has to be increased. Regarding to magnetoresistive (AMR, Giant Magnetoresistance (GMR) and Tunneling Magnetoresistive (TMR)) and Hall-effect sensors, both are magnetic belonging to the category of non-contact devices. The robustness of the magnetic sensors and their immunity to environmental particles, allow them to overcome the disadvantages of optical sensors. However, magnetic sensors are not adequate for harsh impact applications, due to magnets brittleness, and their readings can be perturbed by external magnetic fields. The main advantage of Hall-effect sensors is their simplicity, making them cheap, small and compatible for a lot of applications that do not require highly accurate measurements. Magnetoresistive sensors are similar to the Hall-effect sensors. However, in addition to detecting the difference in field strength they also detect changes in field directions. The magnetoresistive effect has the particularity of just occur in a particular range of materials, often ferromagnetic.

Considering the focus criteria for new angular position sensors and the various characteristics of the sensor's technologies usually used, this thesis proposes to the study and development an APS based on eddy currents. A sensor with this technology can be classified as an inductive sensor, offering the same advantages of this type of sensors, being a non-contact device, and capable of working in harsh conditions, i.e., environments with dust, water, shocks, vibrations or harsh electromagnetic fields. Currently, inductive sensors have not been used in the automotive sector due to their weight and dimensions of their traditional implementations. As new inductive sensors use planar coils printed in the sensor circuits Printed Circuit Board (PCB) instead of the traditional solenoids, they can offer a solution that is more compact, robust,

and with a fabrication process with lower costs and higher reliability. When compared to potentiometers it has the advantages of being contactless, and to Hall-effect and magnetoresistive sensors it has lower costs since it does not require neither rare nor expensive materials, as e.g. permanent magnets.

Taking into account the sensor's requirements for automotive, and the problems/challenges of the current solutions, it became clear that eddy current technology has a huge potential to be used in automotive application sensors. The interest in this type of applications is growing in the automotive industry, and proof of this are the increasing number of patents recently submitted. However, as there is a growth in the amount of products on the market that use this technology, it highlights the potential and relevance of this research.

1.3 Motivation

In 2013, University of Minho and Bosch Car Multimedia Braga started a research and technological development partnership with the purpose of obtaining an answer to some scientific and technological challenges proposed by Bosch. The first research project, Human Machine Interface Excellence (HMIExcel), was dedicated to advanced multimedia solutions for automobiles in the man-machine relationship. The master's degree of the author was integrated one of the research lines of the HMIExcel project. After that, the author also integrated a research line of the following program, called INNOVATIVE Car HMI (INNOVCAR). This program focused in acquiring knowledge that would become in world innovations in the car solutions of the future. In both projects the author performed electromagnetic analysis of two automotive APS, through Finite-Element Method (FEM) simulations, and studied its behavior, for example in the presence of external magnetic interference and conductive plates. Based on the results, Bosch showed interest in improving the performance of position sensors based on the eddy current effect. This technology has the capability of developing sensors with lower costs than current solutions, which is an asset in the automotive market.

With the research work developed by the author, it became clear that the process of drawing the coils, import them to the FEM software, perform the FEM model and simulate it for all the case scenarios stipulated takes a long time and requires significant computing resources. So, in order to optimize this process, the author and her supervisors had the idea of developing an analytical model that would allow simulating the behavior of a planar coil when in proximity of a metallic target. Through the development of a generic tool, it will be possible to optimize the development of any sensor based on eddy currents, which uses planar coils with or without metallic plates. Thus, with all the author's background and preferences,

this was considered by the author an interesting and defying challenge. The author started a thesis where the main objective is to develop a tool that would be able to calculate the inductance of planar coils in the presence of a metallic target. With it the author will not just understand the physics behind the technology, but also how they can accelerate the designing process of a sensor based on this technology.

Moreover, working in the front line of automotive sensors development is another of the working goals of the author, since the author enjoys the matching of the industrial world with the product development field. Because developing an innovative sensor by itself does not guarantee that it will succeed in the market, it must be aligned with the market needs, considering performance, costs, and time to market. For the author, this is one of the most defying things about engineering, and having experience in this field will be relevant in the business world.

1.3.1 Research Questions and Objectives

As described previously, the development of eddy current sensors with planar coils is currently a very time-consuming and costly process in terms of software and computational resources. Thus, in order to solve this problem, this thesis proposes an analytical tool to simplify and accelerate the design of this kind of sensors. The main objective of this tool is to be able to calculate the inductance of planar coils in the presence of conductive targets in a faster, simple and cheapest way.

Considering the problem described, this PhD thesis proposes to answer the following research questions:

- **RQ1:** What are the methods more adequate to calculate self and mutual inductances of planar coils for an eddy current based automotive sensor?
- **RQ2:** How can the performance of the several planar coil designing methodologies be compared?
- **RQ3:** What are the main challenges in the designing phase of an eddy current based automotive position sensor and how can they be targeted?
- **RQ4:** Can an eddy current sensor be optimally designed?

So, in order to achieve the tool under proposal, this thesis aims to address several objectives:

- **O1:** Review of the state-of-art of the technologies used in angular position sensors, highlighting their strengths and weakness.
- **O2:** Review the current approaches to simulate and calculate inductance of planar coils.
- **O3:** Implement an analytical method to calculate self and mutual inductance of planar coils.

04: Evaluate the proposed tool within the existing state-of-the-art tools.

05: Implement the best approach of the developed method to the calculation of the interference of a target on the coil's inductance.

06: Assess the proposed tool with FEM simulations and experimental measurements, for the case where planar coils are in the presence of a conductive target.

07: Compare the performance of the tool implemented with the currently used in the development of an automotive eddy current angular position sensor.

1.3.2 Research methodology

In order to organize and align the investigation process of this thesis to answer the research questions and objectives, the following research methodologies were defined:

RM1 - State-of-art of the technologies used in automotive position sensors: In order to better understand the position of eddy current technology in relation to other technologies that exist in the position sensor market, a study of the state-of-the-art of the different technologies used in position sensors was carried out. In this way, it became clear the preferable areas of application for each type of technology, its working requirements, strengths, and weakness. With the knowledge gained from this research, it was possible to have a wide overview of the APS market and identify the position of the eddy currents technology on this market. It will also allow to fulfill the research objective **01** and to have part of the information needed to answer the research question **RQ4**.

RM2 - Review of planar coil inductance calculation methods: Accordingly to the information collected from **RM1**, during the development of a sensor based on eddy currents technology, one of the critical aspects identified is the design of its planar coils. Defining the geometry and calculating the inductance of this type of coils can be quite challenging and time-consuming considering its requirements. Therefore, it became relevant to optimize this process since it will be able to potentiate the appliance of this technology in the APS market. Thus, to accomplish that, a study on the approaches commonly used to calculate the inductance of planar coils printed in PCB was carried out. With this, it will be able to compile and compare the limitations and strengths of each of the methods usually used, understand in which type of applications they are used, and what are the selection criteria of the method to be used. With

this knowledge, it will be possible to identify the window of opportunity for a more optimized approach and to identify which needs must be met. This study will allow accomplishing the objective **O2**, and answering the research question **RQ1**, and partially **RQ2**.

RM3 - Implement the analytical model: With all this information and requirements identified for the inductance calculation method for planar coils, the development and implementation of the analytical methods can start using the MATLAB®software. This methodology was divided into two approaches. One is dedicated to calculating the self-inductance for single and multi-layer planar coils, and the other is for the total inductance of a planar coil in the presence of a metallic target. This structure will allow comparing the model under development with the several approaches commonly used, since the usual analytical methods do not combine all these capabilities. Thus, with this methodology research objectives **O3** and **O5** will be fulfilled.

RM4 - Evaluation of the implemented tool: In order to validate the implemented models and verify if they respond to the needs previously identified, it was necessary to compare the results obtained through them with those obtained with the approaches currently used (approximation analytical formulas, FEM simulations, and experimental measurements). Thus, the results for the self-inductance of 1- and 2-layer coils, and the mutual inductance between a 1-layer coil and a metallic target must be compared. This way, it will be possible to find out the difference in time, accuracy, versatility, and computational resources of the proposed model and the other approaches. By following this methodology it is possible to answer to the research questions **RQ2** and **RQ3** and accomplish the objectives **O4** and **O6**.

RM5 - Application of the implemented tool in an automotive APS based on eddy currents: With the advantages of the proposed approach identified and validated, a comparison can be made between the sensing element design of an APS based on eddy currents using FEM simulations (Ansys®software), experimental measurements, and the proposed analytical tool. This methodology allows to compare not just the accuracy of the inductance results obtained from the model implemented with the ones from the usual approaches, but also about the time and computational resources spent by each method to achieve the final result. It will also allow a comparison between the performance of an APS developed by the proposed analytical model with the one from a commercial APS, in order to validate the applicability of an APS based on eddy currents developed by the proposed approach. Thus,

this methodology will allow to achieve the research objective **O7** and to answer completely to **RQ4**.

1.4 Thesis contributions

Considering the state-of-the-art presented, this thesis aims to introduce some advances. The following topics describes the thesis' contributions:

- **Development of an analytical model to calculate the self and mutual inductance of planar coils with arbitrary geometry**: While the current state-of-the-art analytical models for calculating the inductance of planar coils are limited to regular geometries and a range of dimensions, the proposed model is independent of the coil geometry. This model is much more versatile, being valid for any coil geometry.
- **Integration into the analytical model the ability to calculate the influence of a conductive target on the inductance of planar coils**: The methodology commonly used to estimate the effect of a conductive target on the inductance of a planar coil requires expensive dedicated software, is very time-consuming, and requires high computational resources. With the developed model, the user can reach similar results more quickly and economically, enhancing the development of sensors based on eddy currents.
- **Ability of the proposed model work with imported geometries**: Without the need to design the planar coil and the target analytically, all geometries can be imported from the design software, making the developed model more user-friendly, easy, and quick to use.

To support the development of this thesis and to validate its scientific contribute, the following publications were done:

Journal Papers:

- A. Faria, L. Marques, C. Ferreira, F. Alves, and J. Cabral, "A Fast and Precise Tool for Multi-Layer Planar Coil Self-Inductance Calculation", Sensors, vol. 21, no. 14, p. 4864, Jul. 2021.
- A. Faria, L. Marques, L. Alves, F. Alves, and J. Cabral, "Analytical tool for optimization of position sensors based on eddy currents effect", Sensors and Actuators, A: Physical (under approval).

Conference Papers:

- A. Faria, J. Cabral, L. Marques, F. Alves, and J. Gaspar, "High precision, geometry independent analytical method for self-inductance calculation in planar coils", in Proceedings of the 2021 22nd IEEE International Conference on Industrial Technology (ICIT), Valencia, 2021.

1.5 Organisation of this thesis

This thesis is organized in five chapters, the first one is dedicated to the introduction of the problem statement, the motivation to solve it, and the several milestones defined to accomplish it.

Chapter 2 introduces the state-of-art, which is divided into two sections. The first section is dedicated to explaining the several technologies used in automotive position sensors, identifying the strengths and weaknesses of each one and their main applications. The second section is dedicated to the analytical methods that are usually used for the calculation of self and mutual inductances of planar coils, highlighting their limitations and potentialities.

With the state-of-art defined, Chapter 3 describes the implementation of the models for the calculation of the self-inductance of planar coils with one and two layers, as well as the mutual and total inductance between a planar coil and a conductive target moving over it. This chapter also has the description of the validation process of the proposed analytical model through the comparison with the results got from the correspondent FEM models and analytical approximation formulas.

Being the models implemented validated by FEM simulations pursues the experimental validation. Chapter 3 also describes all the experimental process steps, from the measurement setup to the several configurations of planar coils, the distance between coils and targets. This way, this chapter describes the experimental verification of all the variants of the analytical model implemented.

Having the analytical model implemented and validated for several coils geometries, the model is used with a use case consisting in the design of an automotive APS based on eddy currents. In order to do that, Chapter 4 describes the use case selected, detailing the requirements of the sensor, and its oscillator circuit. This chapter also explains how the model developed can be applied to the use case and accelerate its design phase without compromising the results. The results obtained are also compared with the ones got from the commonly methodology used in the development of automotive APS based on eddy currents. Thus, it is evidenced the advantages and disadvantages, with validated data, of using

the proposed analytical model in the design of automotive position sensors based on the eddy current principle.

Chapter 5 concludes this thesis, summarizing all the knowledge acquired during the various phases, investigation, implementation, and validation, and proposing future research work that can be done with the analytical model implemented.

References

[1.1] BCC Research Staff, “Sensors Markets : A Global Outlook”, BCC Research, Tech. Rep. May, 2019.

[1.2] S. Rajaram, “Sensors : Technologies and Markets to 2023”, BCC Research, Tech. Rep. July, 2018.

[1.3] S. Rajaram, “Global Markets for Automotive Sensor Technologies”, BCC Research, Tech. Rep. February, 2019.

Chapter 2

State-of-art

The main objective of this thesis is to develop an analytical model to be used during the design of eddy current based automotive position sensors. As explained in the previous chapter, the market for angular position sensors is expanding in the automotive sector, and it is in the interest of Bosch Car Multimedia Braga to invest in the development of this type of sensors. In order to understand how position sensor based on this type of technology is positioned comparatively with the offers already on the market, it is relevant to clarify and explore the main concepts related to automotive position sensors. Thereby, this chapter gives emphasis to aspects that should be taken in consideration during a sensor's analysis, selection and development. The main components of a position sensor are addressed, and a classification is made based on the physical principles, and other criteria. The several technologies that these sensors are based on and their main applications are also described. Once the potential of applications for eddy currents based sensors is perceived, it becomes relevant to analyze tools used in designing the sensing elements of a eddy current based automotive sensor. Concerning inductive sensors, there is a tendency to replace solenoids with planar coils printed on circuit boards. This transition allows for more compact, and precise solutions due to the manufacturing and assembly process. However, defining all the parameters of a planar coil in PCB to present the desired behavior can be a very challenging and time-consuming task. Currently to determine the inductances of planar coils two approaches are commonly used, one through analytical approximation formulas, valid only for some regular geometries, and the other through numerical simulations, using finite element method FEM, for coils with irregular geometry or when a more accurate result is desired. In this chapter a section is dedicated to these analytical methods, explaining several formulas that are commonly used to calculate the self and mutual inductance of single and multi-layer planar coils, highlighting their strengths and limitations.

2.1 Position Sensors

Position sensors play an important role in several applications, as they are used frequently both in mass consumption industries and automotive products. Position sensors, as the name implies, detect the position (linear or angular) of something relative to or from a fixed point. The position can be related with the distance or the angle between two points or with the distance or angle travelled or moved away from a fixed point. In the case of angular position sensors, this parameter is related with the distance travelled during a rotational movement. Thereby, an APS calculates the angular displacement of an object moving from a position to another, around an axis [2.1]–[2.4].

Within the range of APSs it can be found several modes of operation. They are classified according to:

- Physical methods used to sense the position;
- Absolute or incremental measurement;
- Reading mode;
- Assembling mode.

If a sensor is incremental, the position can just be measured through a counter increasing or decreasing. A non-volatile memory[1] to store the counter's value is used in this type of sensors, to prevent them from losing the position's information when the system is powered-off. However, the system does not register position changes when turned off. On the other hand, absolute sensors do not face these problems, since they give the real position at any time. So, for more demanding applications, choosing an absolute sensor could be the best option to take [2.4].

Other aspects that can be determinant is the reading and assembling methods. The way the sensor can be mounted and how the position's reading is done can be decisive on the sensor selection for an application. In the case of an APS, it can have a mounting design through-shaft, partial-through-shaft or end-shaft. Beyond this, measurements can be done axially, i.e. in line with the rotational axis, or radially, i.e. orthogonally to the rotational axis. Depending on the application, these design aspects could be restrictive [2.4].

Based on the way of detection, position sensors are divided into contact devices and non-contact devices. As the own name indicates, contact devices implies a physical connection to do the measurement

[1] A non-volatile memory, or non-volatile storage, is a type of computer memory that can retain information without any power supply.

(linear or angular). However, the same does not happen with non-contact sensors. In fact, by being contactless makes them more reliable, have a longer functional lifetime, provide low wear, low acoustic noise generation, and insensitivity to vibrations and contaminations [2.5][2.6]. Despite these advantages, contact-based sensors can provide simpler and lower cost solutions. This highlights that to select the best sensor it is necessary to have all the application's requirements well defined, to achieve the best relation over performance and cost [2.3].

Regarding the category of the physical principle, it is possible to have resistive, optical, magnetic and inductive position sensors [2.1], [2.7]. To better understand the differences in performance offered by each sensing method, the following subsections, from 2.1.1 until 2.1.5, describe their operation mode. These subsections also identify and relate, for each technology, its characteristics with the more suitable applications. After that, a dedicated subsection clarifies the main aspects to consider during a sensor's specification. As the focus of the investigation is on automotive angular position sensors, within each physical category, the sensor examples described are focused on angular measurement.

2.1.1 Resistive Sensors

Potentiometers are the most commonly used resistive position sensors. They are simple devices that translate movement into a change in the resistance value. They have been used as position measurement for more than a century, being originally developed for military applications. They were mainly used in radios and televisions as adjustment knobs [2.2]. A potentiometer has three terminals (Figure 2.1), and it can operate in two modes, as a voltage divider or a rheostat. For the potentiometer to operate like a voltage divider it is necessary to use all the terminals.

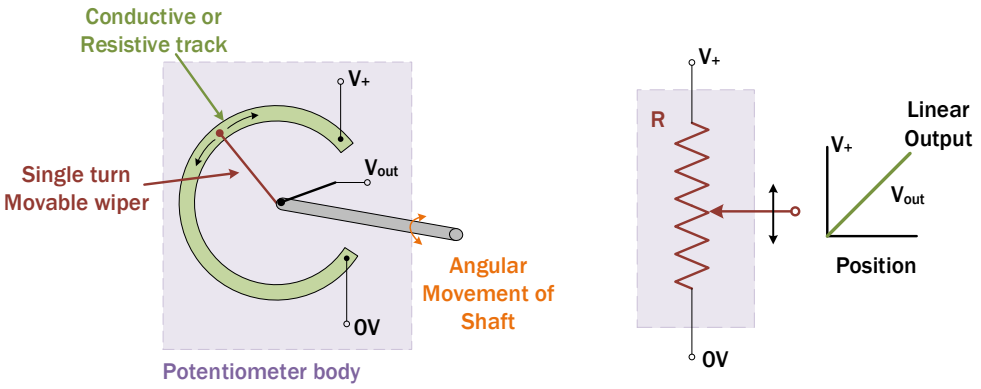

Figure 2.1: Potentiometer Model [2.2].

Potentiometers work well, over long periods, in a lot of applications. In the past they have been applied in many areas of engineering, as in multi-fan hovering systems [2.8], medical instruments [2.9], motor control [2.10], etc. What makes them very desirable is the fact that they are [2.11][2.3][2.12]: low cost, low tech, easy to use, simple operation, simple application theory, robust Electromagnetic Interference (EMI) susceptibility; compact; lightweight; linear; and can me made accurate.

In fact, for the majority of the potentiometer designs, the key parameter is their linearity [2.13]. However, as these sensors have moving parts with physical contact, they are susceptible to wear, vibrations and foreign particles (as dust or sand). They have also low accuracy, low repeatability, limited frequency response and shorter sensing angle. Beyond this, the main disadvantage that potentiometers have is the limitation that its physical size has in the range of the wiper's movement, and hence in the output signal obtained. Despite all these disadvantages, potentiometers continue to be used in some applications related to safety in industries like aerospace and medical. They usually classify these sensors as "simple devices", not having so many restrictive criteria as the electronic ones. This situation makes some potentiometers replacements being unreliable [2.12]. Due to the market's tendency to replace the potentiometers, the potentiometer's industry has, in the past few years, invested in improving the characteristics of its sensors. Making them more reliable, accurate and even more cost-effective [2.11].

2.1.2 Capacitive Sensors

A capacitor is an electrical component that stores electrical charge. Typically, it is composed by two conductive plates with an insulator between them. The quantity of stored charge is dependent of the plates' size, its percentage of overlap, the distance between them and the insulator's permeability. This way, a capacitive sensor can be seen as a non-contact device that measures the plate separation. Usually, it uses metal plates and the insulated between them is air. It can be noted that this kind of devices uses the electrical conductance to measure position. They are mainly used in linear displacement measurements, from a few millimeters to nanometers. And, due to this, they are used in high accurate and high frequency response applications, such as in disk drives. However, capacitive sensors can also be used for rotary position sensing. For doing that, a series of plates are cut or etched along the measurement axis. This way, the sensor has one of the plates that moves across the plates attached to the sensing axis, as outlined in Figure 2.2 [2.3]. Thereby, the variation of the capacitance along the axis indicates the relative position of the two parts, being the distance (d) of the sensor plates from the target plates the only ones responsible for changes in the capacitance, since the dielectric, the plates' size and area will remain constant[2.1], [2.3].

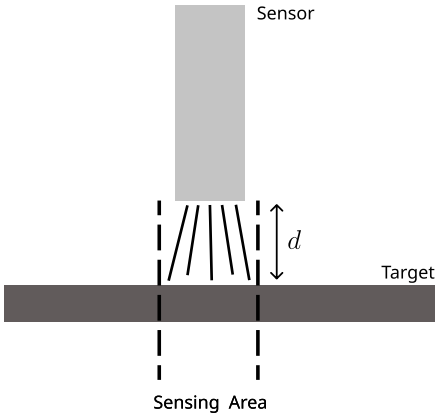

Figure 2.2: Schematic of the behaviour of a capacitive sensor [2.3].

Although it is possible to apply this capacitive sensors in angular position measurements, the necessary configuration (multiple sensors) causes some concerns. In order to not compromise the position measurement, the excitation voltage of all the sensors used must be synchronized. If there is no synchronization, the sensors will interfere with each other and the readings will be compromised. Another issue about these sensors is the fact that they are not able to work under dry or wet environments and in conditions where the distance between the sensor and the target is large [2.3].

2.1.3 Optical Sensors

After the potentiometric sensors, optical sensors are the most popular for measuring position and displacement. What makes them desirable for many applications is that they are simple, insensitive to stray magnetic field interference, and can operate over relatively long distances [2.1]. Several solutions of these type of sensors are available, however they usually are composed by a light source, a photo-detector and optical components (mirrors, lenses, etc.).

Optical encoders are one of the common approaches to this type of sensor, and usually follow two sensing principles. One of them is based on received light from a light source (LED or infra-red). This light passes through the rotating encoded disk that contains the required code patterns, and the light that comes out is sensed by a photo-detector. Another method is by sending the light to a reflective band placed on the encoder's axis. In this approach the light reflection is sensed [2.12], [2.14].

Encoders can be divided in two types: incremental encoders and absolute position encoders [2.1]. Incremental encoders, also denominated as relative encoders, can be composed of one or two position sensors. Figure 2.3 [2.2] shows a simple example of an optical incremental encoder where it is possible

to identify two position sensors, that in this case are photo-detectors, the pattern on the disk, and the two outputs. By counting the pulses from the output square wave, the angular position of the rotating shaft can be obtained. As the outputs from the optical position sensors are displaced by 90° out of phase, through the outputs sequence, it is possible to determine the rotation's direction [2.2].

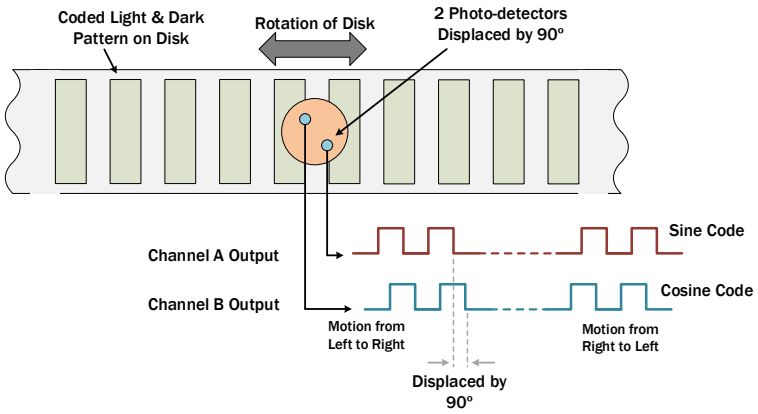

Figure 2.3: Schematic of an optical incremental encoder [2.2].

In turn, the absolute position encoders are more complex than the incremental ones. They provide a distinct output code for each position of the rotating track, being able through it to know the position and direction of the movement. Their coded target is composed by several independent tracks, having each one its own position sensor to read. The measurement of the rotary movement is given by the combination of all the readings performed by each track's sensor. Figure 2.4 [2.2] shows the output of the position sensors of an optical absolute position encoder with a 4-bit binary coded disk. It is possible to see that the combination of the four photo-detectors provide an unique combination for each angle position.

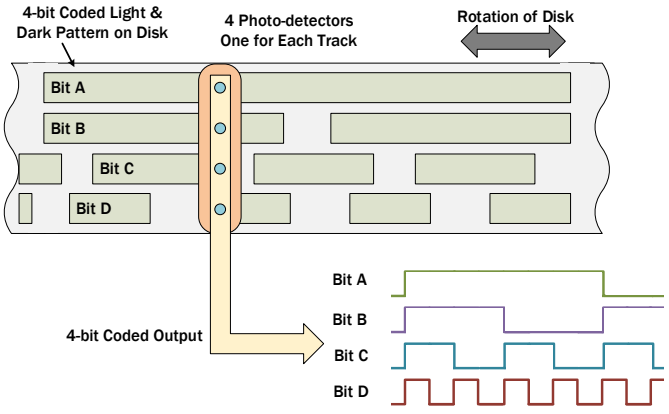

Figure 2.4: 4-bit binary coded disk of an optical absolute position encoder [2.2].

Comparing the incremental encoder's type with the absolute one, although it is simpler, in angular position applications incremental encoders need an external counter to compute the absolute angle of the shaft

after a rotation. Another issue that is important to consider is the fact that as this type of encoders count pulses, if it misses a pulse, due to dirty or vibrations, or if the power fails, the output of it will be compromised. This situation can be sorted out by using absolute position encoders. Due to its non-volatile memory, they are able to retain the current position of the encoder, even when the power is turned off. However, a transversal disadvantage of encoders is that to achieve higher resolution is necessary to increase its size since to have more resolution it is necessary to increase the number of tracks on the sensing pattern. Another disadvantage associated to optical encoders is the high assembly accuracy that is required [2.2], [2.12], [2.14].

2.1.4 Magnetic Sensors

Magnetic position sensors belong to the category of non-contact devices. Because of that, they are very robust, offering several advantages such as low sensitivity to vibrations and foreign particles, as low wear. These characteristics make them being very attractive to a lot of applications.

The angular position measurements can be achieved by sensing the variation of the magnetic fields. These variations can be due to the magnetic fields' strength, direction or just its presence. It is relevant to highlight that this is valid for all sources of magnetic fields, from permanent magnets, and those induced by electric currents, to Earth, etc. There are several sensing principles that can be applied to perform the sensing. The most common are Hall-effect sensor, Anisotropic Magnetoresistive sensor (AMR), Giant Magnetoresistive sensor (GMR), and Tunneling Magnetoresistive sensor (TMR). In order to understand the weakness and strengths, and the adequate working conditions of each one of the techniques, the current subsection will be dedicated to them. Nonetheless, the Table 2.1, can give a quick overview of the main differences between the technical performances of the technologies [2.15].

Table 2.1: Comparison of magnetic sensing technology parameters [2.15].

Technology	Hall Effect	AMR	GMR	TMR
Power Consumption (mA)	$5 \sim 20$	$1 \sim 10$	$1 \sim 10$	$0.001 \sim 0.01$
Die Size (mm^2)	1×1	1×1	1×2	0.5×0.5
Field Sensitivity (mV/V/Oe)	~ 0.05	~ 1	~ 3	~ 100
Dynamic Range (Oe)	~ 10000	~ 10	~ 100	~ 1000
Resolution ($nT/Hz^{1/2}$)	> 100	$0.1 \sim 10$	$1 \sim 10$	$0.1 \sim 10$
Temperature Performance (^oC)	< 150	< 150	< 150	< 200

Despite the various approaches that can be used to perform an angular measurement through a magnetic

sensor, usually, they can be summarized in a magnet changing its position in relation to a magnetic detector. This way, the magnet relative displacement varies proportionally with the magnetic fields' changes.

The robustness of the magnetic sensors and their immunity to foreign particles, allow them to overcome some disadvantages of the optical sensors. However, due to magnetic hysteresis, they are uncommon in applications that require highly accurate measurements. They are not adequate also for harsh impact applications, due to magnets brittleness. Another limitation of this technique is the interference that external magnetic fields can produce on the sensor's readings [2.15].

Hall-Effect

When a metal plate is carrying a constant current, and an orthogonal magnetic field is applied to it, a voltage appears over the plate. This phenomenon is named by Hall-effect and is represented in Figure 2.5 [2.16]. As the voltage intensity changes proportionally to the strength of the applied magnetic field, this effect can be used, for example, to measure the angular position of a rotor, which has attached a rotating magnet. It is relevant to note that, the density of the flux lines that intersect the plate decreases with the increase of the distance between the magnetic source and the plate. Due to this, it can be understood why there is a mounting distance limitation between the Hall-effect sensor and the magnetic source [2.4].

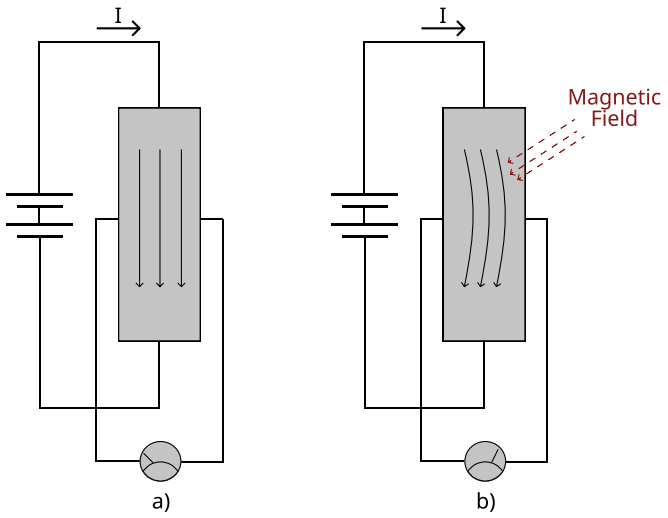

Figure 2.5: [Hall effect in a conductive plate. (a) No magnetic field is applied, so there is no voltage across the plate. (b) A magnetic field is applied, and a voltage is detected over the plate [2.16].

Furthermore, foreign magnetic fields, temperature variations, and magnetically permeable materials nearby can interfere in the Hall-effect sensor's output. These limitations oblige to know and control well the environmental conditions of these sensors, such as Electromagnetic Compatibility (EMC) and mechanical

tolerances [2.14]. The main advantage of Hall sensors is their simplicity, what makes them very cheap, small and compatible for a lot of applications that do not require highly accurate measurements [2.17]. They also provide a constant behaviour over time and a good performance in the presence of moisture, dust, and vibrations [2.3], [2.4].

Magnetoresistive effect

Magnetoresistive sensors are similar to the Hall sensors since both detect the strength of the field that crosses them. However, the magnetoresistive ones can also detect the field direction. Despite this, the effect that occurs in each of these types of sensors is entirely different. The magnetoresistive effect occurs in ferromagnetic materials whose resistance changes with the variation of the magnetic field applied. This way, the variation of the resistance indicates the angular displacement between the magnetoresistive element and the lines of the magnetic field sensed. As can be seen in Figure 2.6 [2.6], within the range of magnetoresistance sensors, three different approaches stand out: AMR, GMR, and TMR [2.6].

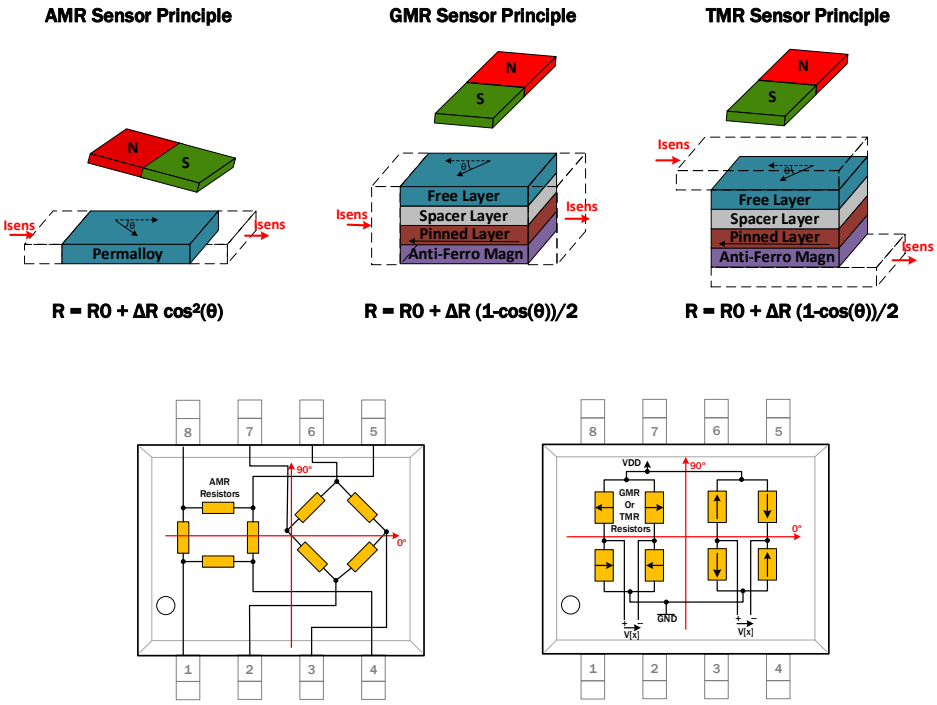

Figure 2.6: Sensors principle of the various MR technologies [2.6].

AMR sensors usually integrate one or two Wheatstone bridges[2]. Each one has four resistive films connected in diamond shape, as detailed in [2.17]. When no magnetic field is applied, in ideal conditions, the bridge is balanced and the side contacts are at the same voltage, so $\Delta V = 0$ V. In the presence of

[2]Wheatstone bridge is an electrical circuit usually used to measure unknown resistance values

a magnetic field, a change in the film's resistance occurs and a differential voltage is produced between the side contacts, $V \neq 0$ V. This voltage is dependent of the angle, that is the angle between the element current flow, and element magnetization [2.17][2.18].

The AMR sensors integrating one Wheatstone bridge have the capacity to measure the magnitude of the magnetic field, while the ones that incorporates two bridges can also detect the direction of the magnetic field. Compared to Hall sensors, AMR sensors can provide higher sensitivity and resolution with lower field strength [2.15][2.17]. However, the angular measurement range of an AMR sensor is only 180^o, which could be a limitation for some applications [2.19][2.6]. To increase this range to 360^o two sensors are required.

Although AMR and GMR sensors are both magnetoresistance sensors, their principle of operation is very distinct. A GMR sensor with a current in plane configuration is composed, at least, by one non-magnetic conductive layer placed between two magnetic layers, as is visible in Figure 2.7 [2.20]. When no external magnetic field is applied, the magnetization of the magnetic layers is inverse. It is relevant to note that in magnetic materials the conductive electrons have spin characteristics. This way, they can be spin up or spin down, according to the direction of the material's magnetization. So, as shown in Figure 2.7 [2.20], the electrons have a short free path movement, moving only between their layer and the non-magnetic one. The length of electrons' path is shorter the thinner the layers are. This effect happens because electrons have more difficulty to travel without hitting the layer's boundary. Hereupon, it is perceptible why the GMR's resistance becomes higher with thinner layers, more boundary collisions translate into longer travel times for electrons to flow through the layers [2.20].

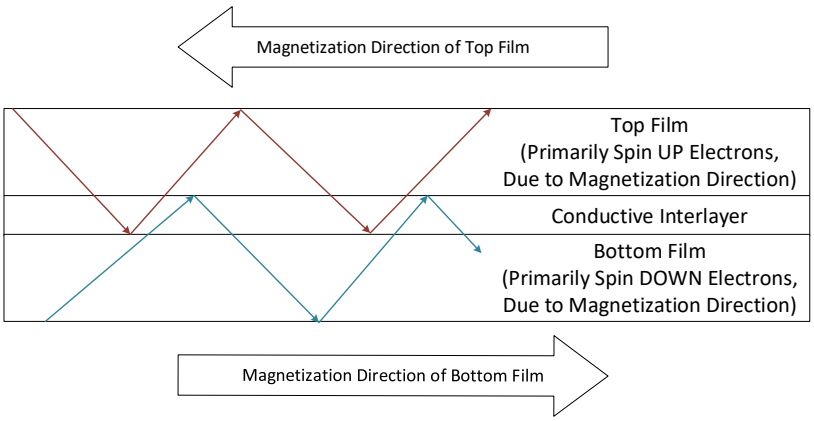

Figure 2.7: Electrons path in a GMR sensor without an external magnetic field [2.20].

Nevertheless, when a magnetic field of sufficient magnitude crosses a GMR sensor, it breaks the coupling of the magnetizations between the magnetic layers. Herewith, the electrons can travel through the two

layers, having now all the same spin value, as is represented in Figure 2.8 [2.20]. With this, there is an increase of the traveling area, the free path length of the electrons, and consequently a decrease of the GMR's electrical resistance [2.20].

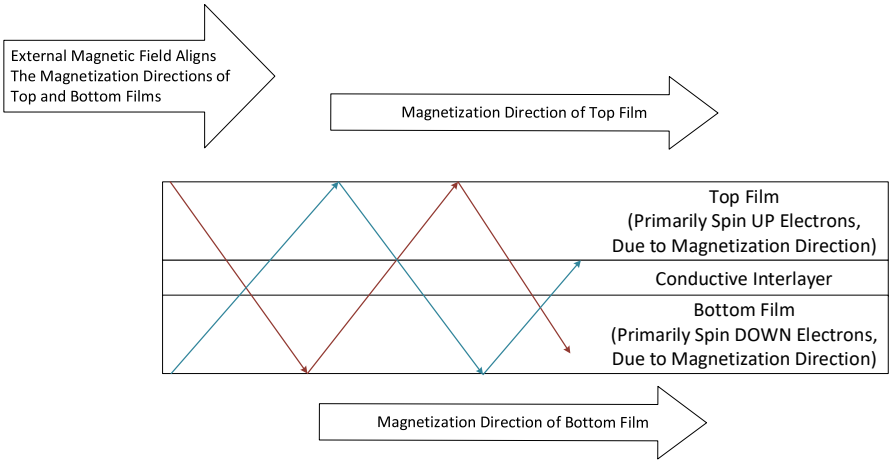

Figure 2.8: Electrons path in a GMR sensor with an external magnetic field [2.20].

The GMR's configuration described before is just one of the possible configurations. Actually, in Figure 2.6 [2.6] is visible another GMR configuration. The operating principle continues to be based on the difference between the magnetizations' directions of adjacent layers. However, instead of a ferromagnetic coupling between the layers, it has one of the magnetic layers with its magnetization direction fixed, also called as pinned layer. To fix the magnetization direction, an anti-ferromagnetic field layer can be added next to the pinned layer. Figure 2.6 [2.6] shows a different placement for this fourth layer in the GMRs structure. In [2.18] another placement of this layer is presented, explained in detail what happens in each layer when a GMR sensor is and is not crossed by an external magnetic field.

Comparing GMR with AMR sensor, they can offer higher sensitivity, lower size, but not better resolution [2.21]. Despite both technologies use two full bridges, as visible in Figure 2.6 [2.6], the GMR has the advantage of having an angular measurement range of 360^{o}, that is the double of the provided by AMR sensors [2.6]. However, the rotation angle is determined, in both sensors, through the arctangent function, where the sine wave and the cosine wave come from the two bridges [2.19].

TMR is also based on a quantum phenomenon such as GMR. TMR uses one Magnetic Tunneling Junction (MTJ) in its configuration. What distinguishes the TMR from the last GMR's configuration analysed is the property of the layer between the free and the pinned layers. In GMR this layer is a conductor, whereas in TMR it is an insulator. With this, TMR sensors can provide a higher change in resistivity, since this layer offers a much higher resistance to the current flow, thus acting as a barrier. Despite TMR and GMR

sensors having a similar operating mode, the TMR one through the tunnelling effect can produce a larger signal amplitude with higher sensitivity and lower noise [2.18]. However, for detecting low signals, AMR might be the better option, since its noise is lower than the one from TMR. Besides these advantages, as TMR sensors have more layers than the others MR sensors they are more expensive [2.21].

In all of magnetoresistive approaches, their resistance is dependent on the angle between the free layer and the magnetic field of reference. The free layer follows the variation of the external magnetic field, represented by a magnet in Figure 2.6 [2.6]. This way, if the magnet rotates, the angle between the free layer and the reference will follow this movement, the resistance changes, and the output's sensor gives the rotation angle [2.6]. To obtain the corresponding voltages signals, Wheatstone bridges are used (Figure 2.6 [2.6]), having the AMR an angular measurement of 180^o, and GMR and TMR of 360^o. Due to the physical characteristics of MR sensors, they are not appropriate for working in environments susceptible to harsh shock or vibrations, and temperature oscillations [2.14].

2.1.5 Inductive Sensors

Generally, inductive angular position sensors are based in an electrical induction principle, discovered by Michael Faraday. Figure 2.9 [2.22] illustrates an example of this principle. This way, when an alternating current is applied to the Tx Coil (transmit coil), a current is induced in the Rx Coil (receive coil). The voltage signal at the receive coil terminals is dependent on the areas, geometry and distance between the two coils, being proportional to them. However, these are not the only parameters that can change the operating mode of the coils. Temperature, as seen previously, is one of these parameters. Nevertheless, with a differential approach, it is possible to minimize external effects and even tolerances and other manufacturing defects [2.22], [2.23].

Inductive sensors are also non-contact devices, and due to their characteristics, they can be applied, as the magnetic sensors, in harsh working conditions. Environments with dust, water, shocks, vibrations or harsh electromagnetic fields (by using the differential approach) will not be an issue [2.24]–[2.26].

Despite their robustness and reliability, this type of sensors have not been used so often due to their weight and dimensions of their traditional approaches. Since this type of approach is based on a series of wound conductors or spools, for the sensor to achieve strong electrical signals and good angular position accuracy, a high precision winding process is required. This way, in addition to the problems of large dimensions and weight, there is also an increase in costs. To overcome these disadvantages associated with wire wound spools, other approaches based on the same physical concept have been developed.

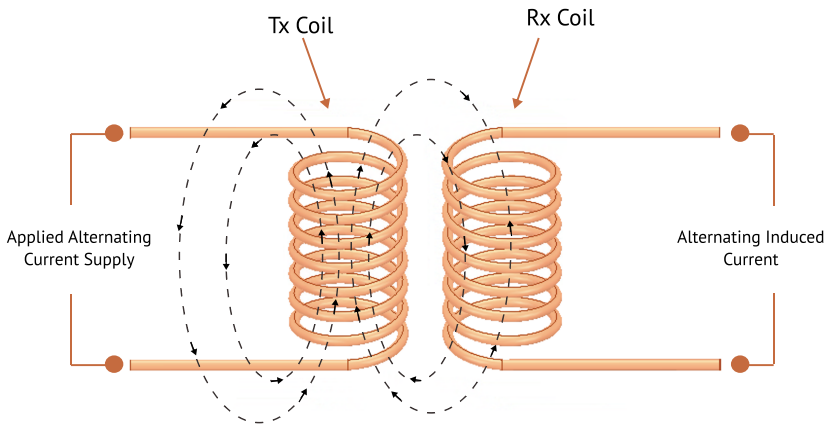

Figure 2.9: Faraday's Induction Law [2.22].

Example of this is the use of coils printed in Printed Circuit Boards (PCB). These planar coils, in addition to overcoming the problems related to the size, weight, and cost, and to maintaining the stability and robustness, can also provide a better measuring performance and a higher geometry's flexibility [2.22], [2.26], [2.27].

Inductive sensors use the self-inductance of a coil or the mutual inductance between several coils to obtain the measurement angle/distance. In this way, they can be configured in different shapes and formats. It is possible to have inductive sensors based on the coil coupling effect, the eddy current effect or even a combination of both. It is even possible to find inductive devices that combine these technologies with magnetic sensors, such as AMR and hall effect sensors [2.25], [2.26], [2.28].

Coil Coupling Effect

Inductive sensors based on coil coupling effect perform their measurements through the variations on the mutual inductance between the coils. Inside this range, it is possible to identify several devices such as resolvers, synchros, Variable Reluctance (VR) resolvers, and Rotary Variable Differential Transformer (RVDT).

Conventional resolvers can be seen as a differential transformer or a small electric motor with one primary/rotor winding and two secondary/stator windings. Its operation mode follows the inductive principle explained before, by applying an excitation signal[3] to the rotor winding, an inducted signal will appear in the stator windings. This way, the angular measurement is based on the position relation between the

[3]The excitation signal corresponds to an AC reference signal.

rotor winding, which has coupled the rotating shaft whose position wants to be measured, and the stator windings (stationary elements).

On the other hand, in VR resolvers both primary and secondaries windings are placed in the stator. The main advantage of VR resolver over the conventional resolvers is the simplicity of the geometry. This way, they are a more competitive approach in the field of angular measurements than the conventional resolvers, since they can offer lower size, mass, and higher reliability [2.29][2.30]. J. Oshino and I. Sasada proposed in [2.31] a new type of resolver, replacing the wound wire coils by printed coils in PCB.

Synchros are other devices that belong to the family of resolvers. Although they follow the same working principle of conventional resolvers, instead of having two stator windings, synchros use three stator windings electrically Y-connected, as can be seen in Figure 2.10 [2.32]. In order to increase their competitiveness and performance, new approaches are being developed. Example of that is the sensor presented in [2.33]. This new approach is like a combination between the VR resolvers and the synchros.

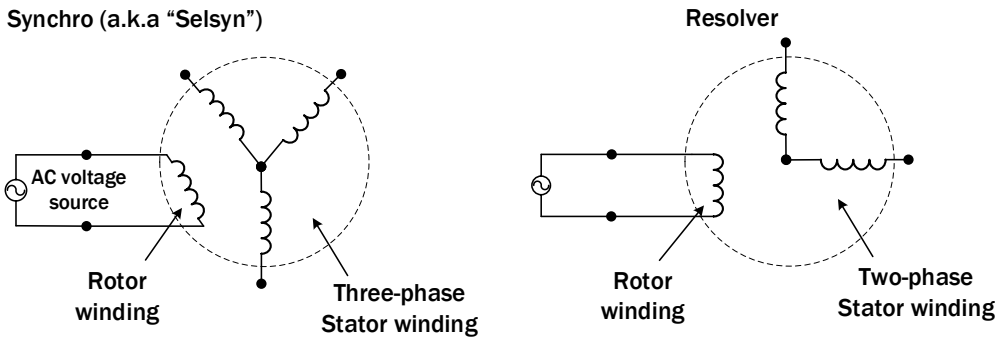

Figure 2.10: Synchro and classical resolver layouts [2.32].

In a general way, despite encoders having better accuracy than resolvers/synchros, they are more complex, larger in size and expensive. So, for applications that do not require so higher precision control, resolvers/synchros end up being preferable due to their advantage in relation to the size, costs and working conditions, which usually are critical parameters in many applications [2.33][2.34]. Nevertheless, the company Celera Motion has a sensor called Incoder that they claim to be a good option to replace synchros. It uses the same induction principle, maintaining a similar reliability, and capability of operating in harsh environments, and in addiction the main components are printed on circuit boards, offering this way a solution smaller, lighter and less costly [2.35].

RVDT sensors are composed by a primary winding, two secondary windings, and a rotating magnetic core, as represented in Figure 2.11 [2.36]. An excitation signal is applied to the primary winding, and a

magnetic field is generated, which in turn induces a current in the secondary windings. The measurement of the angular movement of the rotating core is based on the changing of the mutual inductance between the primary and the secondary coils [2.37]. According to [2.38], since the 1990s printed coils in PCB have been integrated in RVDT, decreasing its weight and size significantly.

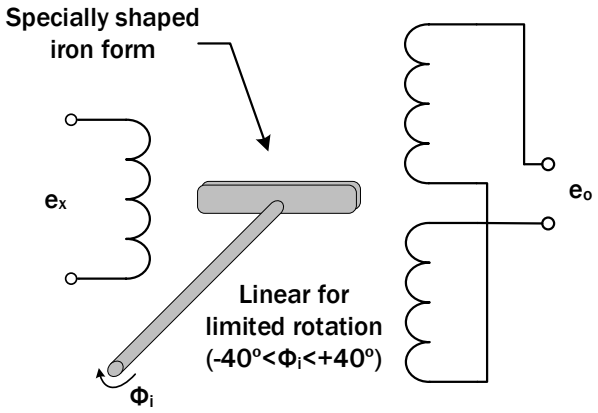

Figure 2.11: RVDT schematic [2.36].

Due to its configurations, RVDT sensors are widely applied in industrial applications that require high resolution, linearity, and reliability, as well as fastness. RVDT presents advantages compared with Hall sensors, since they can offer a better angular accuracy, and with absolute grating encoders because they can be less expensive and easier to use [2.39] [2.37].

Eddy-current Effect

An angular position sensor based on the eddy-current technology, also known as Foucault's current, uses the variation of the electromagnetic field to sense the angle of rotation. This type of sensor consists of a sensing coil, that is powered with an alternating current, which creates an alternating magnetic field. When this field is intercepted by a conductive plate, closed loops of currents, perpendicular to the magnetic field, are induced in the target material, being these called eddy currents. These currents, in turn, generate their own magnetic field, which is opposite to the original field generated by the sensing coil [2.40]–[2.43]. Figure 2.12 represents at red the induced eddy currents, at black the magnetic field generated by the coil and at green the magnetic field generated by the induced currents. These induced currents have the particularity of being concentrated near the surface adjacent to the coil, decreasing exponentially its density with the the increase of the penetration into the target, known as the skin depth effect [2.7].

Thereby, the magnetic field generated by the eddy currents decreases the original magnetic field generated by the coil, changing this way the coil's impedance. This impedance variation depends on the target

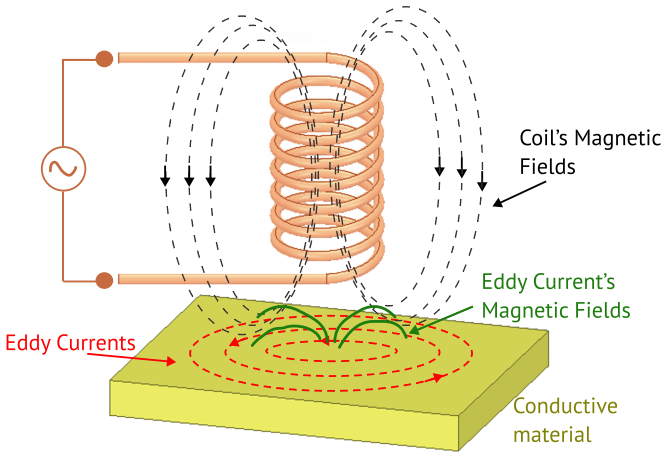

Figure 2.12: Eddy current phenomenon [2.7].

material, the distance and overlapping area of the target in relation to the coil since eddy currents tend to propagate parallel only in the area of the magnetic field of the coil. In order to make the systems more competitive, the wound coils are being replaced by planar coils, printed in circuit boards. This allows more compact, accurate, and precise solutions, owing to the fabrication and assembly process [2.26], [2.35], [2.43]–[2.46].

In the area of angular measurements there are only a few sensors ([2.47]–[2.51]) and studies ([2.24], [2.27]) based on this type of technology. It is more predominant in proximity ([2.36], [2.40]) and linear measurements ([2.25], [2.52]–[2.56]), and in detection of material's defects ([2.57]–[2.60]). However, angular sensors based on this technology are considered a potential approach because of their capability of working under hard conditions, as oil and dust, and because of their reliability, and resolution [2.26].

In the literature it is possible to find several eddy current angular position sensors with different structures. The common methodology consists of one or more excitation coils, one or more sensing coils and one or more conductive targets. Amongst the approaches found, there are some where the sensors have a geometry similar to encoders, as the one presented in [2.24], [2.61], where the code disk is composed by several copper targets printed on a PCB, corresponding these to the grating structures (Figure 2.13A). However, this approach has the same disadvantage as the aforementioned encoders, since, in order to have higher resolutions they end up achieving large dimensions. There are also some approaches that use, for example, an excitation coil, two sensing coils and a 3/4 circular electrically conductive target, as presented in [2.27] (Figure 2.13B), and others with two excitation coils and one sensing coil, where their geometries and the electrically conductive target are adapted to some measurement ranges [2.50]. Another possible methodology for an eddy current sensor is presented in [2.53], where instead of a

electrically conductive target it is used a ferrite target (Figure 2.13C).

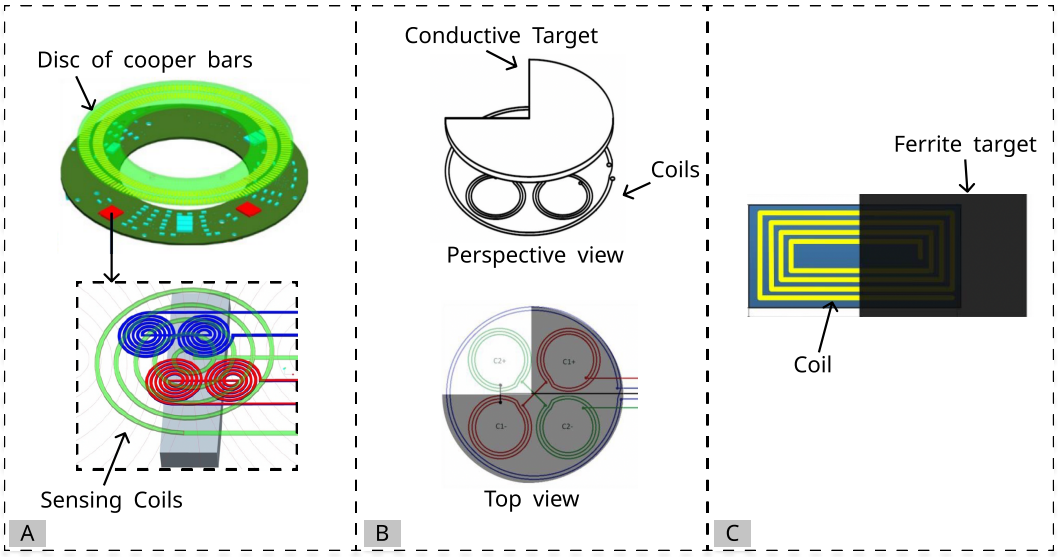

Figure 2.13: Eddy current sensors: A - Planar coil based absolute magnetic rotary sensor [2.24] || B - Low cost planar coil-based eddy current sensor [2.27]. || C - Inductive displacement sensor with a ferrite target [2.53].

According to [2.28], the use of excitation and sensing coils is a methodology that makes the solution more precise. However, in [2.62] is presented an eddy current angular sensor that does not follows the methodology commonly used. This proposal use four identical flexible coils, fabricated on four different flexible PCBs, energized individually. They are surrounding a rotary conductive cylindrical hollow shaft with a semicircular groove, which is responsible for the variation of the magnetic field generated by the eddy currents. This way, it changes the value of the inductance of the coils in function of the angle of rotation. The performance of this thesis' proposal is compared to the one from sensors based on different technologies and approaches, inclusive with the sensor presented in [2.63], that follows the common methodology (four excitation coils and one sensing coil). Despite [2.62] not using the methodology that is known as the one that offers more precise solutions, it is shown that their proposal, when compared with [2.63], it offers a better resolution.

In short, it can be concluded that, for this type of sensor, the geometry, organization, and relationship between its components, coil(s) and target(s), is very dependent on its application and crucial on its resolution. Another factor that also increases the variety of possible architectures is the fact that both coil(s) and target(s) can be printed on rigid or flexible PCBs. Taking into account the precision of the manufacture process of a PCB, the geometric versatility that each of the components can acquire, and the reduction in

costs of both components and in the manufacturing and assembly processes, it is perceptible the potentiality that angular position sensors based on eddy current have for competitive industries where cost and performance are an issue. Furthermore, these sensors can be a good option to replace magnetic angular position sensors, such as those based on the Hall-effect or on magnetoresistive materials (AMR,GMR, and TMR), since, in general way, their resolution is within the same order of magnitude , and because it is no longer necessary to use magnets and materials with specific properties such as magnetoresistance. Considering the cost associated with these materials and magnets, the replacement of magnetic sensors by inductive ones based on eddy currents results in a reduction in the cost of the product.

Conclusions

With regard to the various technologies used in commercial angular position sensors, it can be concluded that for applications where the sensor's durability is a requirement, non-contact measurement sensors are preferable, so that there is no associated physical wear. In order to select the most suitable technology for a given application, it is necessary to take into account factors, such as size and weight, resolution, range of measurement, power consumption, costs, ability to work in hostile environments, and immunity to external magnetic fields. For applications where it is needed very accurate measurements, as in some industrial manufacturing robots, and costs and size is not an issue, resolvers and optical encoders are the most adequate sensors. However, for applications where it is required lower weight, size and costs, and it is not a demand to have a good accuracy, a resistive potentiometer or a hall sensor can be a good option. Although, if the application also has a high resolution as a requirement, the most promising sensors become the inductive based on eddy currents and the magnetic encoders. For situations that require higher robustness and not so much accuracy to need an encoder, an resolver/synchro or an RVDT can be a good solution. The Table 2.2 resumes the relation between the several non-contact APS technologies described previously and some funcional parameters. This table does not include the potentiometers and the mechanical encoders for them being a contact sensor, and the capacitors because their ranger of measurement (from several millimeters to nano-millimeters) is much lower than the one from the other sensors in comparison.

Considering the requirements of automotive position sensors and the analysis presented above, it is clear that eddy current technology has potential in this market area. Since the area of position sensors with planar coils based on eddy currents is expanding, the relevance of this thesis can be proven. As seen earlier, for inductive sensor applications where the cost and size of the sensors are a critical issue, solenoids are being replaced by planar coils printed on circuit boards. However, the design process for this type of coil

Table 2.2: Comparison between several angular sensor technologies

Parameters	Optical Encoder	Magnetic Encoder	Hall-effect Sensor	AMR/GMR /TMR Sensor	Resolver/ Synchro	RVDT	Eddy Current Sensor
Size and Weight	High	High	Low	Low	Medium High	Medium High	Low
Accuracy	Very High	High	Medium	Medium	Medium High	Medium High	High
Cost	Very High	High	Medium	Medium	Medium High	Medium High	Low
Power	Medium	Medium	Low	Low	High	High	Low
Work harsh conditions	No	Without Impacts	Without Impacts	Without Impacts	Yes	Yes	Yes

can be very challenging and time-consuming. Currently, to design this type of coils, two approaches are commonly used, analytical approximation formulas (for some regular geometries), and numerical simulations, using the finite element method (for coils with irregular geometry or when a more accurate result is desired). The following subsection is devoted to explaining the various analytical formulas commonly used to calculate the self and mutual inductance of single- and multi-layer planar coils. With this analysis, strengths and limitations are identified, making it clear what needs to be improved. This information will be useful for the tool under proposal in this thesis.

2.2 Inductance of Planar Coil

Since the main objective of this thesis is to develop an analytical model for the calculation of inductances of planar coils printed on PCB, it is necessary to analyze the tools that are commonly used for this purpose. Thus, this section is dedicated to the most used planar coil inductance calculation methods in the literature. The inductance of planar coils depends on the dimensions of the planar coil and its settings such as width size, space between turns, number of turns, and geometry. As such, it is noticeable that matching all these parameters with the coil application requirements is a very challenging and time-consuming process. Thus, to optimize this design process, a study was carried out to understand what is being used, its limitations, how the complexity of the process is an issue, and how it can be improved.

The planar coil's design process can be done analytically or through a finite-element model. Through a three-dimensional (3D) finite-element model, it is possible to compute a very accurate solution by resolving Maxwell's equations. Although FEM simulation is the most accurate methodology, it requires expensive simulation programs, such as Ansys®software, high computational resources, and the FEM model development itself is a meticulous and challenging process. It also has the disadvantage that the simulation of

the model can take from minutes to several hours or days, depending on the complexity of the model, the desired precision, and the number of cases and variables in simulation. Due to these aspects, this method may become more appropriate for design validation than for its development [2.64], [2.65]. Which concerns to the formulas used by the numerical simulators, in [2.66] and in the Ansys®documentation, it is explained how Ansys®software calculates the inductance of the coils. The program uses the relation between the energy stored (W) in the coil by an applied current (I) to determinate its inductance (L), as given by equation 2.1.

$$L = \frac{2W}{|\ I\ |^2} \tag{2.1}$$

Thus, a methodology based on approximation formulas is ideal to overcome part of the disadvantages of FEM simulations, since it is no longer required to use high computational resources and dedicated software tools, and is much faster when compared to a full FEM simulation. However, the simplicity associated to it can bring some limitations regarding the coil geometries, and the precision of the results. Based on the literature [2.44], [2.65]–[2.76], there are several approximation formulas for calculating the inductance of planar coils, some are application specific [2.76]–[2.79], or are only valid for one type of geometry [2.44], [2.73], [2.74], [2.80], and some remain valid for several regular geometries [2.44], [2.65], [2.73], [2.81]. In this way, this section is divided into two sub-sections, the first dedicated to the analytical calculation of the self-inductance of single-layer flat coils and the second to the analytical calculation of the inductance of multilayer coils. Each part presents the methods and formulas commonly used to calculate the respective inductances, their advantages and disadvantages. In the end, the strengths and weaknesses of each method are highlighted, summarizing the characteristics that an inductance calculation method for planar coils must match to ensure the best relationship between time, versatility and accuracy.

2.2.1 Inductance of a Single-layer Planar Coil

The areas of application for planar coils on Printed Circuit Boards (PCB) have increased over time [2.44]. When compared with solenoids, they offer more design flexibility, high repeatability, and easy integration. This way, they reduce not just the costs of production, integration, and assembly, but also the weight and size of the solution [2.35], [2.45], [2.46]. Other advantages are the fact that they have good thermal performance, robustness, resistance to disturbances, longevity and can be printed on stretchable materials [2.46], [2.64], [2.70]. These properties make planar coils very desirable for competitive industries, such as automotive, health care, robotics, or consumer electronics [2.82], [2.83]. Because of all of this, their use is increasing, as well as the demand for coil design software.

In planar coils, as they are concentric, the core area is not the same for each turn. In other words, for a given outer-diameter, the greater the number of turns of the coil, the smaller the internal diameter. Thus to calculate the inductance it is necessary to have into consideration the self-inductance of the conductor, the mutual inductance between each current-turn, and the environment around the coil. Due to this, several models and methods estimate the inductance of planar inductors through some approximations. They usually are based on curve fitting techniques, numerical approaches, e.g. finite element method (FEM), or empirical formulas, having always an error and restrictions associated with it [2.44], [2.66]–[2.73], [2.75], [2.84]–[2.86]. The Greenhouse method, also known as the Expanded Grover method, is identified ([2.70], [2.75], [2.76], [2.78], [2.87]) as the one that offers the most accurate solution. However, it is not the most used due to its complexity of implementing from scratch each time it is wanted to determine the inductance of a coil. This method considers that the inductance of a planar coil is the result of the sum of all straight conductor's self-inductance, L_0, plus the mutual inductance between each segment pairs. The mutual inductance value depends on the angle between the two segments, the space between them, their length, and on the direction of the current on the wires. Since the planar coils are concentric, it is visible in Figure 2.14 that the direction of current is not the same in all the traces. Thus, the resulting inductance, L_T, can be obtained through:

$$L_T = L_0 + M_T \tag{2.2}$$

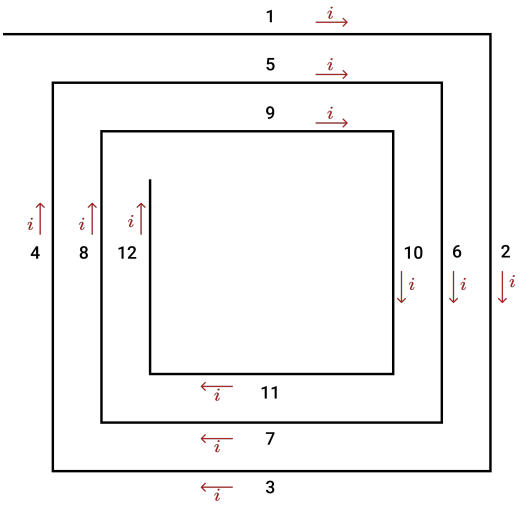

Figure 2.14: Square planar coil with three turns.

Taking the example of a square planar coil with three turns, as shown in Figure 2.14, the total self-inductance, L_0, of all the segments is equal to:

$$\begin{aligned} L_0 = L_{self1} + L_{self2} + L_{self3} + L_{self4} + L_{self5} \\ + L_{self6} + L_{self7} + L_{self8} + L_{self9} + L_{self10} + L_{self11} + L_{self12} \end{aligned} \tag{2.3}$$

The self-inductance of each straight conductor, with a rectangular cross-section of w and t dimensions, can be calculated using:

$$L_{self} = 0.002l(\ln(\frac{2l}{w+t}) + 0.50049 + \frac{w+t}{3l}) \tag{2.4}$$

where l (cm) is the conductor length; w (cm) corresponds to the wire width; and t (cm) to its thickness.

The mutual inductance between the segments 1 and 5 has two components, one caused by the current flowing in segment 1, $M_{1,5}$, and another by current flowing in segment 5, $M_{5,1}$. As the current flowing in the two segments has the same magnitude, frequency and phase ($M_{1,5} = M_{5,1}$), the total mutual inductance is equal to $M_{1,5} + M_{5,1} = 2 \times M_{1,5}$. Looking into the direction that the current flows in these two segments, it can be concluded that the resultant mutual inductance is "positive". The same happens for the segment pairs $2-6$, $3-7$, $4-8$, $5-9$, $6-10$, $7-11$, $8-12$, $9-1$, $10-2$, $11-3$ and $12-4$. However, between segments pairs $1-3$, $1-7$, $1-11$, $5-3$, $5-7$, $5-11$, $9-3$, $9-7$, $9-11$, $2-4$, $2-8$, $2-12$, $6-4$, $6-8$, $6-12$, $10-4$, $10-8$, and $10-12$, the resultant mutual inductance behaves as if it were "negative", since the current i flows in opposite directions in the pair of conductors. This way, the total mutual inductance, M_T, of the coil is given by:

$$\begin{aligned} M_T &= M_+ - M_- \\ M_+ &= 2(M_{1,5} + M_{2,6} + M_{3,7} + M_{4,8} + M_{5,9} + M_{6,10} + M_{7,11} + M_{8,12} + \\ &\quad M_{9,1} + M_{10,2} + M_{11,3} + M_{12,4}) \\ M_- &= 2(M_{1,3} + M_{1,7} + M_{1,11} + M_{5,3} + M_{5,7} + M_{5,11} + M_{9,3} + M_{9,7} + M_{9,11} + \\ &\quad M_{2,4} + M_{2,8} + M_{2,12} + M_{6,4} + M_{6,8} + M_{6,12} + M_{10,4} + M_{10,8} + M_{10,12}) \end{aligned} \tag{2.5}$$

So, to calculate the mutual inductance between the pair of filaments, it is necessary to have into consideration their position in relation to each other. Figure 2.15 shows the general case to calculate the mutual inductance between two parallel segments.

Thus, according to Grover [2.88], the mutual inductance, M, of two parallel filaments can be calculated by:

$$\begin{aligned} M = \frac{\mu_0}{4 \times \pi}[\alpha \sinh^{-1}\frac{\alpha}{d} - \beta \sinh^{-1}\frac{\beta}{d} - \gamma \sinh^{-1}\frac{\gamma}{d} \\ +\delta \sinh^{-1}\frac{\delta}{d} - \sqrt{\alpha^2 + d^2} + \sqrt{\beta^2 + d^2} \\ +\sqrt{\gamma^2 + d^2} - \sqrt{\delta^2 + d^2}] \end{aligned} \tag{2.6}$$

where μ_0 is the vacuum permeability, $\alpha = l + m + \delta$, $\beta = l + \delta$, and $\gamma = m + \delta$. In the case of the filaments being overlapped, the length δ has negative influence. So, in these cases $\alpha = l + m - \delta$, $\beta = l - \delta$, and $\gamma = m - \delta$.

Equation (2.6) remains valid for parallel filaments. Thus, when they are not parallel, as illustrated in the case of Figure 2.16, mutual inductance between them can be calculated by [2.88]:

$$\begin{aligned} M = \frac{\mu_0}{2 \times \pi}\cos\theta[(\mu + l)\tanh^{-1}\frac{m}{R_1 + R_2} \\ +(v + m)\tanh^{-1}\frac{l}{R_1 + R_4} - \mu \tanh^{-1}\frac{m}{R_3 + R_4} \\ -v \tanh^{-1}\frac{l}{R_2 + R_3}] \end{aligned} \tag{2.7}$$

Considering that (2.7) represents the general case of Figure 2.16, l and m correspond to the length of the filaments, while the remaining variables stand for all the relevant distances identified. These variables

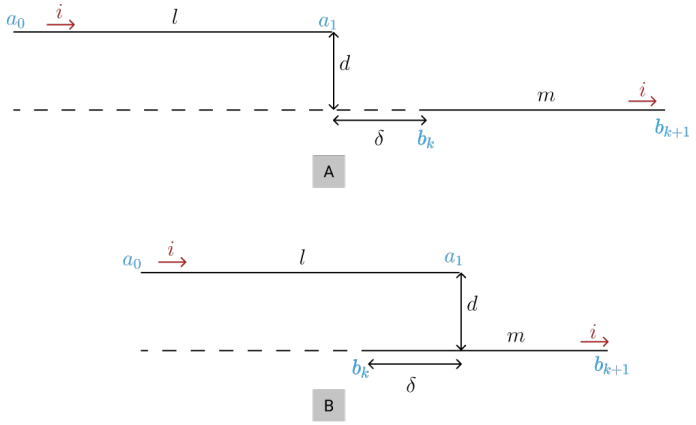

Figure 2.15: Mutual Inductance's general case of two filaments parallels.

can be determined using:

$$2\cos\theta = \frac{\alpha^2}{lm}\alpha^2 = {R_4}^2 - {R_3}^2 + {R_2}^2 - {R_1}^2 \tag{2.8}$$

$$\mu = \frac{[2m^2({R_2}^2 - {R_3}^2 - l^2) + \alpha^2({R_4}^2 - {R_3}^2 - m^2)]l}{4l^2m^2 - \alpha^4} \tag{2.9}$$

$$v = \frac{[2l^2({R_4}^2 - R_3^2 - m^2) + \alpha^2({R_2}^2 - {R_3}^2 - l^2)]m}{4l^2m^2 - \alpha^4} \tag{2.10}$$

$$\begin{aligned} {R_1}^2 &= (\mu + l)^2 + (v + m)^2 - 2(\mu + l)(v + m)\cos\theta \\ {R_2}^2 &= (\mu + l)^2 + v^2 - 2v(\mu + l)\cos\theta \\ {R_3}^2 &= \mu^2 + v^2 - 2\mu v\cos\theta \\ {R_4}^2 &= \mu^2 + (v + m)^2 - 2\mu(v + m)\cos\theta \end{aligned} \tag{2.11}$$

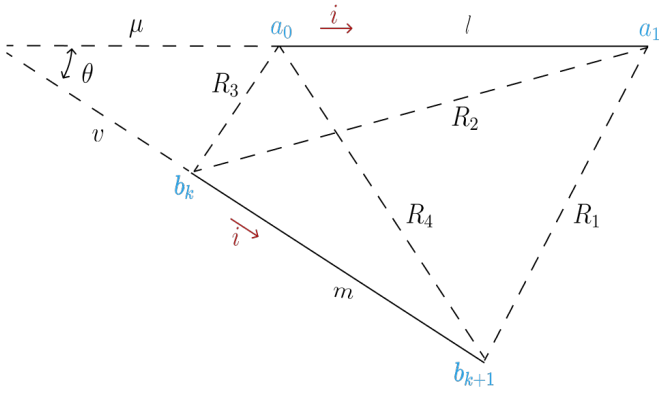

Figure 2.16: Mutual Inductance's general case of two filaments nonparallels.

Based on all the steps explained before, to calculate the inductance of a planar coil by the Greenhouse method, it became clear that the greater the number of turns, the higher is the number of calculations. In a general way, for a square planar coil with N turns, the model will have $4N$ self-inductance terms, $2N^2$ negative mutual inductance terms, and $2N(N-1)$ positive mutual inductance terms. However, nowadays, this increase in calculations is reflected in the order of seconds in the execution time, not being a relevant factor. This way, it is much less time-consuming than a numerical approach, and still does not

require huge computational resources. Despite the complexity of the model, due to its accuracy, it is the method most often chosen to calculate the inductance of planar coils [2.75].

In [2.74], beyond explaining and testing the Greenhouse method, the authors also analyse and compare the accuracy of the results given by Bryan method (Equation 2.12, where the inductance is given in nH) and Terman method (Equation 2.13, where the inductance is given in fH). Both methods present worst results than the Greenhouse method.

$$L = 0.00241(\frac{d_o + d_i}{4})n^{5/3}\ln[4\frac{d_o + d_i}{d_o - d_i}] \tag{2.12}$$

$$L = 10d_oN^2\{180[\log(\frac{2d_o^2}{t+w}) + 5 - \log(9.5d_o)] + 8(0.914 + \frac{0.22(t+w)}{d_o})\} \tag{2.13}$$

In concordance with what is presented in [2.74], in [2.44] a disadvantage that all have in common is identified. These methods are just valid for square and rectangular planar coils. It makes also reference to the methods developed by Wheeler, Gleason, and Olivei, highlighting that they are also limited to one type of shaped coils. In this case, it is to circular planar coils. In [2.74] it is also noted that the method developed by Dill, beyond being limited to square geometries, the coil has to be completely filled.

Mohan S. et al [2.65], despite defending that Greenhouse method is very accurate and that the time taken to calculate inductance is adequate, they also pointed out that it is too complex to implement from scratch for an initial design. Due to that, the authors developed three simple approximated equations, with typical errors of $2-3\%$, Modified Wheeler Formula, Expression based on Current Sheet Approximation, and Data Fitted Monomial Expression. These approximation formulas were validated for regular coils with an outside diameter (d_{out}) between $100/480$ μm, an inside diameter (d_{in}) between $0.1-0.9d_{out}$, a wire width (w) between 2 μm and $0.3d_{out}$, a space between turns (s) from 2 μm to $3d_{out}$, and an inductance value between 0.5 and 100 nH.

The modified Wheeler approximation formula is derived from the Wheeler's formulas. In [2.89], Wheeler presented several formulas for the calculation of the inductance of helical coils with one or more layers, and Mohan S. et al proposed an approximation to make Wheeler's formulas valid for planar coils [2.65]. This way, they derived an equation that is dependent on two coefficients (k_1 and k_2) related to the coil layout, the vacuum permeability, and some geometric parameters of the coil such as the number of turns (n), its average diameter (d_{avg}), and fill ratio (ρ). Table 2.3 shows the valid coil layouts and the values of

the corresponding coefficients to apply in:

$$L = k_1 \mu_0 \frac{n^2 d_{avg}}{1 + k_2 \rho} \tag{2.14}$$

Table 2.3: Coefficients for Modified Wheeler Formula [2.65].

Layout	k_1	k_2
Square	2.34	2.75
Hexagonal	2.33	3.82
Octagonal	2.25	3.55

Since this approximation formula depends only on the average diameter and the fill ratio of the coil, it is not sensible to different configurations of s and w when the values of d_{avg} and ρ are the same. In these cases, the error associated with this model increases.

The Current Sheet Approximation formula is based on the approximation of the sides of the coil to the current sheets of equal density using electromagnetic principles. In this formula, the calculation of the auto and mutual inductances between the coil wires is performed considering concepts of geometric mean distance (GMD), the arithmetic mean distance (AMD), and the arithmetic mean square distance (AMSD)[2.65]. Due to this approach, the greater is the ratio between the space between turns and the track's width, the larger are the errors between this formula and the real coil inductance. Table 2.4 shows the coil layouts for which this approach is valid and the corresponding coefficients to be applied:

$$L = \frac{\mu_0 n^2 d_{avg} c_1}{2} (\ln(\frac{c_2}{\rho}) + c_3 \rho + c_4 \rho) \tag{2.15}$$

where, d_{avg} is the average diameter, n the number of turns, and ρ is the fill ratio ($\rho = \frac{d_{out} - d_{in}}{d_{out} + d_{in}}$).

Table 2.4: Coefficients for Current Sheet Approximation Formula [2.65].

Layout	c_1	c_2	c_3	c_4
Square	1.27	2.07	0.18	0.13
Hexagonal	1.09	2.23	0.00	0.17
Octagonal	1.07	2.29	0.00	0.19
Circle	1.00	2.46	0.00	0.20

The expression Data Fitted Monomial was developed using the authors' database of inductors, athwart data-fitting techniques. For that reason, when the characteristics of the coil under analysis are different from those of the database, the error between the formula and the coil inductance can be significant. The coil geometries that can be used and the respective coefficients are presented in Table 2.5. The

inductance formula relies on this set of geometry dependant coefficients and in the coil's parameters to calculate the self inductance:

$$L = \beta d_o^{\alpha_1} w^{\alpha_2} d_{avg}^{\alpha_3} n^{\alpha_4} s^{\alpha_5} \tag{2.16}$$

where: d_{out} corresponds to the outer-diameter, w to the turn's width, d_{avg} to the average diameter ($d_{avg} = \frac{d_{out}+d_{in}}{2}$), d_{in} to the inner-diameter, n to the number of turns, and s to the space between turns.

Table 2.5: Coefficients for Data Fitted Monomial Formula [2.65].

Layout	β^*	α_1	α_2	α_3	α_4	α_5
Square	1.62	−1.21	−0.147	2.40	1.78	−0.030
Hexagonal	1.28	−1.24	−0.174	2.47	1.77	−0.049
Octagonal	1.33	−1.21	−0.163	2.43	1.75	−0.049

*Values x10^{-3}.

Beyond the simplicity and accuracy of these three approximate formulas, they have also the advantage, that from the initial specifications, like outer coil size (d_o), the number of turns (n), turn width (w), and space between turns (s), they can provide directly the coil inductance. In this way, they become more interactive, since by just modifying one of the parameters, the designer can see immediately its impact on the inductance of the coils. As visible in Tables 2.3, 2.4, and 2.5, each one of the formulas is suitable for several regular spiral coils geometries. The one that is valid for more regular coil geometries is the Current Sheet Approximation formula (circle, square, hexagonal, and octagonal).

In [2.65], Sunderarajan et al also compared the results obtained by these three formulas, with the ones obtained by ASITIC®field solver simulator. Both results are in agreement, with typical errors lower than 3%. The authors pointed out that there are some uncertainties related to the fabrication process, like the thickness of the oxide. Since this process can cause a variation in the coil inductance in the same order of the formulas error, it shows that it is not worth investing in more complex formulas with higher accuracy for the type of coils they are valid for. This way, these formulas are adequate for being used during design and optimization phases.

Despite the article [2.65] being from 1999, the expressions presented have been used over the years until the present to estimate the coil's self-inductance. From the literature survey, it is possible to state that the Current Sheet Approximation formula is the most used [2.44], [2.66]–[2.72], [2.87], [2.90], [2.91], followed by the Modified Wheeler [2.66], [2.76] and the Data Fitted Monomial [2.73], [2.92]. The Current Sheet Approximation formula stands out from other formulas because it has has a good accuracy, and it is valid for more coil geometries.

2.2.2 Inductance of a Multi-layer Planar Coil

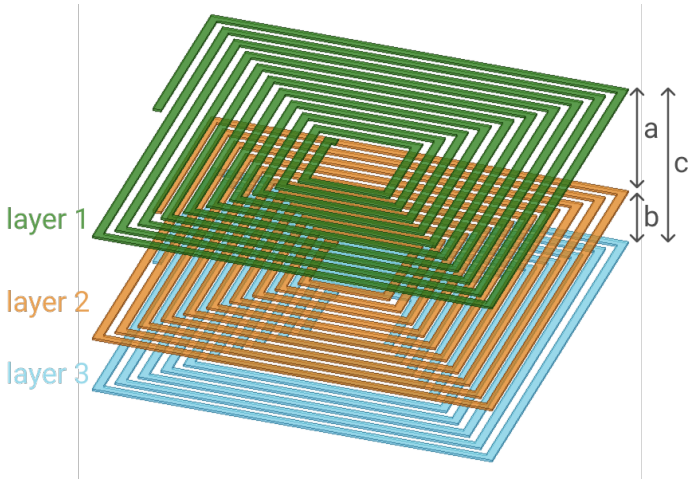

Figure 2.17: Example of a planar 3-layer square coil.

The inductance of a multi-layer planar coil (Figure 2.17) depends on the parameterization of the coil at each layer (geometry, number of turns, space between turns, wire width, internal and external diameter) and the distance between them. Thus, to obtain the total inductance of a 2-layer coil it is necessary to sum the self-inductances of each layer, and to sum or subtract, depending on the direction of the current, the double of the mutual inductance between the layers [2.67], [2.68], [2.74]:

$$L_T = L_1 + L_2 \pm 2M \tag{2.17}$$

where, L_T is the total inductance, L_1 and L_2 are the values of self-inductance of the coils in each layer, and M is the mutual inductance between the two coils, that can be calculated through:

$$M = K\sqrt{L_1 L_2}. \tag{2.18}$$

where, K is the coupling coefficient between the coils of each layer. Currently, to perform these calculations, the combination of the coupling coefficient with the self-inductance values obtained by the previously mentioned approximation formulas is being used [2.87], [2.93]. Typically, this coefficient is either calculated analytically [2.66] or using a numerical model [2.72], or it can be measured experimentally [2.94]. Equation 2.19 is the analytical expression that is most commonly used to calculate the coupling coefficient between coils [2.66]–[2.68]. It was derived experimentally by Zhao J. [2.67] through multi-layer coils with the distance between adjacent layers varying from 0.75 mm to 2 mm, considering coils with 5 to 20 turns

[2.66]–[2.68]. This equation has the particularity of being valid only within the range that was derived, and the coils of all layers must be equal and perfectly aligned.

$$\begin{gathered} M = 2K_c\sqrt{L_1L_2} \\ K_c = \frac{n^2}{0.64[(0.184X^3 - 0.525X^2 + 1.038X + 1.001)(1.67n^2 - 5.84n + 65)]} \end{gathered} \tag{2.19}$$

where, K_c is the coupling factor, n the number of coil's turns, and X the distance between the layers in mm [2.66]–[2.68].

For the case of a multi-layer coil, the coupling between each pair of layers must be calculated, in this way, through the proposal of Zhao J. [2.67], Equation 2.19 has be applied between each pair of layers. Taking the example of the multi-layer coil visible in Figure 2.17, in order to calculate the total mutual inductance of the coil, it is necessary to calculate the mutual inductance between layer $1-2$, $1-3$ and $2-3$. To do it, it has to be determined the coupling coefficient between these layers by:

$$\begin{aligned} K_{c12} &= \frac{n^2}{0.64[(0.184a^3 - 0.525a^2 + 1.038a + 1.001)(1.67n^2 - 5.84n + 65)]} \\ K_{c13} &= \frac{n^2}{0.64[(0.184b^3 - 0.525b^2 + 1.038b + 1.001)(1.67n^2 - 5.84n + 65)]} \\ K_{c23} &= \frac{n^2}{0.64[(0.184c^3 - 0.525c^2 + 1.038c + 1.001)(1.67n^2 - 5.84n + 65)]} \end{aligned} \tag{2.20}$$

Thus, as the coils in all the layers are equal, $L_1 = L_2 = L_3$, so $M = 2K_c\sqrt{L_1L_2} = 2K_cL_1$ and the total mutual inductance can be obtained through:

$$\begin{aligned} M &= 2K_{c12}L_1 + 2K_{c13}L_1 + 2K_{c23}L_1 \\ &= 2L_1(K_{c12} + K_{c13} + K_{c23}) \end{aligned} \tag{2.21}$$

Then, it follows the application of Equation 2.17 in order to obtain the total inductance. Considering the example mentioned before, and assuming that the current in the 3 layers has the same direction, the total inductance of the 3-layer coil is given by:

$$L_T = 6L_1 + 4L_1(K_{c12} + K_{c13} + K_{c23}) \tag{2.22}$$

Despite this approach, the mutual inductance of a multi-layer coil can be calculated following the Grover

equations, calculating the inductance between all the segments of the several layers of the coil. It is much more complex than the approach proposed by Zhao J. [2.67]. However, there are no limitations about dimensions or geometries of the coils. Despite not having these limitations, the implementation is not simple when it is necessary to calculate a multi-layer coil inductance, specially when there is a greater number of coil segments. These facts usually cause the coupling coefficient to be calculated experimentally or using a FEM software rather than using these equations.

In what concerns to the analytical models presented to calculate the self-inductance of a 1-layer planar coil, despite the Greenhouse method being recognized as the most accurate, the formulas commonly used in the literature are the Current Sheet Approximation, the Modified Wheeler and the Data Fitted Monomial, since they can be used directly, only replacing their variables with the values of the coil parameters. Thus, it can be concluded that defining the design of a 1-layer planar coil using one of the three approximation formulas developed by Mohan S. et al is a simple, and fast process, with no need for high computational resources. However, as previously stated, these formulas are only valid for certain fixed coil geometries and do not have the same accuracy as a FEM simulation. It can even be said that its accuracy is affected by the geometric configuration of the coil under analysis. For example, in the case of the Data Fitted Monomial expression, as its constants are derived from a database of coils, if the dimensions of the coil that is being analyzed are out of the range of the database, the results will have higher errors. In the case of Current Sheet Approximation, its result deteriorates with the increase of the ratio between the space between turns, and the width of the inductor ($\frac{s}{w}$), the error obtained can be as high as 8%. For the case when $s \leq 3w$, and in the case of the Modified Wheeler, by analyzing the Equation 2.14, it can be noted that it just has into consideration the number of turns of the coil, its average diameter, and its fill ratio. So, for all the combinations that the sum of the wire's width and the space between turns is the same, keeping the same number of turns and length of the inner segment, the value of the auto-inductance calculated by it will be the same.

Regarding the calculation of mutual inductance between multi-layer coils, one of the three approximation equations mentioned before can be used together with an auxiliary equation, derived by Zhao J., to determine the coupling coefficient between layers. The simplicity, speed, and low cost of the analytical inductance calculation process, for 1-layer planar coils, can, most of the time, be achieved by using these models found in the literature. However, the limitation of the coupling coefficient equation itself, which is only valid for coils with 5 to 20 turns and with adjacent layers spaced between 0.75 mm and 2 mm, does not allow these solutions to be considered viable for all configurations of multi-layer planar coil calculation. It also has the limitation that it can not be used to calculate the coupling between coils

with different configurations (geometry, number of turns, space between turns, wire width, internal and external diameter).

Due to the growing interest in planar coils, and these limitations, it is advantageous to have a more versatile tool than the generic expressions usually used as an alternative to FEM simulations. The ideal scenario would be to combine speed, precision, easy interaction, and understanding, adding versatility in terms of geometry yet. This way, it would be possible to analyze coils with any geometry different than square, hexagonal, octagonal, and circular, with several turns and layers. The next section describes the proposed tool that meets those requirements.

References

[2.1] J. Fraden, Handbook of Modern Sensors. New York, NY: Springer New York, 2010, pp. 279–326, isbn: 978-1-4419-6465-6. doi: 10.1007/978-1-4419-6466-3. [Online]. Available: http://link.springer.com/10.1007/978-1-4419-6466-3.

[2.2] Electronics Tutorials, Position Sensors, 2014. [Online]. Available: https://www.electronics-tutorials.ws/io/io_2.html.

[2.3] Electronics Hubs, Position Sensors, 2015. [Online]. Available: https://www.electronicshub.org/position-sensors/#top.

[2.4] C. Ebbesson, "Comparative study of different rotary position sensors for electrical machines used in an hybrid electric vehicle application", PhD thesis, Lund, 2011, pp. 23–25. [Online]. Available: https://www.iea.lth.se/publications/MS-Theses/Full%20document/5287_full_ducument_Rotary%20_Position_Sensors.pdf.

[2.5] J. Leuckfeld and H. Oyrer, "Addressing the Challenges of Position Sensor Solutions in Safety Critical", in IDT Inc. Technical Education Webinar Series, 2017, pp. 1–26. [Online]. Available: https://www.slideshare.net/HeinzOyrer/addressing-the-challenges-of-position-sensor-solutions-in-safety-critical-automotive-applications-idt-webinar-january-25-2017-slideshare.

[2.6] H. Zangl, L.-M. Faller, and W. Granig, "Optimal design of angular position sensors", COMPEL - The international journal for computation and mathematics in electrical and electronic engineering, vol. 36, no. 5, pp. 1372–1385, Sep. 2017, issn: 0332-1649. doi: 10.1108/COMPEL-02-2017-0099. [Online]. Available: http://www.emeraldinsight.com/doi/10.1108/COMPEL-02-2017-0099.

[2.7] W. Y. Du, Resistive, Capacitive, Inductive, and Magnetic Sensor Technologies - Winncy Y. Du - Google Books. New York, NY: CRC Press, 2015, p. 408, isbn: 9781439812495. [Online]. Available: https://books.google.de/books?id=iZnLBQAAQBAJ&pg=PA99&lpg=PA99&dq=classification+of+materials+based+on+capacitive+sensing&source=bl&ots=VgM8TRiPQx&sig=iGg5Y_iy2lk_aE7O3SR0UfpBgPY&hl=de&sa=X&ved=0ahUKEwjAi4_bjbjTAhWSZlAKHZrpDBUQ6AEIODAC#v=onepage&q=classif.

[2.8] B. Luce and K. Rahnamai, "Controller design for a multi-fan hovering system", in Proceedings: Electrical Insulation Conference and Electrical Manufacturing and Coil Winding Conference (Cat. No.01CH37264), Cincinnati, OH, USA: IEEE, 2001, pp. 311–317, isbn: 0-7803-7180-1. doi: 10.1109/EEIC.2001.965643. [Online]. Available: http://ieeexplore.ieee.org/document/965643/.

[2.9] M. Parnichkun, W. Pongern, and T. Jearsiripongkul, "Development of a force-displacement controlled medical tele-analyzer", in ISIE 2001. 2001 IEEE International Symposium on Industrial Electronics Proceedings (Cat. No.01TH8570), vol. 3, Pusan, South Korea: IEEE, 2001, pp. 1978–1981, isbn: 0-7803-7180-1. doi: 10.1109/ISIE.2001.932016. [Online]. Available: http://ieeexplore.ieee.org/document/932016/.

[2.10] E. Purwanto and S. Toyama, "Control method of a spherical ultrasonic motor", in Proceedings 2003 IEEE/ASME International Conference on Advanced Intelligent Mechatronics (AIM 2003), vol. 2, IEEE, 2003, pp. 1321–1326, isbn: 0-7803-7759-1. doi: 10.1109/AIM.2003.1225534. [Online]. Available: http://ieeexplore.ieee.org/document/1225534/.

[2.11] B. Rosengrant and B. Kostik, Potentiometers: A Proven Position Sensing Solution that Every Engineer Needs to Consider in Modern Designs, 2011. [Online]. Available: https://www.sensorsmag.com/embedded/potentiometers-a-proven-position-sensing-solution-every-engineer-needs-to-consider-modern.

[2.12] M. Howard, Choosing the right position Sensor. [Online]. Available: https://www.zettlex.com/articles/choosing-right-position-sensor/ (visited on 07/30/2018).

[2.13] A. Othman, N. Hamzah, Z. Hussain, R. Baharudin, A. D. Rosli, and A. I. C. Ani, "Design and development of an adjustable angle sensor based on rotary potentiometer for measuring finger flexion", Proceedings - 6th IEEE International Conference on Control System, Computing and Engineering, ICCSCE 2016, no. November, pp. 569–574, 2017. doi: 10.1109/ICCSCE.

2016.7893640. [Online]. Available: https://ieeexplore.ieee.org/document/7893640/.

[2.14] M. Howard, Inductive versus magnetic position sensors.

[2.15] MultiDimension Technology Co. Ltd. and MultiDimension Technology Co.Ltd., MR Sensor Technology, 2015. [Online]. Available: http://www.dowaytech.com/en/1776.html%20https://web.archive.org/web/20180301175414/http://www.dowaytech.com/en/1776.html.

[2.16] E. Ramsden, "Hall-Effect Sensors: Theory and Application. Newnes", in Hall-Effect Sensors: Theory and Application. Newnes, second edi, Elsevier, 2006, ch. Chapter 1-, pp. 1–2, isbn: 978-0-7506-7934-3.

[2.17] Honeywell, How to apply Honeywell APS00B Angular Position Sensor ICs, 2011.

[2.18] Y. Cai, Y. Zhao, X. Ding, and J. Fennelly, Magnetometer basics for mobile phone applications, 2012. [Online]. Available: http://www.memsic.com/technology/amr-magnetic-sensors.cfm.

[2.19] J. Gächter, J. Fabian, M. Hirz, A. Schmidhofer, and H. Lanzenberger, "Evaluation of Angular Sensor Systems for Rotor Position Sensing of Automotive Electric Drives", in Advanced Microsystems for Automotive Applications 2014, J. Fischer-Wolfarth and G. Meye, Ed., Springer, Cham, 2014, pp. 277–286, isbn: 978-3-319-08087-1. doi: 10.1007/978-3-319-08087-1{_}25. [Online]. Available: http://link.springer.com/10.1007/978-3-319-08087-1_25.

[2.20] NVE Corporation, Application Notes for GMR Sensors. [Online]. Available: https://www.nve.com/Downloads/apps.pdf.

[2.21] J. Paul, C. Schnieders, J. Traute, R. Lehndorff, A. Conca, B. Leven, B. Hillebrands, F. Casper, and G. Jakob, "Sensors Based on Tunnel Magnetoresistance - New Technology, New Opportunities", in AMA Conferences, Nürnberg, Germany, 2015, pp. 234–239. doi: 10.5162/SENSOR2015/B3.2. [Online]. Available: http://www.ama-science.org/proceedings/details/1921.

[2.22] M. Howard, A Comparison of Inductive and Capacitive Position Sensors Operating Principles – Capacitive Sensors. doi: 2018-07-30. [Online]. Available: https://www.zettlex.com/articles/a-comparison-of-inductive-and-capacitive-position-sensors/.

[2.23] M. A. Howard, "Next-generation inductive transducers for position measurement", W. E. Thompson and P. F. McManamon, Eds., vol. 8395, International Society for Optics and Photonics, Jun.

2012, 83950K. doi: 10.1117/12.917041. [Online]. Available: http://proceedings.spiedigitallibrary.org/proceeding.aspx?doi=10.1117/12.917041.

[2.24] Z. Zhang, F. Ni, Y. Dong, C. Guo, M. Jin, and H. Liu, "A Novel Absolute Magnetic Rotary Sensor", IEEE Transactions on Industrial Electronics, vol. 62, no. 7, pp. 4408–4419, Jul. 2015, issn: 0278-0046. doi: 10.1109/TIE.2014.2387794. [Online]. Available: http://ieeexplore.ieee.org/document/7001599/.

[2.25] B. Wang, K. H. Teo, and P. Orlik, "An accurate contactless position sensor with planar resonators", in 2016 IEEE SENSORS, IEEE, Oct. 2016, pp. 1–3, isbn: 978-1-4799-8287-5. doi: 10.1109/ICSENS.2016.7808939. [Online]. Available: http://ieeexplore.ieee.org/document/7808939/.

[2.26] A. S. A. Kumar, B. George, and S. C. Mukhopadhyay, "Technologies and Applications of Angle Sensors: A Review", IEEE Sensors Journal, vol. 21, no. 6, pp. 7195–7206, 2020, issn: 1530-437X. doi: 10.1109/jsen.2020.3045461.

[2.27] B. S. Nauduri and G. Shaga, "A novel approach of using a planar inductive position sensor for the Permanent magnet synchronous motor control application", in 2018 IEEE Sensors Applications Symposium (SAS), IEEE, Mar. 2018, pp. 1–5, isbn: 978-1-5386-2092-2. doi: 10.1109/SAS.2018.8336708. [Online]. Available: http://ieeexplore.ieee.org/document/8336708/.

[2.28] P. Ripka, J. Blažek, M. Mirzaei, P. Lipovský, M. Šmelko, and K. Draganová, "Inductive position and speed sensors", Sensors (Switzerland), vol. 20, no. 1, 2020, issn: 14248220. doi: 10.3390/s20010065.

[2.29] G. Leibovich and S. Senanian, "Development of Variable Reluctance Resolver for Position Feedback", in Proceedings of the 41st Aerospace Mechanisms Symposium, Jet Propulsion Laboratory, Pasadena, California, 2012, pp. 141–146. [Online]. Available: http://esmats.eu/amspapers/pastpapers/pdfs/2012/leibovich.pdf.

[2.30] L. Sun, J. Zou, and Y. Lu, "New variable-reluctance resolver for rotor-position sensing", in 2004 IEEE Region 10 Conference TENCON 2004., vol. D, Chiang Mai, Thailand: IEEE, pp. 5–8, isbn: 0-7803-8560-8. doi: 10.1109/TENCON.2004.1414855. [Online]. Available: http://ieeexplore.ieee.org/document/1414855/.

[2.31] J. Oshino and I. Sasada, "Thin resolver using the easy magnetization axis of the grain-oriented silicon steel as an angle indicator", AIP Advances, vol. 7, no. 056662, pp. 1–7, 2017, issn:

2158-3226. doi: 10.1063/1.4977494. [Online]. Available: http://aip.scitation.org/doi/10.1063/1.4977494.

[2.32] T. R. Kuphaldt, Lessons In Electric Circuits, Volume II – AC; Sixth, Koro Press, Ed. 2006, pp. 398–401. [Online]. Available: https://www.allaboutcircuits.com/assets/pdf/alternating-current.pdf.

[2.33] M. Ghafarzadeh, A. Kamali E., A. D. Aliabad, R. Abedini, and M. A. Tajeddini, "A new brushless synchro with look-up table error compensation", International Journal of Numerical Modelling: Electronic Networks, Devices and Fields, vol. 29, no. 4, pp. 577–591, Jul. 2016, issn: 08943370. doi: 10.1002/jnm.2113. [Online]. Available: http://doi.wiley.com/10.1002/jnm.2113.

[2.34] D. Pazouki, M. Ghafarzadeh, R. Abedini, A. D. Aliabad, and E. A. Kamali, "A novel brushless synchro: Operation principle and experimental results", in 2013 21st Iranian Conference on Electrical Engineering (ICEE), IEEE, May 2013, pp. 1–6, isbn: 978-1-4673-5634-3. doi: 10.1109/IranianCEE.2013.6599625. [Online]. Available: http://ieeexplore.ieee.org/document/6599625/.

[2.35] M. Howard, Choosing the right position Sensor. [Online]. Available: https://www.zettlex.com/articles/choosing-right-position-sensor/.

[2.36] J. G. Webster, H. Eren, and H. Eren, Measurement, Instrumentation, and Sensors Handbook, Second Edition, H. Eren, Ed. CRC Press, Jan. 2014, isbn: 978-1-4398-4888-3. doi: 10.1201/b15474. [Online]. Available: https://www.taylorfrancis.com/books/9781439848890.

[2.37] Q. Zhou, Y. Zhang, Y. Zhou, and D. Yu, "Error Analysis and Compensation Method Research of Airborne Reluctance RVDTs", in Proceedings of the First Symposium on Aviation Maintenance and Management-Volume I, J Wang, Ed., Springer, Berlin, Heidelberg, 2014, pp. 199–207. doi: 10.1007/978-3-642-54236-7{_}22. [Online]. Available: http://link.springer.com/10.1007/978-3-642-54236-7_22.

[2.38] J.-K. Lee, Y.-H. Ko, and S.-G. Lee, "Calibration technique for sensitivity variation in RVDT type accelerator position sensor", in 2013 IEEE International Instrumentation and Measurement Technology Conference (I2MTC), IEEE, 2013, pp. 1512–1516, isbn: 978-1-4673-4623-8. doi: 10.1109/I2MTC.2013.6555666. [Online]. Available: http://ieeexplore.ieee.org/lpdocs/epic03/wrapper.htm?arnumber=6555666.

[2.39] Y. Zhou, Y. Zhang, C. Zhang, and Q. Zhou, "Design and Analysis of High-Reliability Universal Airborne RVDTs", in Proceedings of the First Symposium on Aviation Maintenance and Management-Volume I, J. Wang, Ed., Springer, Berlin, Heidelberg, 2014, pp. 189–197. doi: 10.1007/978-3-642-54236-7{_}21. [Online]. Available: http://link.springer.com/10.1007/978-3-642-54236-7_21.

[2.40] Lion Precision, "Differences Between Capacitive and Eddy-Current Sensors", Tech. Rep., 2009, p. 9. [Online]. Available: https://cdn.thomasnet.com/ccp/01248493/183696.pdf.

[2.41] V. Aviation, Eddy Current Electromagnetic Induction. [Online]. Available: http://www.victor-aviation.com/Eddy-Current-Inspection.php.

[2.42] Innospection, Innospection, 2013. [Online]. Available: http://www.innospection.com/pdfs/Eddy%20Current%20Theory.pdf.

[2.43] B. George, Z. Tan, and S. Nihtianov, "Advances in Capacitive, Eddy Current, and Magnetic Displacement Sensors and Corresponding Interfaces", IEEE Transactions on Industrial Electronics, vol. 64, no. 12, pp. 9595–9607, Dec. 2017, issn: 0278-0046. doi: 10.1109/TIE.2017.2726982. [Online]. Available: http://ieeexplore.ieee.org/document/7979582/.

[2.44] M. Pospisilik, L. Kouril, I. V. O. Motyl, and M. Adamek, "Single and Double Layer Spiral Planar Inductors Optimisation with the Aid of Self-Organising Migrating Algorithm", in Recent Advances in Signal Processing, Computational Geometry and Systems Theory, Florence, 23 August 2011 - 25 August 2011, 2011, pp. 272–277, isbn: 9781618040275.

[2.45] Cambridge Integrated Circuits Ltd, Resonant Inductive Position Sensors, 2014. [Online]. Available: https://www.sensorland.com/.

[2.46] T. Karimov, O. Druzhina, A. Karimov, and D. Butusov, "Axial Movement Sensor Based on Chaotic Oscillator and Planar Coil", in Conference of Open Innovation Association, FRUCT, vol. 2020-April, Yaroslav (Russia), 23 April 2020 - 24 April 2020, 2020, pp. 130–135, isbn: 9789526924427. doi: 10.23919/FRUCT48808.2020.9087471.

[2.47] E. Automotive, "Inductive through-shaft position sensor for e-motor", Tech. Rep. 4, 2013, pp. 160–182. [Online]. Available: https://www.efiautomotive.com/en/produits/capteur-de-position-inductif-trough-shaft-pour-e-motor/.

[2.48] Hella, "Angular Position Sensors Single and double sensors", [Online]. Available: https://www.hella.com/powersports/assets/media_global/627_Angular_Position_Sensors_KI_HELLA_EN.pdf.

[2.49] Sadri Brojaj, MOTOR POSITION SENSORS. [Online]. Available: https://www.hella.com/microsite-electronics/en/Motor-Position-Sensors-1483.html.

[2.50] Renesas Electronic Corporation, "IPS2200 INDUCTIVE POSITION SENSORS A New Era in Motor Commutation", RENESAS, Tech. Rep., pp. 5–6. [Online]. Available: https://www.renesas.com/us/en/products/sensor-products/position-sensors.

[2.51] Renesas Electronics Corporation, "IPS2200 INDUCTIVE POSITION SENSORS A New Era in Motor Commutation", Renesas, Tech. Rep., pp. 5–6. [Online]. Available: idt.com/position.

[2.52] A. K. Palit, "Frequency Response Modeling of Inductive Position Sensor with Finite Element Tools", 2014.

[2.53] M. Kisic, N. Blaz, K. Babkovic, L. Zivanov, and M. Damnjanovic, "Inductive tangential displacement sensor", in 2016 39th International Spring Seminar on Electronics Technology (ISSE), IEEE, May 2016, pp. 433–438, isbn: 978-1-5090-1389-0. doi: 10.1109/ISSE.2016.7563235. [Online]. Available: http://ieeexplore.ieee.org/document/7563235/.

[2.54] N. Misron, L. Q. Ying, R. N. Firdaus, N. Abdullah, N. F. Mailah, and H. Wakiwaka, "Effect of inductive coil shape on sensing performance of linear displacement sensor using thin inductive coil and pattern guide", Sensors, vol. 11, no. 11, pp. 10 522–10 533, 2011, issn: 14248220. doi: 10.3390/s111110522.

[2.55] M. Rahal and A. Demosthenous, "An ASIC Front End for Planar High-Frequency Contactless Inductive Position Sensors", IEEE Transactions on Instrumentation and Measurement, vol. 58, no. 9, pp. 3021–3030, Sep. 2009, issn: 0018-9456. doi: 10.1109/TIM.2009.2016819. [Online]. Available: http://ieeexplore.ieee.org/document/4982738/.

[2.56] D. Ito, T. Fujioka, H. Wakiwaka, K. Tashiro, H. Yajima, Y. Manta, T. Kanazawa, and N. Fujiwara, "Simplified calculation method of impedance of a planar coil in consideration of the influence depending on eddy current", Journal of the Japan Society of Applied Electromagnetics and Mechanics, vol. 21, no. 2, pp. 234–239, 2013.

[2.57] S. Yamada, K. Chomsuwan, Y. Fukuda, M. Iwahara, H. Wakiwaka, and S. Shoji, "Eddy-current testing probe with spin-valve type GMR sensor for printed circuit board inspection", IEEE Transactions on Magnetics, vol. 40, no. 4 II, pp. 2676–2678, 2004, issn: 00189464. doi: 10.1109/TMAG.2004.829254.

[2.58] D. Kacprzak, T. Taniguchi, K. Nakamura, S. Yamada, and M. Iwahara, "Novel eddy current testing sensor for the inspection of printed circuit boards", IEEE Transactions on Magnetics, vol. 37, no. 4 I, pp. 2010–2012, 2001, issn: 00189464. doi: 10.1109/20.951037.

[2.59] R. J. Ditchburn and S. K. Burke, “Planar rectangular spiral coils in eddy-current non-destructive inspection”, NDT and E International, vol. 38, no. 8, pp. 690–700, 2005, issn: 09638695. doi: 10.1016/j.ndteint.2005.04.001.

[2.60] D. E. o. T. d. Aguiam, “Heterodyning Non Destructive Testing Electronic System Based on Eddy Currents”, PhD thesis, Técnico Lisboa, 2013, p. 92.

[2.61] Z. Zhang, Y. Dong, F. Ni, M. Jin, and H. Liu, “A Method for Measurement of Absolute Angular Position and Application in a Novel Electromagnetic Encoder System”, Journal of Sensors, vol. 2015, pp. 1–10, May 2015, issn: 1687-725X. doi: 10.1155/2015/503852. [Online]. Available: http://www.hindawi.com/journals/js/2015/503852/.

[2.62] A. S. Anil Kumar, B. George, and S. C. Mukhopadhyay, “An eddy current based non-contact displacement sensor”, in I2MTC 2020 - International Instrumentation and Measurement Technology Conference, Proceedings, Dubrovnik, Croatia, 25–28 May, 2020, pp. 1–6, isbn: 9781728144603. doi: 10.1109/I2MTC43012.2020.9128506.

[2.63] N. Anandan, A. Varma Muppala, and B. George, “A Flexible, Planar-Coil-Based Sensor for Through-Shaft Angle Sensing”, IEEE Sensors Journal, vol. 18, no. 24, pp. 10 217–10 224, 2018, issn: 1530437X. doi: 10.1109/JSEN.2018.2874065.

[2.64] M. Chen, M. Araghchini, K. K. Afridi, J. H. Lang, C. R. Sullivan, and D. J. Perreault, “A Systematic Approach to Modeling Impedances and Current Distribution in Planar Magnetics”, IEEE Transactions on Power Electronics, vol. 31, no. 1, pp. 560–580, Jan. 2016, issn: 0885-8993. doi: 10.1109/TPEL.2015.2411618. [Online]. Available: http://ieeexplore.ieee.org/document/7058353/.

[2.65] S. S. Mohan, M. D. M. Hershenson, S. P. Boyd, and T. H. Lee, “Simple accurate expressions for planar spiral inductances”, IEEE Journal of Solid-State Circuits, vol. 34, no. 10, pp. 1419–1424, 1999, issn: 00189200. doi: 10.1109/4.792620.

[2.66] M. Ulvr, “Design of PCB search coils for AC magnetic flux density measurement”, AIP Advances, vol. 8, no. 4, 2018, issn: 21583226. doi: 10.1063/1.4991643.

[2.67] J. Zhao, “A new calculation for designing multilayer planar spiral inductors”, Edn, vol. 55, no. 14, pp. 37–40, 2010, issn: 00127515.

[2.68] A. Nejadpak, M. R. Barzegaran, A. Sarikhani, and O. A. Mohammed, “Design of planar inductor based Z-source inverter for residential alternate energy sources”, Conference Proceedings - IEEE Applied Power Electronics Conference and Exposition - APEC, pp. 1698–1703, 2011. doi: 10.1109/APEC.2011.5744824.

[2.69] C. Pacurar, V. Topa, C. Munteanu, A. Racasan, and C. Hebedean, "Spiral inductors inductance computation and layout optimization", in EPE 2012 - Proceedings of the 2012 International Conference and Exposition on Electrical and Power Engineering, Iasi, Romania, 25–27 October, 2012, pp. 699–704, isbn: 9781467350013. doi: 10.1109/ICEPE.2012.6463850.

[2.70] N. Lazarus, C. D. Meyer, S. S. Bedair, H. Nochetto, and I. M. Kierzewski, "Multilayer liquid metal stretchable inductors", Smart Materials and Structures, vol. 23, no. 8, 2014, issn: 1361665X. doi: 10.1088/0964-1726/23/8/085036.

[2.71] J. M. Lopez-Villegas, N. Vidal, and J. A. Del Alamo, "Optimized toroidal inductors versus planar spiral inductors in multilayered technologies", IEEE Transactions on Microwave Theory and Techniques, vol. 65, no. 2, pp. 423–431, 2017, issn: 00189480. doi: 10.1109/TMTT.2016.2645571.

[2.72] C. Pacurar, V. Topa, A. Giurgiuman, C. Munteanu, C. Constantinescu, M. Gliga, and S. Andreica, "The Construction of a Wireless Power Supply System using Planar Spiral Inductors", in Proceedings of 2019 8th International Conference on Modern Power Systems, MPS 2019, Cluj-Napoca, Cluj, Romania, 21–23 May: IEEE, 2019, pp. 1–6, isbn: 9781728107509. doi: 10.1109/MPS.2019.8759779.

[2.73] S. Musunuri and P. Chapman, "Multi-layer spiral inductor design for monolithic DC-DC converters", in 38th IAS Annual Meeting on Conference Record of the Industry Applications Conference, 2003., vol. 2, IEEE, 2003, pp. 1270–1275, isbn: 0-7803-7883-0. doi: 10.1109/IAS.2003.1257713. [Online]. Available: http://ieeexplore.ieee.org/document/1257713/.

[2.74] H. Greenhouse, "Design of Planar Rectangular Microelectronic Inductors", IEEE Transactions on Parts, Hybrids, and Packaging, vol. 10, no. 2, pp. 101–109, Jun. 1974, issn: 0361-1000. doi: 10.1109/TPHP.1974.1134841. [Online]. Available: http://ieeexplore.ieee.org/document/1134841/.

[2.75] C. Patrick Yue and S. Simon Wong, "Physical modeling of spiral inductors on silicon", IEEE Transactions on Electron Devices, vol. 47, no. 3, pp. 560–568, 2000, issn: 00189383. doi: 10.1109/16.824729.

[2.76] Q. Xiao, T. Luo, Y. Shi, D. Chen, H. Ye, S. Hu, and Z. Ren, "Simple and accurate radio frequency inductance expression for on-chip planar spiral inductors", in ISAPE 2008 - The 8th International Symposium on Antennas, Propagation and EM Theory Proceedings, Kunming, China, 2–5 November, 2008, pp. 1025–1028, isbn: 9781424421923. doi: 10.1109/ISAPE.2008.4735396.

[2.77] B. J. Fletcher, S. Das, and T. Mak, “Design and optimization of inductive-coupling links for 3-D-ICs”, IEEE Transactions on Very Large Scale Integration (VLSI) Systems, vol. 27, no. 3, pp. 711–723, 2019, issn: 10638210. doi: 10.1109/TVLSI.2018.2881075.

[2.78] H. Tavakkoli, E. Abbaspour-Sani, A. Khalilzadegan, G. Rezazadeh, and A. Khoei, “Analytical study of mutual inductance of hexagonal and octagonal spiral planer coils”, Sensors and Actuators, A: Physical, vol. 247, pp. 53–64, 2016, issn: 09244247. doi: 10.1016/j.sna.2016.04.065. [Online]. Available: http://dx.doi.org/10.1016/j.sna.2016.04.065.

[2.79] X. Ding, X. Chen, N. Li, X. Chen, and X. Zhao, “An inductive salt solution concentration sensor using a planar coil based on a PQCR-L circuit”, Sensors and Actuators, A: Physical, vol. 263, pp. 246–251, 2017, issn: 09244247. doi: 10.1016/j.sna.2017.05.043. [Online]. Available: http://dx.doi.org/10.1016/j.sna.2017.05.043.

[2.80] F. Durmus and S. Karagol, “Mutual Inductance Calculation Formula for Planar Square Coils”, ISMSIT 2018 - 2nd International Symposium on Multidisciplinary Studies and Innovative Technologies, Proceedings, pp. 1–5, 2018. doi: 10.1109/ISMSIT.2018.8567040.

[2.81] M. Ulvr, “Design of PCB search coils for AC magnetic flux density measurement”, AIP Advances, vol. 8, no. 4, p. 047 505, Apr. 2018, issn: 2158-3226. doi: 10.1063/1.4991643. [Online]. Available: http://aip.scitation.org/doi/10.1063/1.4991643.

[2.82] F. J. Lopez-Alcolea, J. V. D. Real, P. Roncero-Sanchez, and A. P. Torres, “Modeling of a Magnetic Coupler Based on Single- And Double-Layered Rectangular Planar Coils with In-Plane Misalignment for Wireless Power Transfer”, IEEE Transactions on Power Electronics, vol. 35, no. 5, pp. 5102–5121, 2020, issn: 19410107. doi: 10.1109/TPEL.2019.2944194.

[2.83] Q. Wang, M. A. Saket, A. Troy, and M. Ordonez, “A Self-Compensated Planar Coil for Resonant Wireless Power Transfer Systems”, IEEE Transactions on Power Electronics, vol. 36, no. 1, pp. 674–682, 2021, issn: 19410107. doi: 10.1109/TPEL.2020.2998186.

[2.84] T. Leuerer and W. Mokwa, “Planar coils with magnetic layers for optimized energy transfer in telemetric systems”, Sensors and Actuators, A: Physical, vol. 116, no. 3, pp. 410–416, 2004, issn: 09244247. doi: 10.1016/j.sna.2004.05.020.

[2.85] H. Wang, J. Kow, N. Raske, G. de Boer, M. Ghajari, R. Hewson, A. Alazmani, and P. Culmer, “Robust and high-performance soft inductive tactile sensors based on the Eddy-current effect”, Sensors and Actuators, A: Physical, vol. 271, pp. 44–52, 2018, issn: 09244247. doi: 10.1016/j.sna.2017.12.060. [Online]. Available: http://dx.doi.org/10.1016/j.sna.2017.12.060.

[2.86] W. Li, S. Liao, and C. Tsou, “A novel sensing chip with dual-coil inductance for determining raw milk quality”, Sensors and Actuators, A: Physical, vol. 241, pp. 96–103, 2016, issn: 09244247. doi: 10.1016/j.sna.2016.01.035. [Online]. Available: http://dx.doi.org/10.1016/j.sna.2016.01.035.

[2.87] Y. Cheng and Y. Shu, “A New Analytical Calculation of the Mutual Inductance of the Coaxial Spiral Rectangular Coils”, IEEE Transactions on Magnetics, vol. 50, no. 4, 2014, issn: 00189464. doi: 10.1109/TMAG.2013.2290972.

[2.88] J. N. Snyder and F. C. Grover, Inductance Calculations Working Formulas and Tables, 85. 180 Varick Street New York, N. Y. 10014: Dover Publications, Inc., 1964, vol. 18, p. 164, isbn: 0876645570. doi: 10.2307/2003443.

[2.89] H. A. Wheeler, “Simple inductance formulas for radio coils”, Proceedings of the Institute of Radio Engineers, vol. 16, no. 10, pp. 1398–1400, 1928, issn: 07315996. doi: 10.1109/JRPROC.1928.221309.

[2.90] B. J. Fletcher, S. Das, and T. Mak, “A high-speed design methodology for inductive coupling links in 3D-ICs”, in Proceedings of the 2018 Design, Automation and Test in Europe Conference and Exhibition, DATE 2018, vol. 2018-Janua, Dresden, Germany, 19–23 March, 2018, pp. 497–502, isbn: 9783981926316. doi: 10.23919/DATE.2018.8342059.

[2.91] D. K. Biswas, M. Sinclair, T. Le, S. A. Pullano, A. S. Fiorillo, and I. Mahbub, “Modeling and characterization of scaling factor of flexible spiral coils for wirelessly powered wearable sensors”, Sensors (Switzerland), vol. 20, no. 8, 2020, issn: 14248220. doi: 10.3390/s20082282.

[2.92] L. C. Hsu, J. Kadomoto, S. Hasegawa, A. Kosuge, Y. Take, and T. Kuroda, “Analytical thruchip inductive coupling channel design optimization”, Proceedings of the Asia and South Pacific Design Automation Conference, ASP-DAC, vol. 25-28-Janu, pp. 731–736, 2016. doi: 10.1109/ASPDAC.2016.7428098.

[2.93] Y. R. K. N, “Dynamic Modeling and Calculation of Self and Mutual Inductance between a Pair of Coils for Wireless Power Transfer Applications using ANSYS Maxwell”, International Advanced Research Journal in Science, Engineering and Technology, vol. 2, no. 10, pp. 2393–2395, 2015. doi: 10.17148/IARJSET.2015.21002.

[2.94] H. Wakiwaka, D. Ito, K. Tashiro, H. Yajima, Y. Manta, T. Kanazawa, and N. Fujiwara, “Simplified calculation method of planar coil impedance considering the eddy current distribution by using finite element method”, Materials Science Forum, vol. 792, pp. 215–220, 2014, issn: 02555476. doi: 10.4028/www.scientific.net/MSF.792.215.

Chapter 3

Development of an Analytical Model for Self and Mutual Inductance of Planar Coils

In the process of developing a sensor, it is essential, during the design phase, to ensure that it meets the previously defined operational criteria. For this purpose, several design approaches need to be simulated, tested and compared. In the case of inductive sensors, several parameters can be adjusted from the geometry of printed planar coils, to the number of turns, space between turns, wire's width, internal and external diameter, and even the amount of coils used and their position.

Currently, as presented in the previous chapter, to evaluate the various possible combinations of coils to be used in a given application, in situations where the factor time is critical and precision is not a requirement, generic expressions limited to some geometries and configurations are used. When this does not happen, FEM simulations or experimental measurements can be employed, increasing substantially the designing costs. In both cases, the design time is drastically higher when compared to the use of more generic analytical expressions. This chapter presents the analytical model developed in this thesis, based on Grover equations, which accelerates the designing process of a sensor based on planar coils. With it, it is possible to control the various parameters of the coil (geometry, number of turns, wire's width, space between turns, number of segments per turn, amount of coils, and their position) and obtain its induction value for different configurations, without the need for high computational resources or spending a lot of time on this process.

The proposed model is presented in the Sections 3.1, 3.2 and 3.3. The first section is dedicated to the calculation of the self-inductance of 1-layer planar coils, the second section addresses the extension of the model to coils with two layers, and the third section integrates into the model the movement of a electrically conductive target over a planar coil. In each of these sections, the results obtained through

the implemented model is compared and validated with generic expressions, when applicable, and FEM simulations. In order to have a complete validation, Section 3.4 presents an experimental validation of these coil designs. Section 3.5 summarizes the conclusions reached regarding the developed model and the usual approaches.

3.1 Self-inductance Model for 1-Layer Planar Coils

3.1.1 1-Layer Model Implementation

In this section the model developed for single layer coils based on Grover equations [3.1] and the Expanded Grover Method [3.2] is described. This method considers that the inductance of a planar coil (Equation 2.2) is the result of the sum of all straight conductor's self-inductance, L_0, plus the mutual inductance between each segment pairs. Thus, the resulting mutual inductance, M_T, is the sum of all segment pairs of mutual inductance.

In order to calculate the self and mutual inductance of each coil segment, first it is necessary to have all the geometric information about the coil, as well as the lengths and geometrical coordinates of each segment. Considering the example of planar coils with 4, 6, 8, and 10 segments per turn, visible in Figure 3.1, it is perceptible that each trace has a length (l_i) and width (w), and that each turn is separated by a space s. In order to simplify the approach, for the inductance calculations the coil's wire width will be omitted. The wire will be referenced by a segment in its middle position and shortened at each connecting end by half the track's width, as represented by the dashed red line in the square coil of Figure 3.1 [3.2].

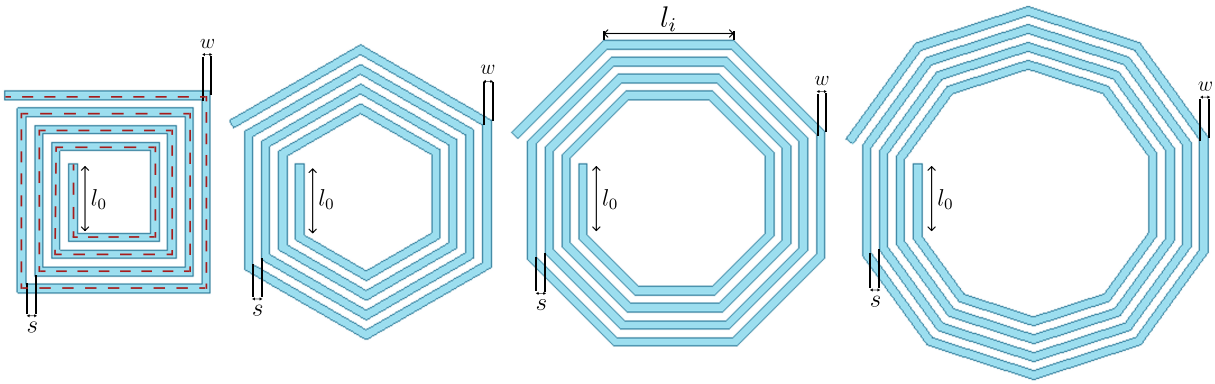

Figure 3.1: Planar coils of 4 turns with 4, 6, 8, and 10 segments per turn.

Thus, the first step is to calculate the coordinates of each vertex of the coil. As the model will be validated by a FEM model implemented using ANSYS®software, both of them should work on the same coil's layout. To draw the planar coil on ANSYS®, the python script available at [3.3] was used, where through the length

of the inner segment (l_0), the space between turns (s), the wire's width (w), the number of segments per turn (n_s), the total number of segments ($N \times n_s$) and the wire's thickness, the coil is generated. This way, part of this script was adapted and implemented using MATLAB®software, in order to have the coordinates of the simplified segments that represent the coil under analysis. With the coordinates determined, the calculation of the length of each of the coil segments (l_i) is done by calculating the distance between consecutive points.

As mentioned in Section 2.2.1, to calculate the coil's self-inductance it is necessary to calculate the self-inductance of each simplified segment (L_0), and the mutual inductance between all of them (M_T). To calculate L_0, Equation 3.1 has to be used for each coil's trace, being the l_i (cm) the length of the trace (calculated previously), w (cm) its width and t (cm) its thickness.

$$L_0 = \sum_{i=1}^{i=(N\times n_s)} L_{self_i} = \sum_{i=1}^{i=(N\times n_s)} 0.002 l_i (\ln(\frac{2l_i}{w+t}) + 0.50049 + \frac{w+t}{3l_i}) \tag{3.1}$$

After obtaining the self-inductance value of all the coil's segments it is necessary to calculate the mutual-inductance between them. Figures 3.2, 3.3, and 3.6 show the flowcharts that describe this process. To start the mutual-inductance calculation process (3.2) it is necessary to have previously defined the following variables:

- Nf: Number of coil turns
- n : Number of segments per turn
- coordinates [Nf.n, 2] : coil's vertices
- am_x [Nf, n] : x-coordinates of all segments in each turn
- am_y [Nf, n] : y-coordinates of all segments in each turn
- am_z [Nf, n] : z-coordinates of all segments in each turn length
- length [Nf,n] : segment's length
- teta [n,n] : angles between coil segments

Nf and **n** are both user-defined coil parameters at the beginning. The variable **coordinates** stores the values of the coil vertices calculated through the adapted script mentioned above, with the first column having the x-coordinates and the second having the y-coordinates. Both of them are assigned to the variables **am_x** and **am_y**, respectively. It is assumed that the coil is perpendicular to the z-axis, so all

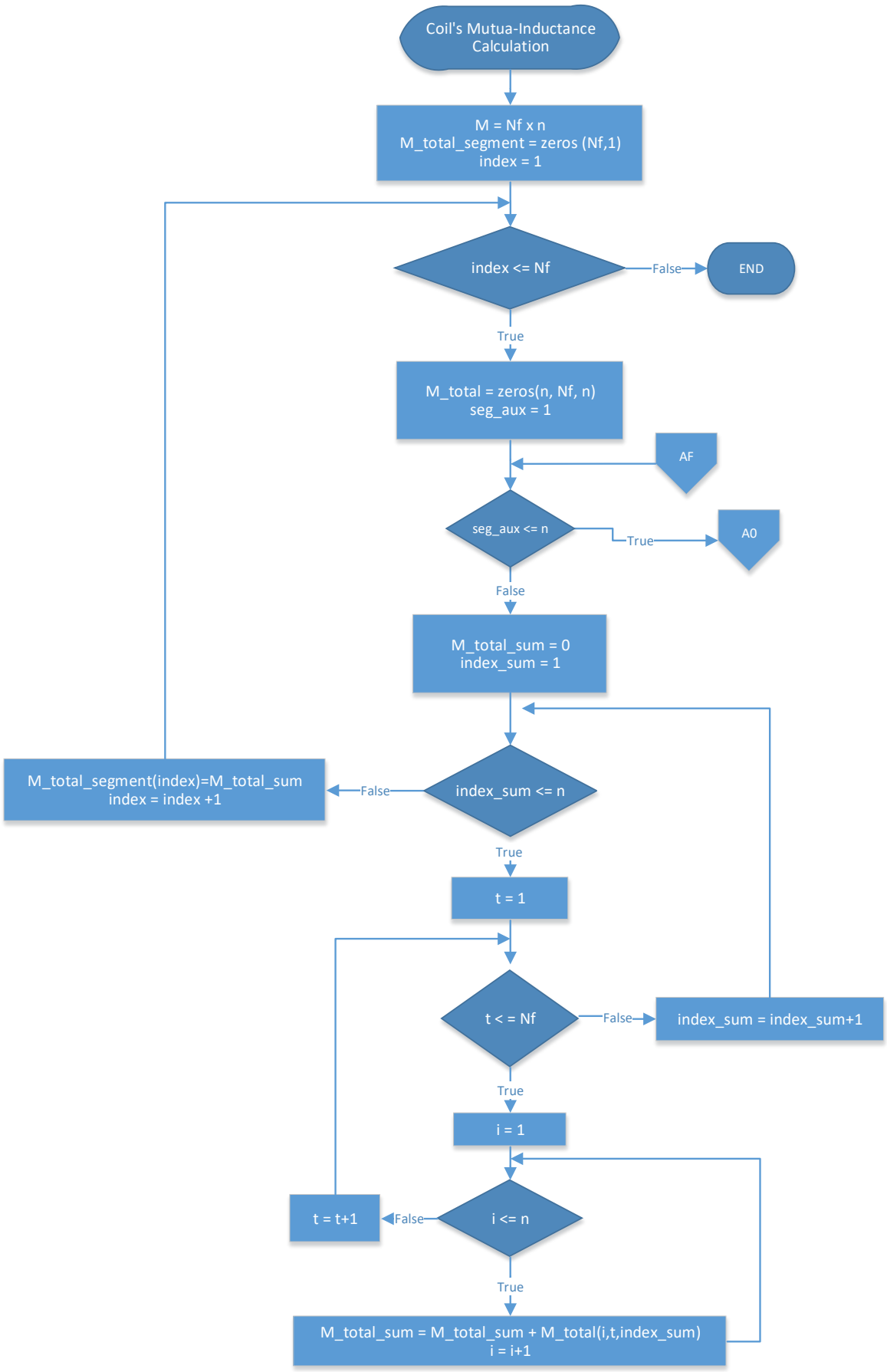

Figure 3.2: Flowchart of the mutual inductance calculation process PART 1.

the vertices of the coil have the same z-coordinates, and these values are in the variable **am_z**. The length of each of the coil segments (l_i), are stored in the variable **length**. The matrix lines of **am_x**, **am_y**, **am_z**, and **length** refer to the coil turns, and their columns to the coil vertices of each turn. Finely, the variable **teta** has the values of the angles between the segments of the coil, with each line referring to the angles between one segment and the others [3.4].

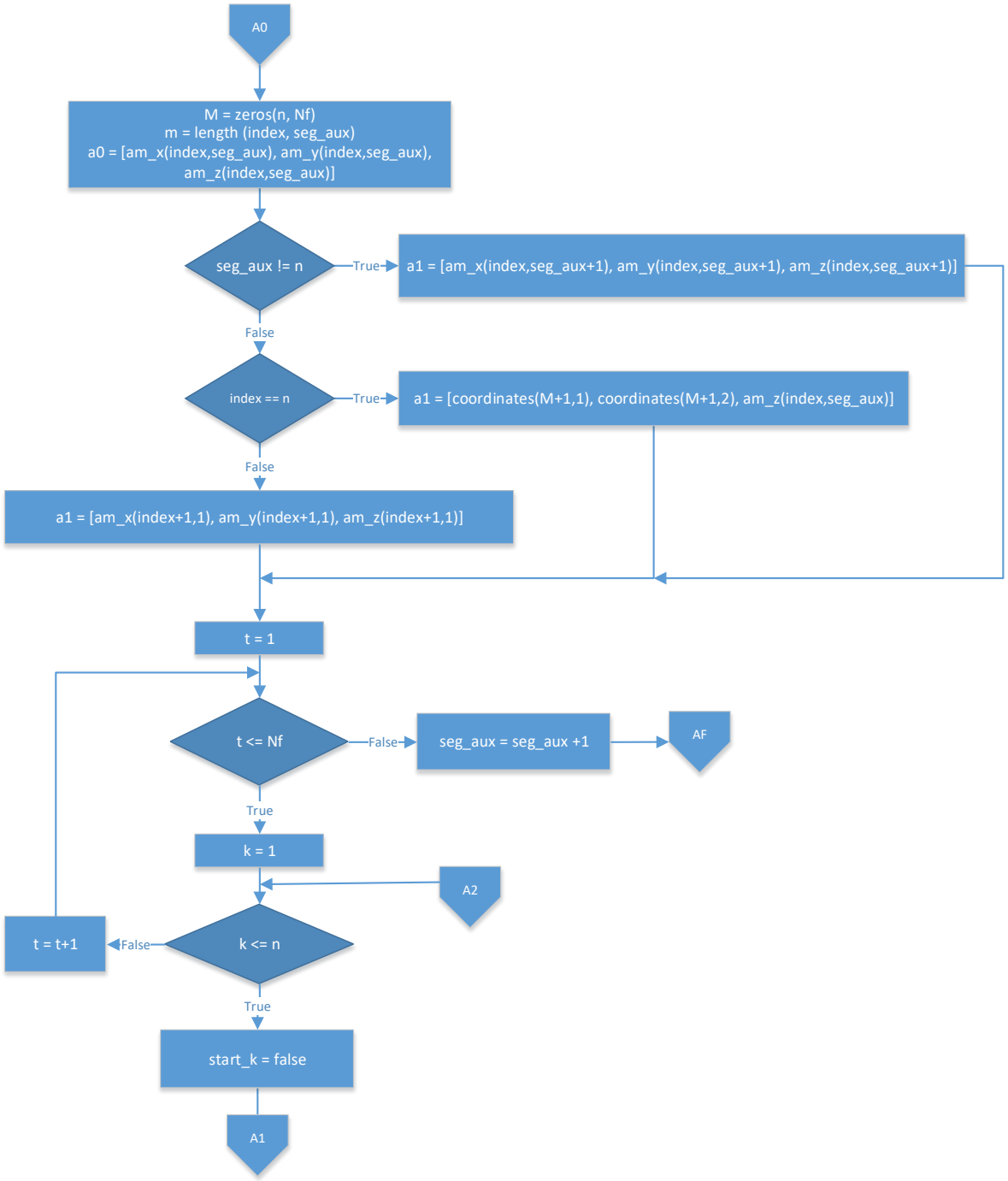

Figure 3.3: Flowchart of the mutual inductance calculation process PART 2.

Referring to the flowchart depicted in Figure 3.2, and bearing in mind the explanation made earlier about

the interaction that exists between segments of a coil, to calculate the mutual inductance among them, it is necessary to start by defining a segment as the reference, and then calculate the mutual inductance to all the other segments. In order to calculate the mutual inductances that exist between all segments, this process of defining the reference segment has to go through all the coil's segments. This way, the coordinates of the reference segment are denominated by a_0 and a_1. The coordinates of the segment that will be compared with the reference are denominated by b_k and b_{k+1}. These denominations are visible in Figures 3.3, 3.4 and 3.6. If the angle between the segments a_0a_1 and b_kb_{k+1} is 90 degrees, then the mutual inductance between them is automatically assigned with the value zero, otherwise, the function **Mutual_Inductance** is called. The input parameters of this function are the segments coordinates and its lengths, corresponding **m** to the length of segment a_0a_1, and **l** to the b_kb_{k+1} [3.4].

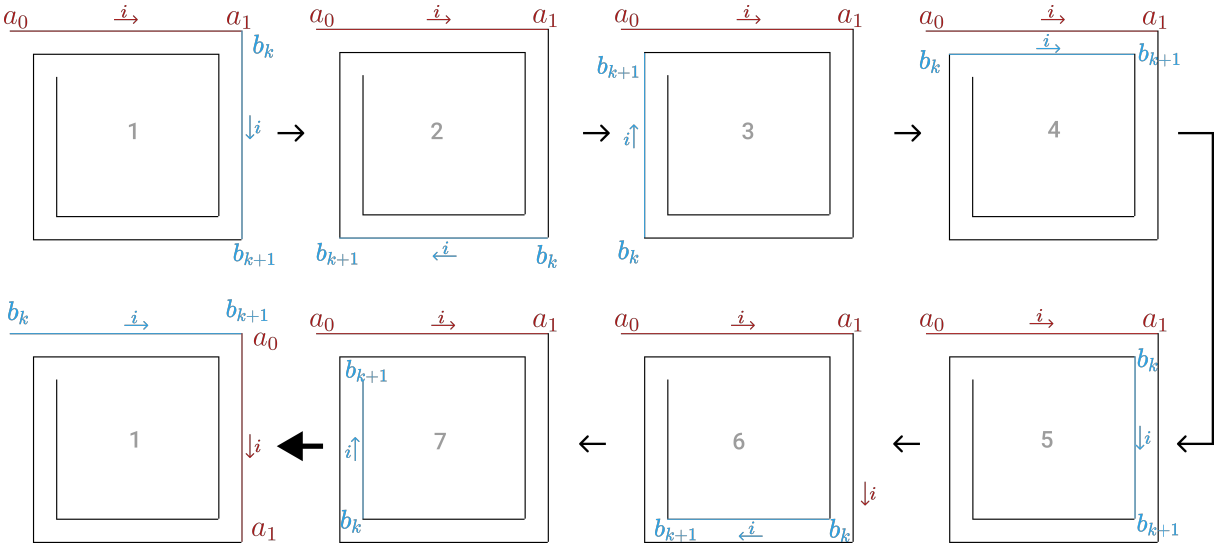

Figure 3.4: Sequence exemplifying the process of defining the reference segment (a_0a_1) and going through all segments (b_kb_{k+1}) of the coil to calculate the mutual inductances between them.

With regards to the function **Mutual_Inductance**, represented in the flowchart of Figure 3.7, it stands by verifying the direction of the current on each of the coil's segments. Since the Grover equations assume that the current in both segments has the same direction, the cross product between the segments vectors is done in order to check that. The results are stored in the variable **signal**, and if it is lower than zero, it means that the mutual-inductance between the segments is negative, and the orientation of the segment b_kb_{k+1} is swapped, passing b_k to stay with the value of b_{k+1} and vice versa. The variable **signal** will be used at the end of the calculation to restore the inductance signal. To calculate the mutual-inductance, Grover proposed two different approaches, one for parallel segments, and another to

unparalleled segments (see Equations 2.6 - 2.11). In Figure 3.5 it is possible to remind the geometric concepts of the different variables represented in the flowchart of Figure 3.7.

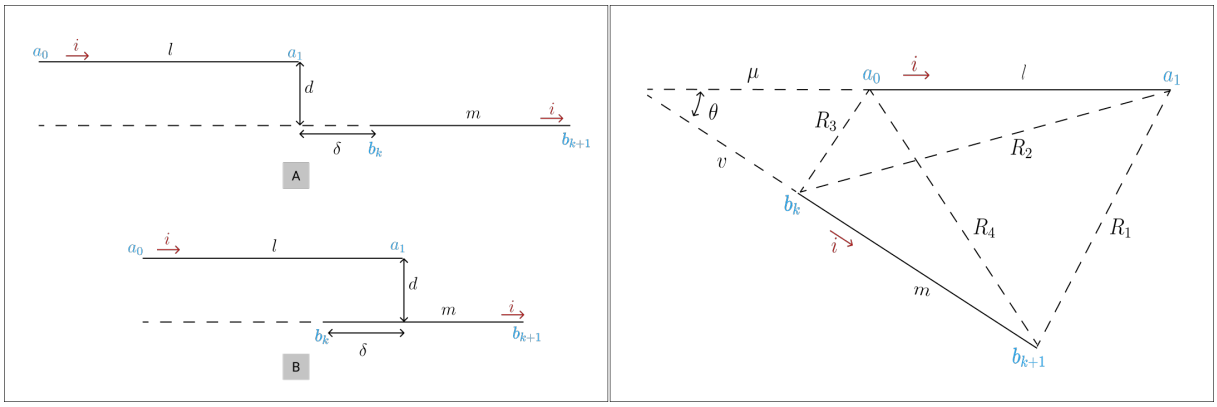

Figure 3.5: Mutual Inductance's general case of two filaments parallels, at left, and unparalleled at right.

Thus, according to the relationship between the geometry of the segments, the appropriate Grover equation is used, and the result is multiplied by the variable **signal**, ensuring that the inductance signal is calculated.

After calculating the mutual-inductance between all segments, the resulting values are summed up and added to the total self-inductance value, previously calculated. The final result corresponds to the auto-inductance value of the planar coil [3.4].

3.1.2 1-Layer Model Comparison with the Analytical Models Commonly used

In order to assess and validate the behaviour of the model developed, the auto-inductances calculated using it was compared with the values obtained by using the generic expressions previously presented (Chapter 2). Since the generic formulas are all valid just for square, hexagonal, and octagonal planar coils, these were the geometries selected to assess the proposed model. To analyze the behaviour of the model, coils with a different number of turns were tested, in order to understand if the model works for variable number of turns. To validate it, coils with 5, 10, and 15 turns were considered, with the different geometries previously indicated. As the validation is done by the comparison with the regular expressions, and since the Current Sheet Approximation formula's result presents larger errors with the increase of the ratio between the space between turns (s), and the width (w) of the inductor, the coils under analysis were considered to have equal width and space between coils turns. Taking into consideration the minimal values of w and s used in a regular PCB production, the values of 0.15 mm were selected.

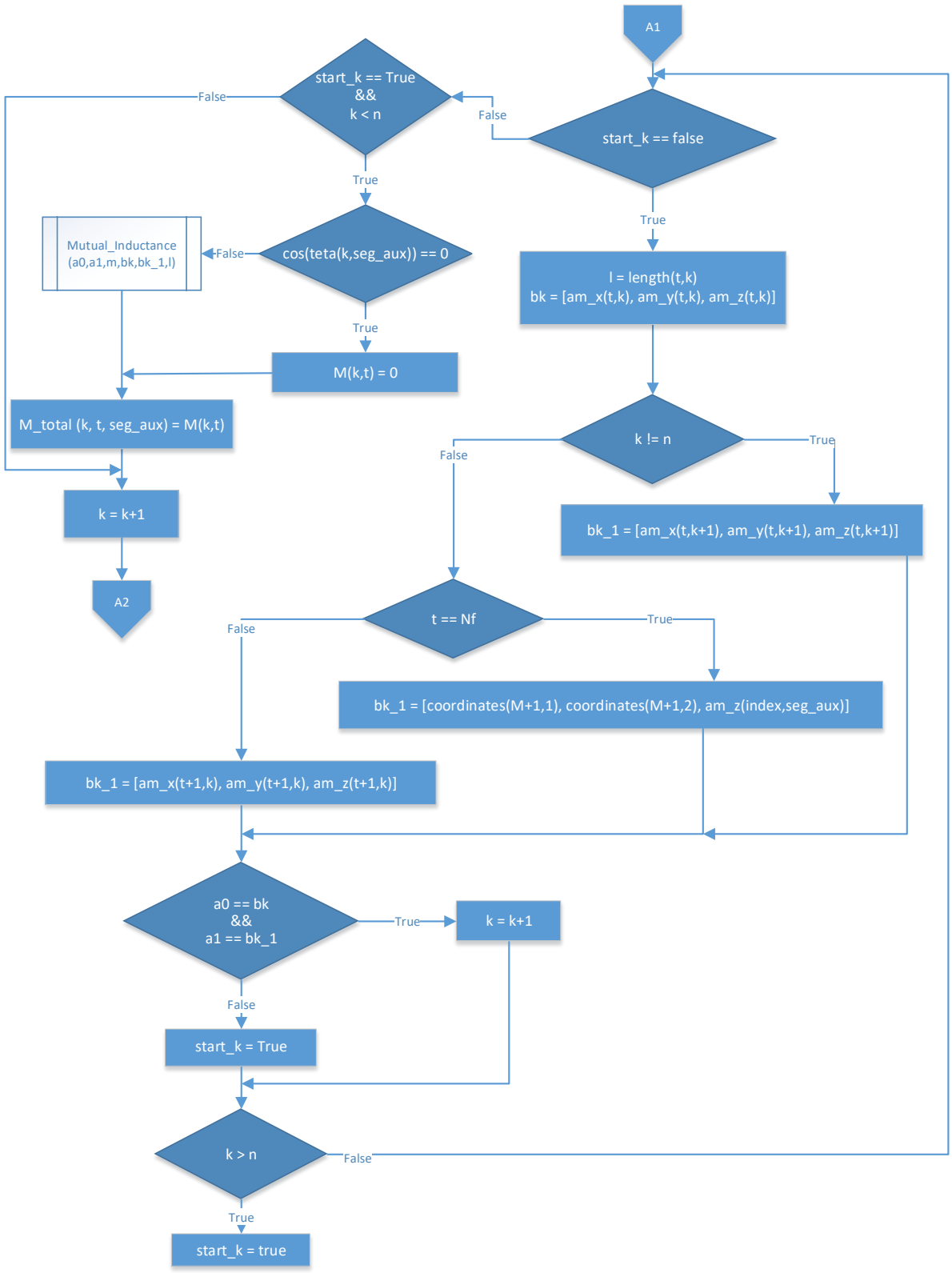

Figure 3.6: Flowchart of the mutual inductance calculation process PART 3.

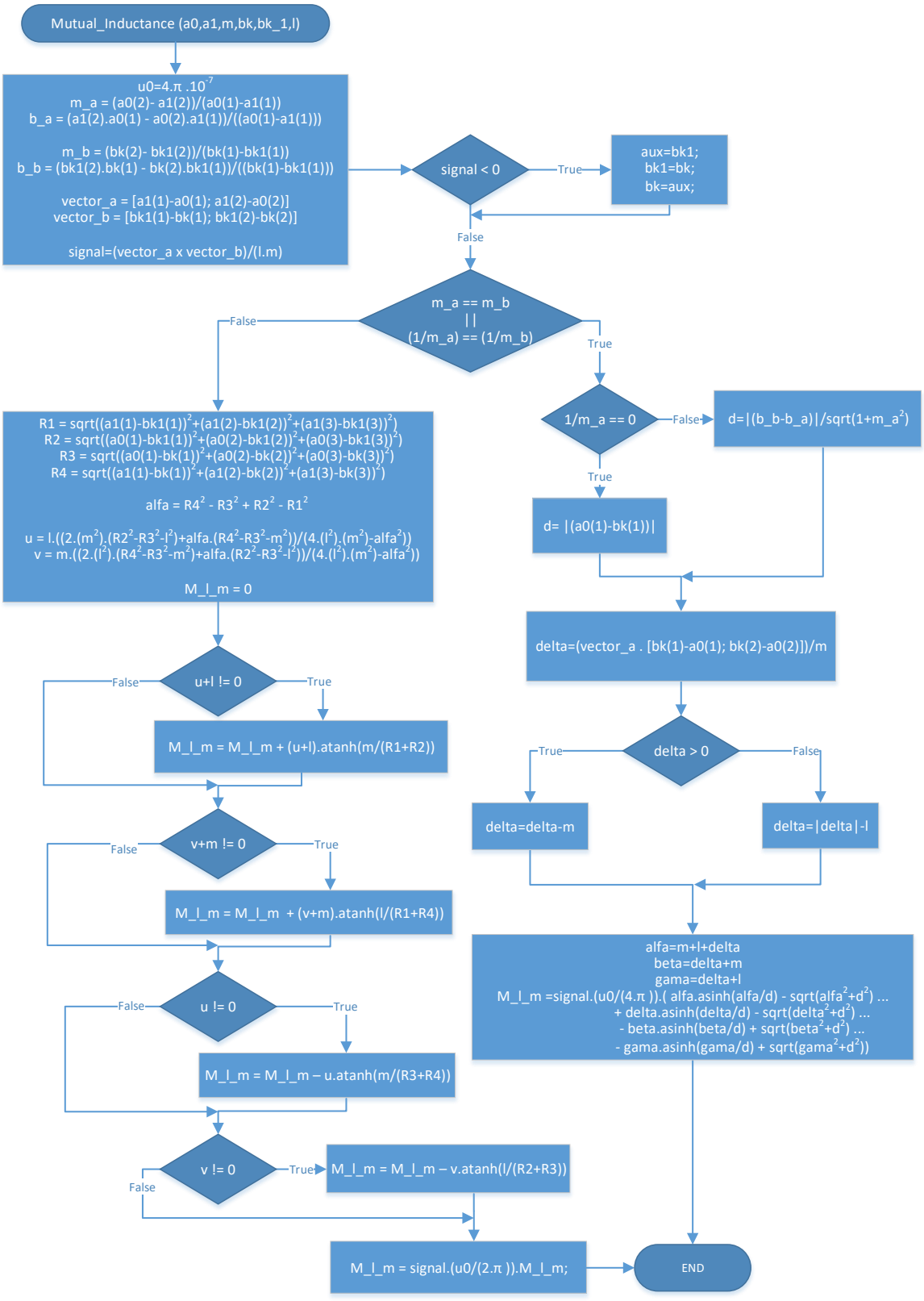

Figure 3.7: Flowchart of the Mutual Inductance Function.

The graphics in Figure 3.8 show the results for coils with 10 turns, considering the previously defined standard wire's width (w) and space between turns (s) of 0.15 mm. The inner segment, l_0, was changed in a range from 1 mm to 1.5 mm.

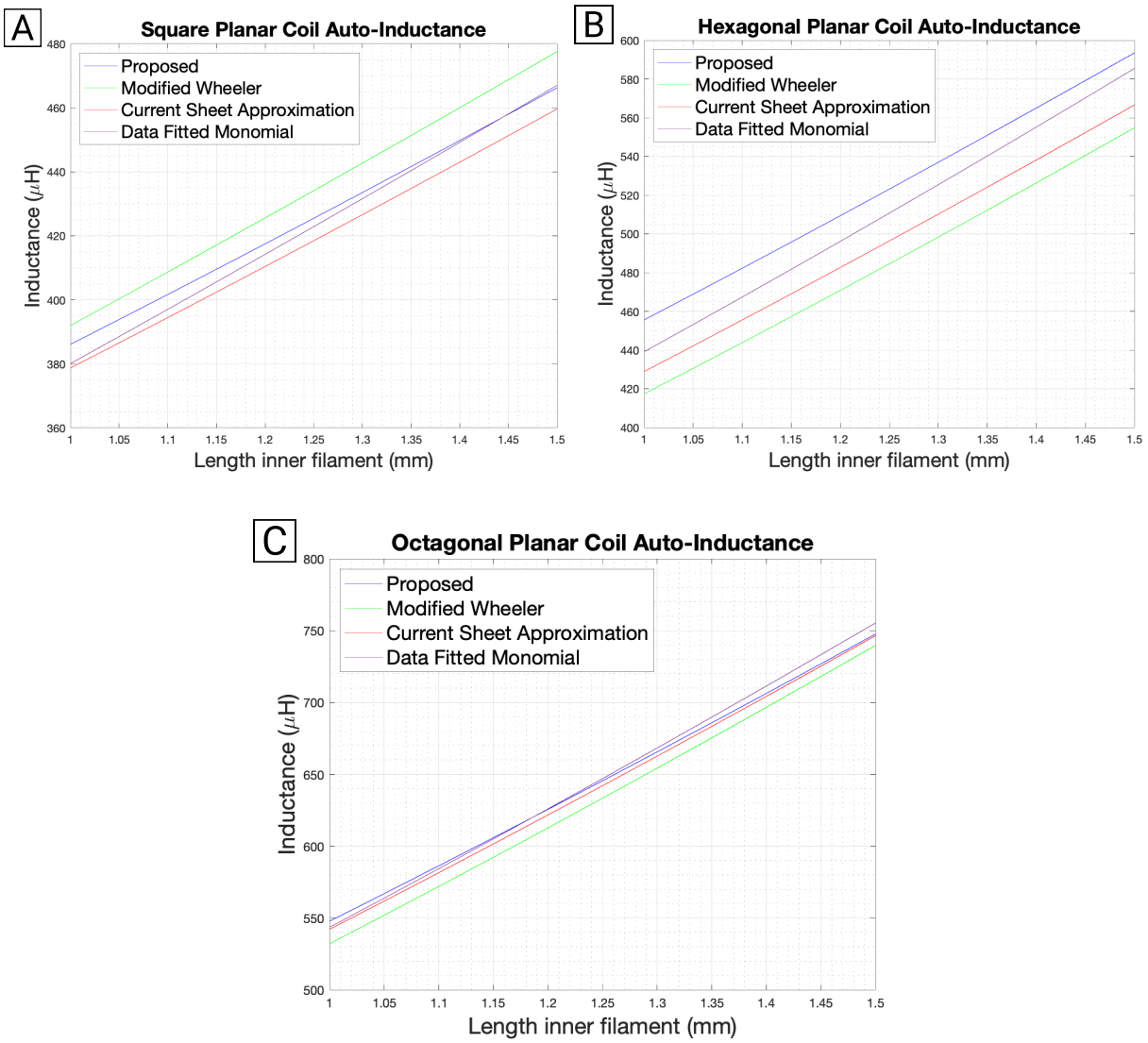

Figure 3.8: Inductance for coils of 10 turns, with a wire's width of 0.15 mm, and space between turns of 0.15 mm. A - Square coil; B - Hexagonal coil; C - Octagonal coil.

It is visible that the results from this thesis proposed analytical model are in concordance with the ones obtained from the generic expressions. For the case of the square coil, the maximum deviation from the proposed model and the generic expressions is approximately 2%. For hexagonal coils the values differ more, even between the generic formulas, being the maximum deviation equal to 8.39% when using the Modified Wheeler formula, 5.85% when using the Current Sheet Approximation expression, and 3.61% when using the Data Fitted Monomial. For the octagonal cases, the maximum error between

the model developed and the Current Sheet Approximation and the Data Fitted Monomial is around 1%, while between the Modified Wheeler formula is 2.87%.

To evaluate the model's response to a different number of coil turns, octagonal coils with 5, 10 and 15 turns were analysed, with a wire's width (w) of 0.15 mm, and space between turns (s) of 0.15 mm. The range of values for l_0 is the same from the previous simulation described. Analyzing the results obtained, depicted in Figures 3.8C and 3.9, it is perceptible that for all the turns simulated, the data from the proposed model is closer to the Current Sheet Approximation expression. The maximum deviation for $N = 5$, is 1.32%, for $N = 10$ is 1.03%, and for $N = 15$ is 1.89%. When using the Modified Wheeler formula, the maximum deviation for $N = 5$, and $N = 10$ is around 3% and for $N = 15$ is around 5%. When using the Data Fitted Monomial when $N = 5$ the maximum deviation is 5.04%, when $N = 10$ is 1.02%, and when $N = 15$ is 3.44%.

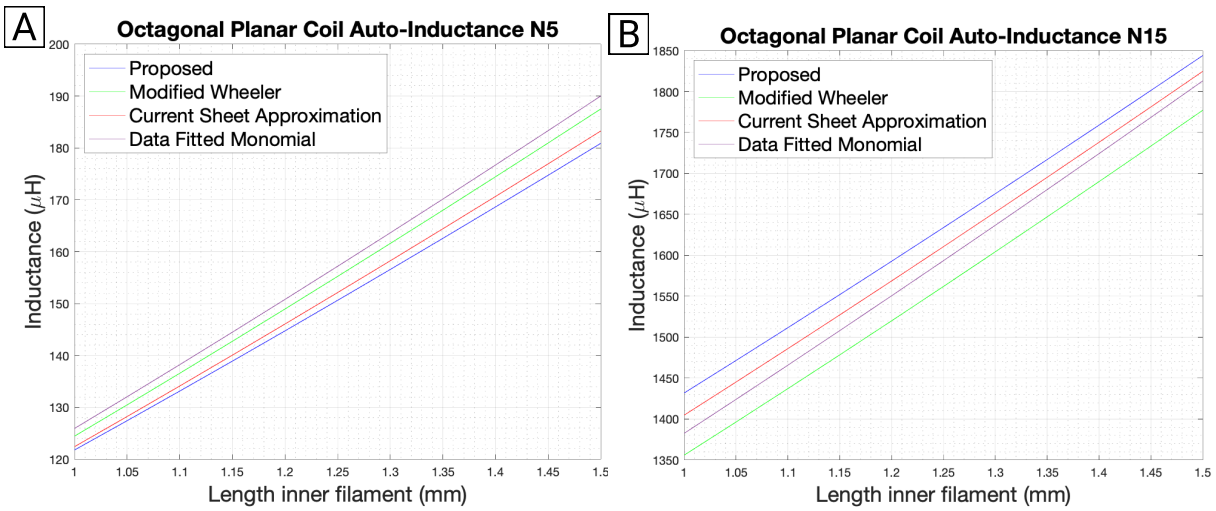

Figure 3.9: Inductance for Octagonal coils with a wire's width of 0.15mm, space between turns of 0.15mm, and A - 5 turns; B - 15 turns.

3.1.3 1-Layer Model Comparison with FEM Simulation

In this sub-section a comparison is performed between the coil's inductance values obtained with the developed model, with the analytical formulas, and the FEM simulations, which will be used as the reference values. This analysis will allow to verify which approach is the more accurate, the developed one or the generic formulas.

To design the coils on Ansys®Software, as already mentioned in sub-section 3.1.1, the python script available at [3.3] was used. Through the attribution of the length of the inner segment intended (l_0), the space

between turns (s), the wire's width (w), the number of segments per turn (n_s), the total number of segments ($N \times n_s$) and the wire's thickness the coil is generated. Figure 3.10$A-E$ shows the examples of coils layouts simulated with the different models, where analytical formulas were only applied to layouts 3.10$A-C$ [3.5].

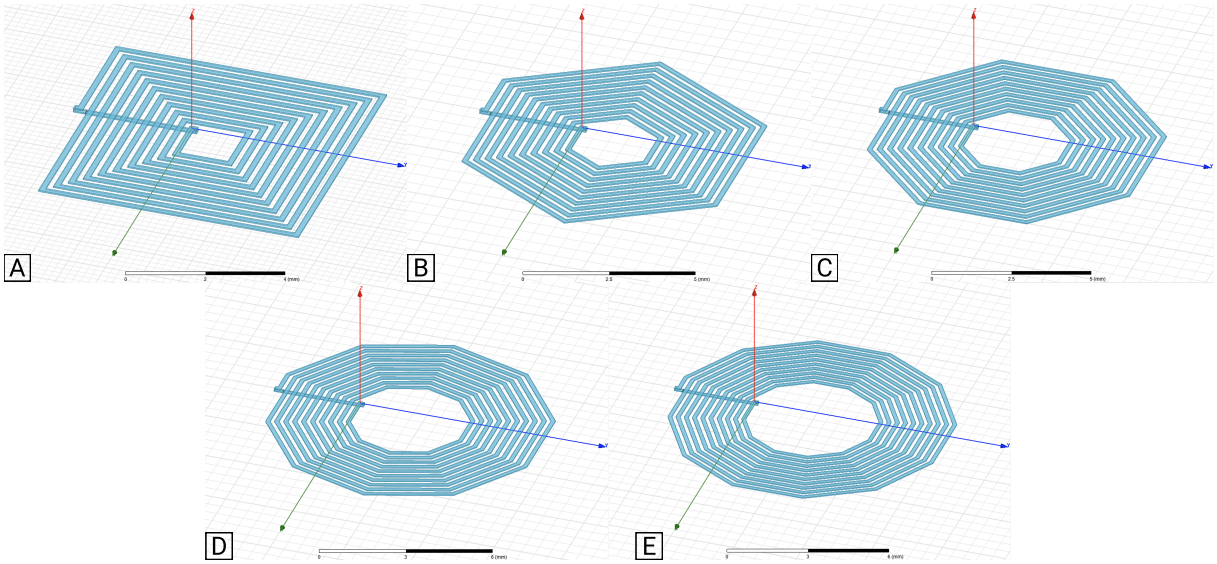

Figure 3.10: Coil's layouts simulated in Ansys®Software. Segments per turn: A: 4; B: 6; C: 8; D: 10; E: 12.

The finite element simulations were performed with Ansys®, selecting the solution type Magnetic, specifically the eddy current mode. The simulations consider an air-box with a side of five times the coil outer diameter, as shown in Figure 3.11A, for a square coil example, and a test current of 1mA. The solver frequency selected was 1 MHz, as it is close to the frequency of interest and corresponds to the maximum frequency that the laboratory's LCR [3.6], which will be used in the experimental results, can measure. The adaptive setup was configured with a percent error of 1% and a minimum of 2 convergence passes.

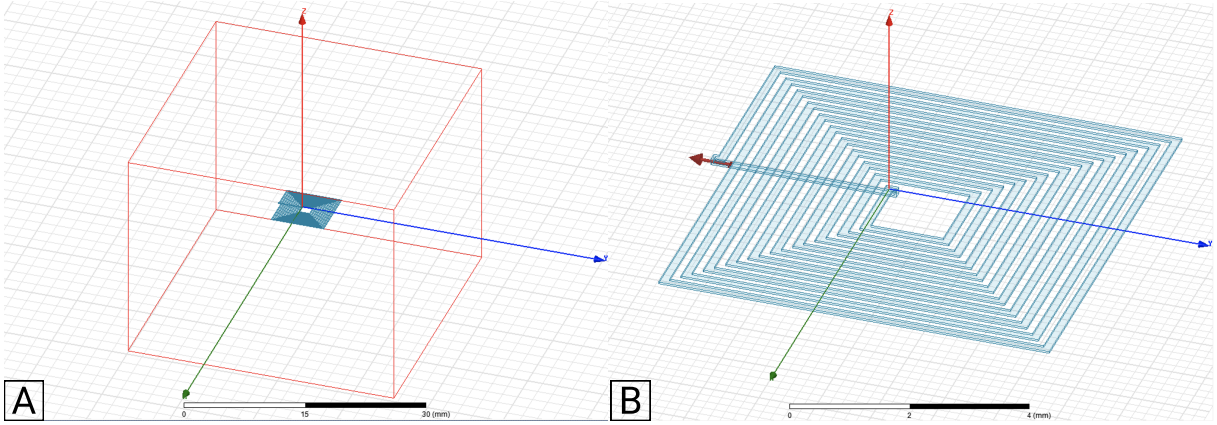

Figure 3.11: A: Ansys®project with coil and air box. B: Current applied into the coil.

Regarding the mesh parameters, the type selected for the simulation case of the coils with 1-layer was the surface approximation based, for both coil and air-box. In the coil it was assigned a finer mesh (level 9) (e.g. Figure 3.12B), since this is the critical area for the calculation of self-inductance, while for the air-box a coarser mesh (level 4) was used (e.g. Figure 3.12A) [3.5].

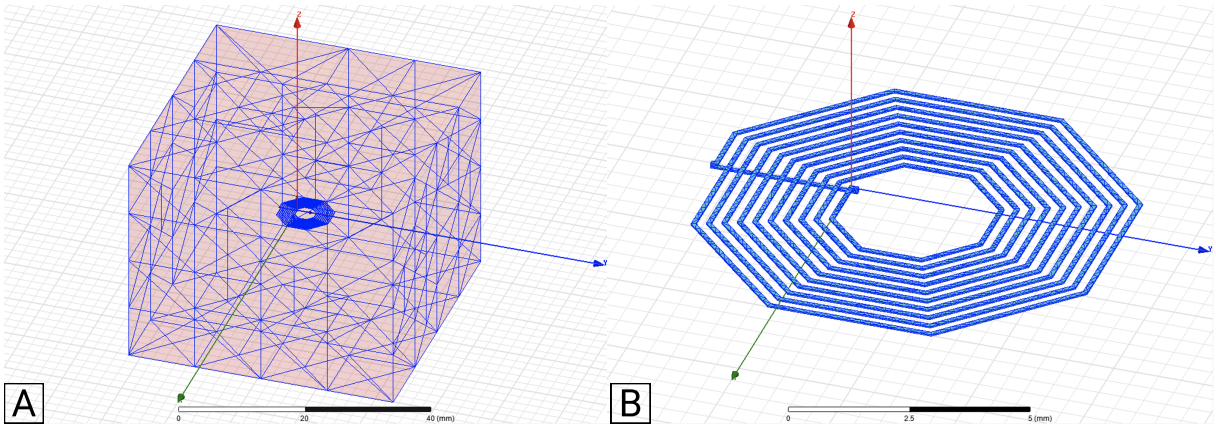

Figure 3.12: A: Air box's mesh. B: Coil's mesh.

Figure 3.13 and 3.14 present the self-inductance results for the different layouts (see Figure 3.10$A-E$) calculated with the different methods and software tool. There is a good agreement between the developed model with analytical formulas and FEM simulation results, reproducing the self-inductance trends observed as a function of the number of segments, and the number of turns. Considering the FEM simulation results as a reference, in the inductance values in Figure 3.13, the Modified Wheeler method shows a minimal error of 0.18% and a maximum of 35.85%. The Current Sheet Approximation method has a minimum error of 0.04% and a maximum of 6.31%, and the Data Fitted Monomial a minimum of 0.1% and a maximum of 3.51%. In the proposed model, the errors are between 0.58% and 2.64%. Particularly, for cases in which the state-of-the-art approximations have no solution, the developed model presents an error, in relation to the FEM model, between 0.62% and 0.82%.

From the results shown in Figure 3.14, the range of errors of the Modified Wheeler method is in between 0.99% and 12.67%, for the Current Sheet Approximation method between 2.93% and 9.39%, for the Data Fitted Monomial between 2.08% and 9.31%. For the developed model the errors are between 2.13% and 7.93%. Concerning the cases when just the proposed model has a solution, the errors are between 1.39% and 2.45%. Thus, it is possible to conclude that the errors of the proposed model are in concordance with the error range from the generic formulas, with the advantage of not being geometry limited.

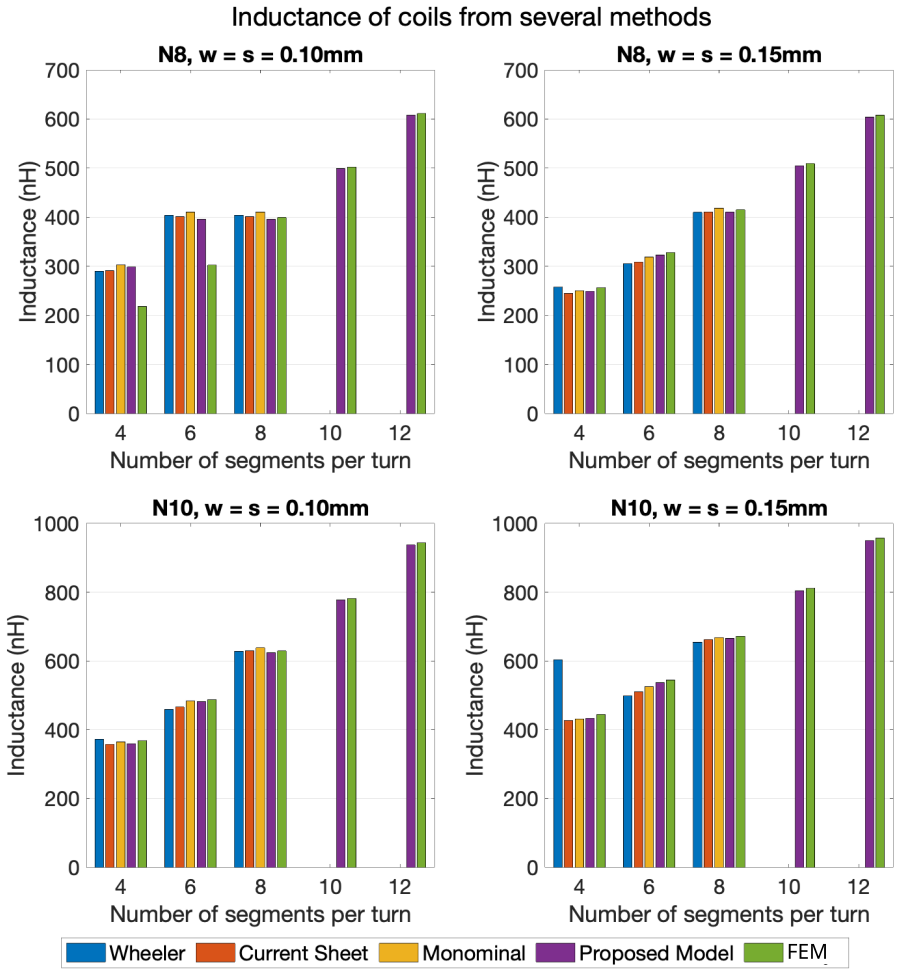

Figure 3.13: Comparison between several methods of inductance calculation of coils with 8 and 10 turns, for $L_0 = 1.3$mm, $w = s = 0.10$mm and $w = s = 0.15$mm, and for 4, 6, 8, 10, and 12 segments per turn.

3.2 Self-Inductance Model for 2-Layer Planar Coils

3.2.1 2-Layer Model Implementation

The process to calculate the self-inductance of a 2-layer planar coil follows the same line of reasoning for the case of a 1-layer coil. For the case of a 2-layer planar coil, in addition of having to calculate the auto-inductance of each of the coils, the mutual inductance between the two coils must also be calculated. However, in this mutual-inductance calculation process, instead of the compared segments being from the same coil, they will be from different coils. This way, taking into account the structure of the mutual-inductance calculation process presented in the flowcharts of Figures 3.2, 3.3, and 3.6, in the case of a 2-layer coil, there are some adjustments that must be done. In this case, two coils instead of one must be configured, having this way an upper and lower coil (each one with a n, s, w and L_0). Thus, with the self-inductance of each coil calculated, the calculation of the mutual-inductance between the two coils

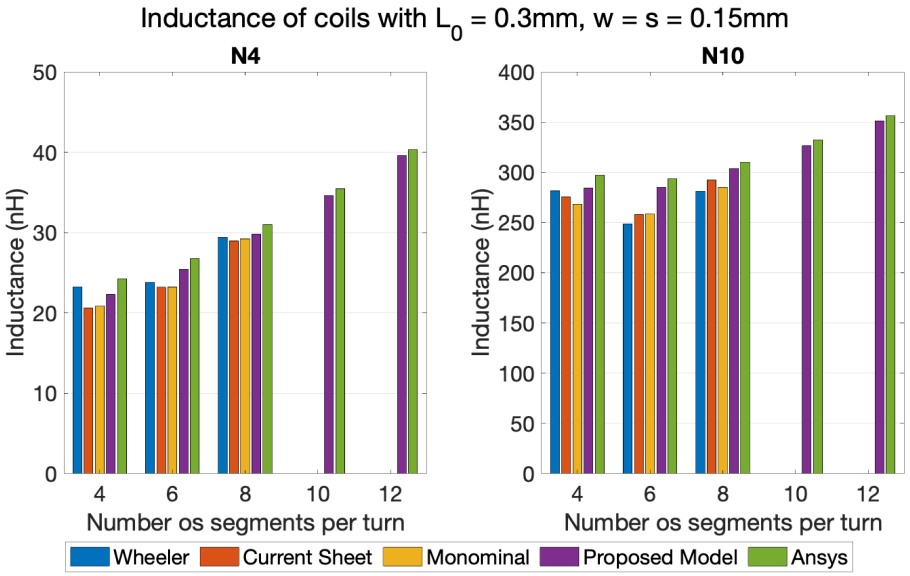

Figure 3.14: Comparison between several methods of inductance calculation of coils with 4 and 10 turns, for $L_0 = 0.3$mm, $w = s = 0.10$mm, and for 4, 6, 8, 10, and 12 segments per turn.

can be calculated. For the 1-layer case, the mutual-inductance calculation is always between segments, a_0a_1 and b_kb_{k+1}, that belong to the same coil and z-plane, being its different geometrical configurations represented in Figure 3.5. For the case of 2-layer coils, the segments a_0a_1 correspond to the upper coil segments, and the b_kb_{k+1} to the ones of the lower coil. These segments are in different z-planes, so the z component has to be considered in the mutual inductance calculation. Comparing Figures 3.15 with 3.5, it is possible to see the difference between the segments distances for the parallel and nonparallel cases, and how the variables fit.

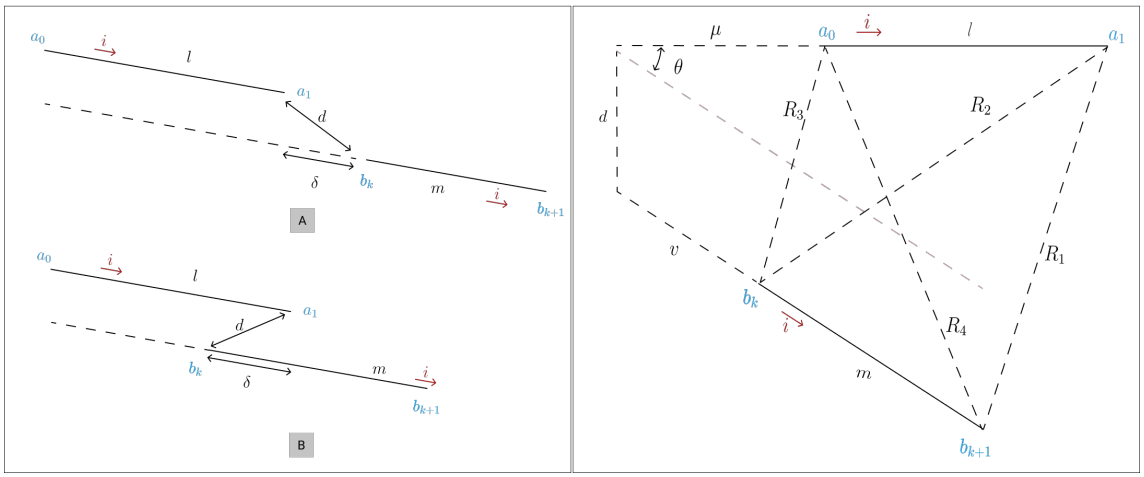

Figure 3.15: Mutual Inductance's general case of two filaments parallels in different z-planes, at left, and unparalleled at right.

With this new dimension, modifications were made to the equations used to calculate the mutual-inductance. According to [3.1], for the cases of nonparallel segments in different z-planes, the mutual-inductance between them is given by:

$$\begin{aligned} M = \frac{\mu_0}{2\times\pi}\cos\theta[(\mu+l)\tanh^{-1}\frac{m}{R_1+R_2} \\ +(v+m)\tanh^{-1}\frac{l}{R_1+R_4} - \mu\tanh^{-1}\frac{m}{R_3+R_4} \\ -v\tanh^{-1}\frac{l}{R_2+R_3} - \frac{\Omega d}{\sin\theta}] \end{aligned} \tag{3.2}$$

where,

$$\begin{aligned} \Omega = \arctan\frac{d^2\cos\theta+(\mu+l)(v+m)\sin\theta^2}{dR_1\sin\theta} - \arctan\frac{d^2\cos\theta+(\mu+l)v\sin\theta^2}{dR_2\sin\theta} \\ +\arctan\frac{d^2\cos\theta+\mu v\sin\theta^2}{dR_3\sin\theta} - \arctan\frac{d^2\cos\theta+\mu(v+m)\sin\theta^2}{dR_4\sin\theta} \end{aligned} \tag{3.3}$$

The remaining variables, (mu, v, m, l, d, θ, R_1, R_2, R_3, and R_4), are calculated in the same way as in the case of 1-layer coils (Equations 2.8, 2.9, 2.10, and 2.11). For the case of the parallel segments, the only difference that exists on the mutual-induction function is on the calculation of the variable d. Instead of being calculated by $d = |a0(1) - bk(1)|$ for the case of vertical segments, and by $d = |b_b - b_a|/\sqrt{1+m_a^2}$ for the other cases (described in Figure 3.7), it is calculated through $d = |(vector_a/m) \times [bk1(1) - a0(1); bk1(2) - a0(2); bk1(3) - a0(3)]|$.

Thus, with the self-inductance of the upper coil (L_{up}) and the lower coil (L_{down}), and the mutual inductance between them (M) calculated, follows the combination of them, through the equation $L_T = L_{up} + L_{down} \pm 2M$, already explained in Section 2.2.2.

3.2.2 2-Layer Model validation with FEM Simulation and comparison with a generic coupling coefficient

In this sub-section, the validation of the 2-layer proposed model is performed through the comparison of its results with the ones obtained through the FEM simulations, which are considered the reference values. The results obtained through the combination of the generic formulas and the approximated coupling coefficient formula are also compared. Figure 3.16 shows the examples of 2-layer coil layouts simulated with the different models (analytical formulas were only applied to layouts 3.10$A-C$).

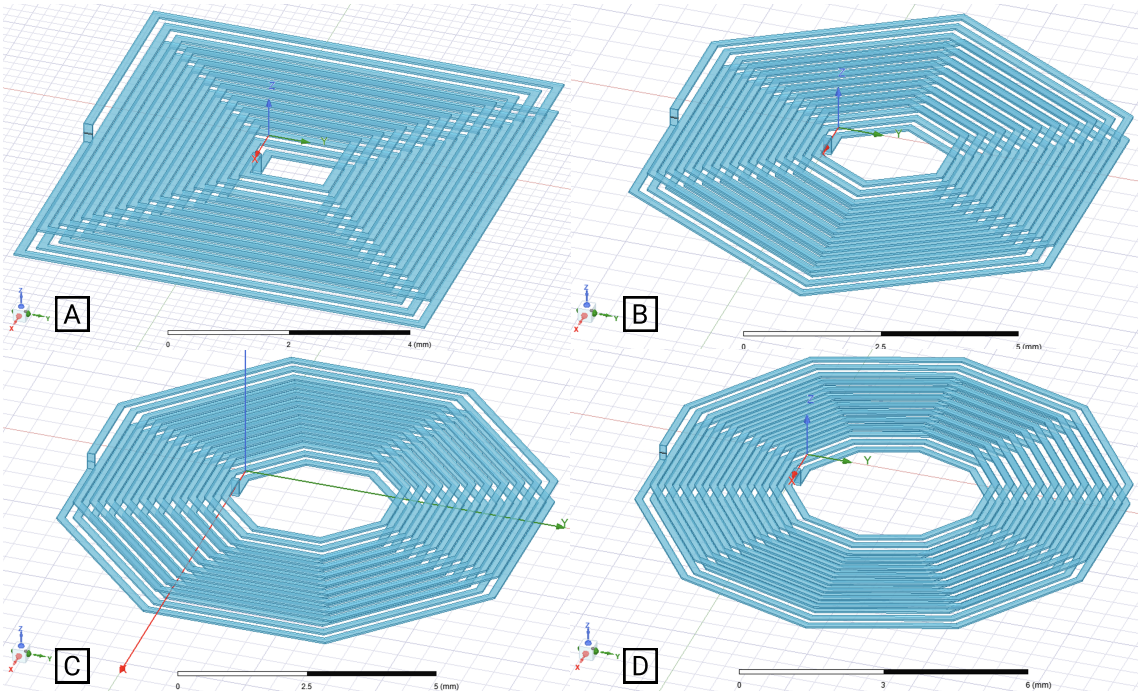

Figure 3.16: 2-layer coil layouts simulated in Ansys®Software. Segments per turn: A: 4; B: 6; C: 8; D: 10.

Each coil was drawn separately using the python script available at [3.3] (explained in Sub-section 3.1.1), by the attribution of the length of the inner segment intended (l_0), the space between turns (s), the wire's width (w), the number of segments per turn (n_s), the total number of segments ($N \times n_s$) and the wire's thickness. To ensure that the current flows in the same direction on both coils, the lower coil is mirrored in relation to the upper one. This way, if the current flows clockwise in the upper coil, the same will occur in the lower one.

The FEM simulations considered an air-box with the same side dimensions as before (five times the coil outer diameter), as depicted in Figure 3.17A, and a test current of 1 mA, visible in Figure 3.17B for a 2-layer square coil example. The solver frequency selected was 1 MHz, the adaptive setup was configured

with a percent error of 1%, and a minimum of 2 convergence passes. Regarding the mesh parameters, the type selected for the simulation case of the coils with 2-layer was the surface approximation based, for both coil and air-box. In the 2-layer coil it was assigned a finer mesh, since this is the critical area for the calculation of self-inductance, while for the air-box a coarser mesh was used.

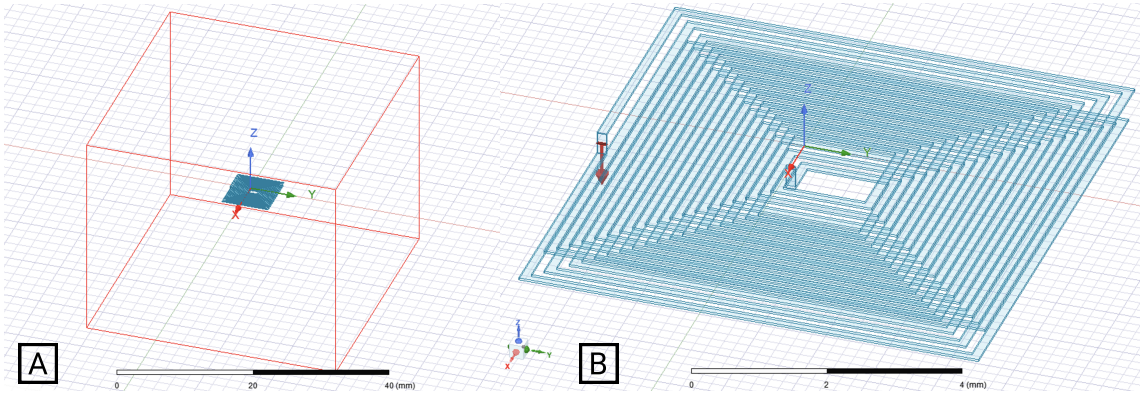

Figure 3.17: A: Ansys® project with 2-layer coil and air box. B: Current applied into the coil.

The simulations performed with 1-layer coils, presented in Sub-section 3.1.3, show the concordance that exists between the FEM model, the developed analytical model and the generic expressions. The same does not happen in the case of a 2-layer coil. Looking into Figures 3.18 and 3.19 it is visible that the developed model is much more in concordance with the FEM model than the generic expressions. The inductance values from the generic expressions for the case of 2-layer coils present significant errors. It is visible that all the generic expressions have the same pattern, which is very different from the one got from the FEM simulations and the proposed model. This highlights the limitation of the generic coupling factor in the calculation of the inductance of a 2-layer coil.

The coupling factor expression is limited to the conditions under it was generated. Thus, it claims to be work through multi-layer coils with the distance between adjacent layers varying from 0.75 mm to 2 mm, with coils with 5 to 20 turns. Having this in consideration, it was already expected that the inductance values from the generic expressions for the case of 2-layer coils with 4 turns would present significant errors (Figure 3.18).

However, for the case of 2-layer coils with 10 turns the inductance values calculated were expected to have a good concordance. Through, the analysis of the graphics presented in Figure 3.19 it can be seen that the results are closer to the ones got from FEM than for the case of 2-layer coils with 4 turns. Considering, the case of the 10-turn coils, for the distance between layers from 0.75 mm to 2 mm (values

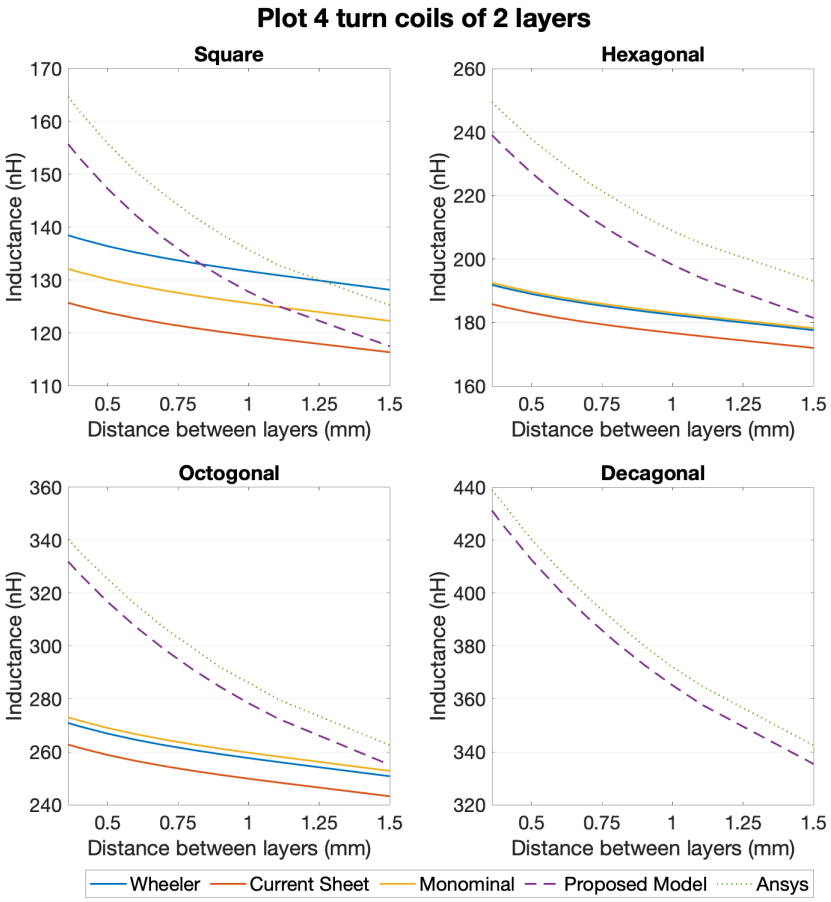

Figure 3.18: Comparison between several methods of inductance calculation of 2-layer coils with 4 turns, for $L_0 = 1.3$mm, $w = s = 0.15$mm, and for 4, 6, 8, and 10 segments per turn.

that the generic coupling coefficient is valid), the maximum error registered between the FEM model and the generic approaches is 4.42% for the square coils, 10.83% for the hexagonal case, and 6.57% for the octagonal. For the same selected cases, the proposed approach shows maximum errors of 3.53% for the square coils, 2.22% for the hexagonal, 1.56% for the octagonal, and 1.23% for the decagonal.

In view of the results, it can be concluded that within the ranges in which the coupling coefficient formula was generated, the results are significantly better. However, despite this improvement, the values obtained by the developed model are much more in agreement with the FEM model results in all the cases tested. Therefore, taking into account the limitations of the expression of the coupling factor and for the generic expressions, with respect to the geometries of the coils, and of the errors in relation to the FEM simulations, it can be concluded that the approach developed is more efficient and versatile.

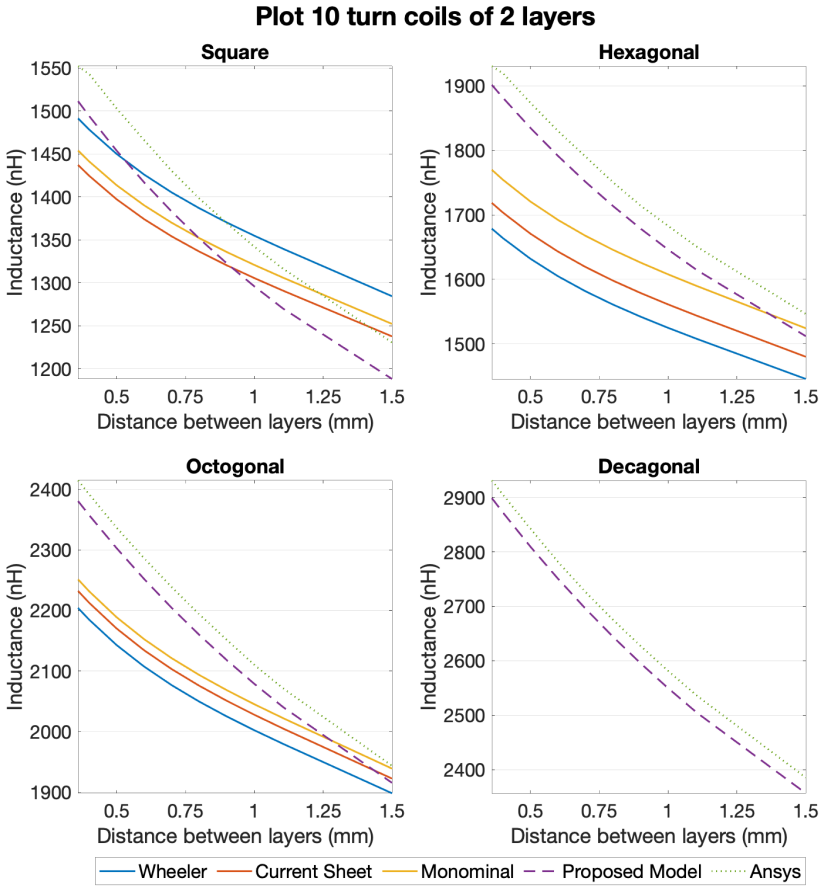

Figure 3.19: Comparison between several methods of inductance calculation of 2-layer coils with 10 turns, for $L_0 = 1.3$mm, $w = s = 0.15$mm, and for 4, 6, 8, and 10 segments per turn.

Considering the structure of the model developed, it is easily scalable to planar coils with more layers. However, as coils printed in PCB with more than two layers were not required by the laboratory, this aspect was not explored in depth.

3.3 Inductance Model for 1-Layer Planar Coil with a Conductive Target

3.3.1 1-Layer Coil with a Conductive Target Model Implementation

As explained in Sub-section 2.1.5, when a conducting plate is close to a coil and intercepts its magnetic field, the inductance of the coil changes. To calculate the inductance of a 1-layer planar coil with a conductive target, the same line of reasoning used for the case of the 2-layer coil, presented in the previous section, was employed. According to Hiroyuki Wakiwaka et al [3.7] and Norhisam Misron et al [3.8], when

a conductive target is placed over or under a planar coil, the eddy currents induced in it practically only take place in the overlapped area. That is, the target area that does not overlap the coil does not have a significant amount of eddy currents and can therefore be ignored. This way, even if the target is larger than the coil, only the overlapping area is considered. Hiroyuki Wakiwaka et al [3.7] also states that the target can be approximated to a one-turn coil, with a track width equivalent to the space between the inner and outer edges of the coil. Figure 3.20 shows an example of a hexagonal coil with 4 turns and in shaded blue the shape of the target that is considered by the analytical model. It is noticeable that the outer and inner sides of the coil are responsible for defining the shape and width of the one-turn coil that is used to represent the target.

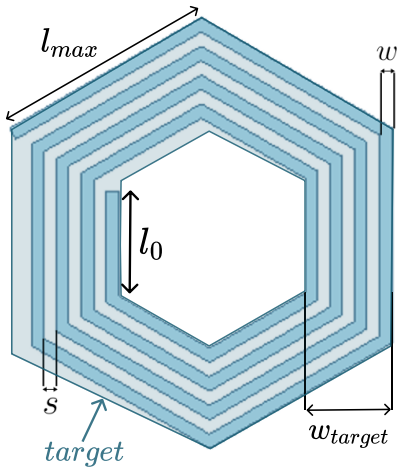

Figure 3.20: Hexagonal coil and the corresponding target geometry which is considered in the analytical model to calculate the inductance between them.

For the calculations of the self-inductance of the target and the mutual inductance between the target and the coil, the average filament of the one-turn coil has to be used. This filament corresponds to the medium position between the inner and outer edges of the coil, as marked in green dashed lines in Figure 3.21.

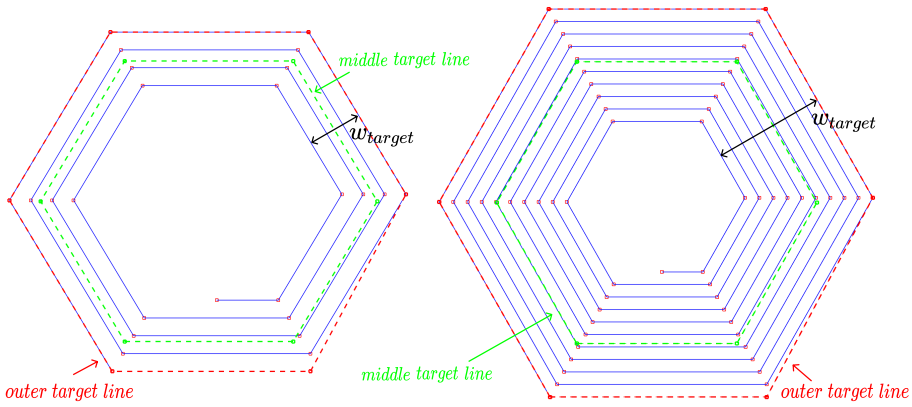

Figure 3.21: Two sets of coil and target as used by the analytical model are represented. In blue two hexagonal coils, with 4 and 10 turns, and in green the one-turn coil representing the target.

The figure shows two examples of how the analytical model considers a hexagonal coil and its target in the inductance calculations, for 4 and 10 turns. In blue are represented the filaments of the hexagonal coils and in green are those of the coil that represents the target. In order to obtain the target dimensions, as the coils have regular geometries, the radius of the circle containing the outermost filament of the coil was calculated. Later, this radius was used to calculate the length of the sides of the target, being then possible to calculate the coordinates of each of the target vertices. In this way, the target parameterization for the position in which it is completely over the coil can be obtained. However, if it is only partially overlapping the coil, it is necessary to intersect its areas in order to obtain the overlapping area. Figure 3.22 exemplifies the translation of a target over an octagonal coil and how this movement is reflected in the target's geometry. The resulting geometry is the one that will be considered later in the calculations of the mutual inductance between the target and the coil.

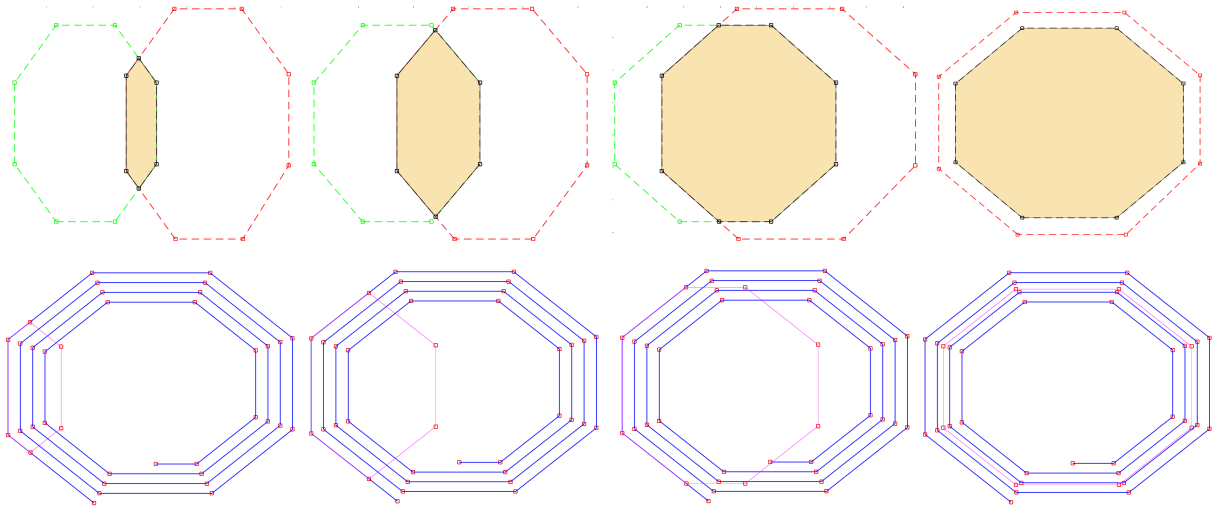

Figure 3.22: Target moving and the resulting geometry.

With the target geometry defined, the calculation of the inductance of the coil overlapped by a target can be obtained. Due to the target's approximation to a one-turn coil, its self-inductance and mutual inductance with the coil are calculated using the calculation functions used in the case of the 2-layer planar coil. However, the total inductance of the system can not be calculated in the same way, since the current in the target is not the same that flows in the coil. Therefore, to calculate the total inductance of the coil, first the self-inductances of the 1-layer coil (L_{Coil}) and of the target (one-turn coil)(L_{Target}), and the mutual inductance between both ($M_{Coil+Target}$) need to be calculated.

$$L_{Total} = L_{Coil} - \frac{M^2_{Coil+Target}}{L_{Target}} \tag{3.4}$$

3.3.2 1-Layer Coil with a Conductive Target Model validation with FEM Simulation

In this sub-section, the validation of the 1-layer coil with a target model is performed through the comparison of the results obtained and the results given by the FEM simulations, which are considered the values of reference.

For the model validation, 1-layer coils with 4, 6, 8 and 10 sides per turn were simulated, as shown in Figure 3.10$A-D$, for 4 and 10 turns, with a wire's width and a space between turns of 0.15 mm, in the presence of a target over it (example in Figure 3.23).

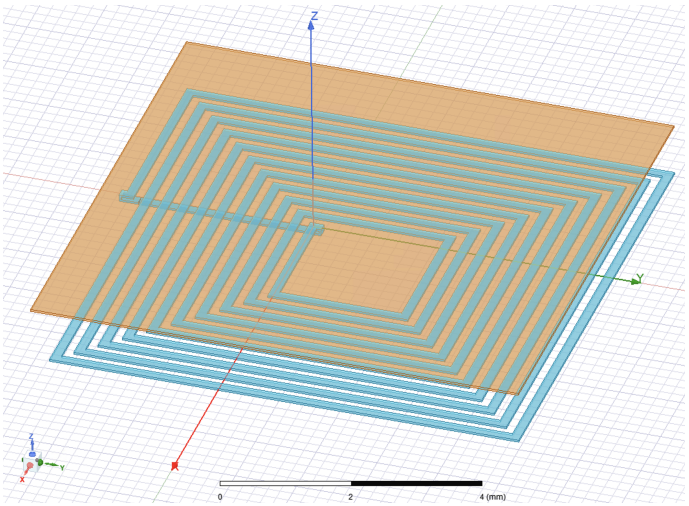

Figure 3.23: FEM model of a square coil with a target over it.

The FEM models simulated followed the same configuration as the ones used in the validation of the previous models. This way, the simulations considered an air-box with a side of five times the border of the objects, and a test current of 1 mA. The solver frequency selected was 1 MHz, the adaptive setup was configured with a percent error of 1%, and a minimum of 2 convergence passes. Regarding the mesh parameters, the type selected for this simulation case was the surface approximation based, for coil, target and air-box. In the coil and target it was assigned a finer mesh, since these are the critical area for the calculation of self-inductance, while for the air-box a coarser mesh was used.

In order to understand how the proposed analytical model responds to different target positions in different coil's geometries, for each one of the coil's geometries (Figure 3.10$A-D$), the target was simulated in several positions, either on the z-axis and on the y-axis. Thus, Table 3.1 summarizes the used values for each variable.

Table 3.1: Simulation cases with 1-layer coil and target

Variables	**Values**
Coil layout	Square, Hexagonal, Octagonal, Decagonal
Number of coil turns	4, 10
Inner coil segment (l_0)	0.3, 1.0, 1.5, 2.0
Target height(z_{target})	0.36, 0.4, 0.5, 0.7, 0.8, 1.0, 1.105, 1.5
Target translation (y_{target})	$-\lambda$, $-\frac{3\lambda}{4}$, $-\frac{\lambda}{2}$, $-\frac{\lambda}{4}$, 0, $\frac{\lambda}{4}$, $\frac{\lambda}{2}$, $\frac{3\lambda}{4}$, λ^*

* Where λ corresponds to the coil length on the y axis.

When comparing the values obtained from the various FEM simulations with those of the developed model, it was concluded that in order to improve the target approximation model, it is necessary to add a compensation factor. After several simulations with coils of different sizes and geometries, the most suitable value for the compensation factor is 0.3. Thus, this compensation factor was added to equation 3.4:

$$L_{Total} = L_{Coil} - \frac{M^2_{Coil+Target}}{L_{Target}} \times 1.3 \tag{3.5}$$

To better understand the differences between the results obtained in the FEM simulations and the proposed model with and without the compensation factor, the comparison of these three methods, for all case studies visible in Table 3.1, was performed. Figures 3.24 and 3.25 show some of the results obtained by the methods under analysis for all the configurations of l_0 and y_{target} presented in Table 3.1, and for some of the values of z_{target}, namely 0.4 mm, 0.7 mm, 1.0 mm, and 1.5 mm. In the case of Figure 3.24, the inductance values refer to the translation of the target on a square coil of 4 turns, and of Figure 3.25 to a 10-turn octagonal coil. Analyzing the graphics from both figures, it is noticeable that, in general, the model developed with the correction factor presents results closer to those obtained by FEM simulations.

To validate the developed model and quantify the errors obtained with the compensation factor, in relation to the FEM model, an error analysis along the translation movement of the target over the coil was performed. Appendix A shows the inductance graphs obtained for all the case studies defined in Table 3.1. Through its analysis, it can be concluded that the developed model presents a worse performance for distances between the target and the coil of less than 0.7 mm. Table 3.2 summarizes the two ranges of average error over a target translation for the several coil's configurations, where **F** regards to the full simulated range of z_{target} and the **S** to the selected range of z_{target} higher or equal to 0.7 mm. Through the analysis of this table, it is possible to verify that with the increase in the number of turns and the size of the internal hole radius of the coil, the errors between FEM simulation and the proposed model also

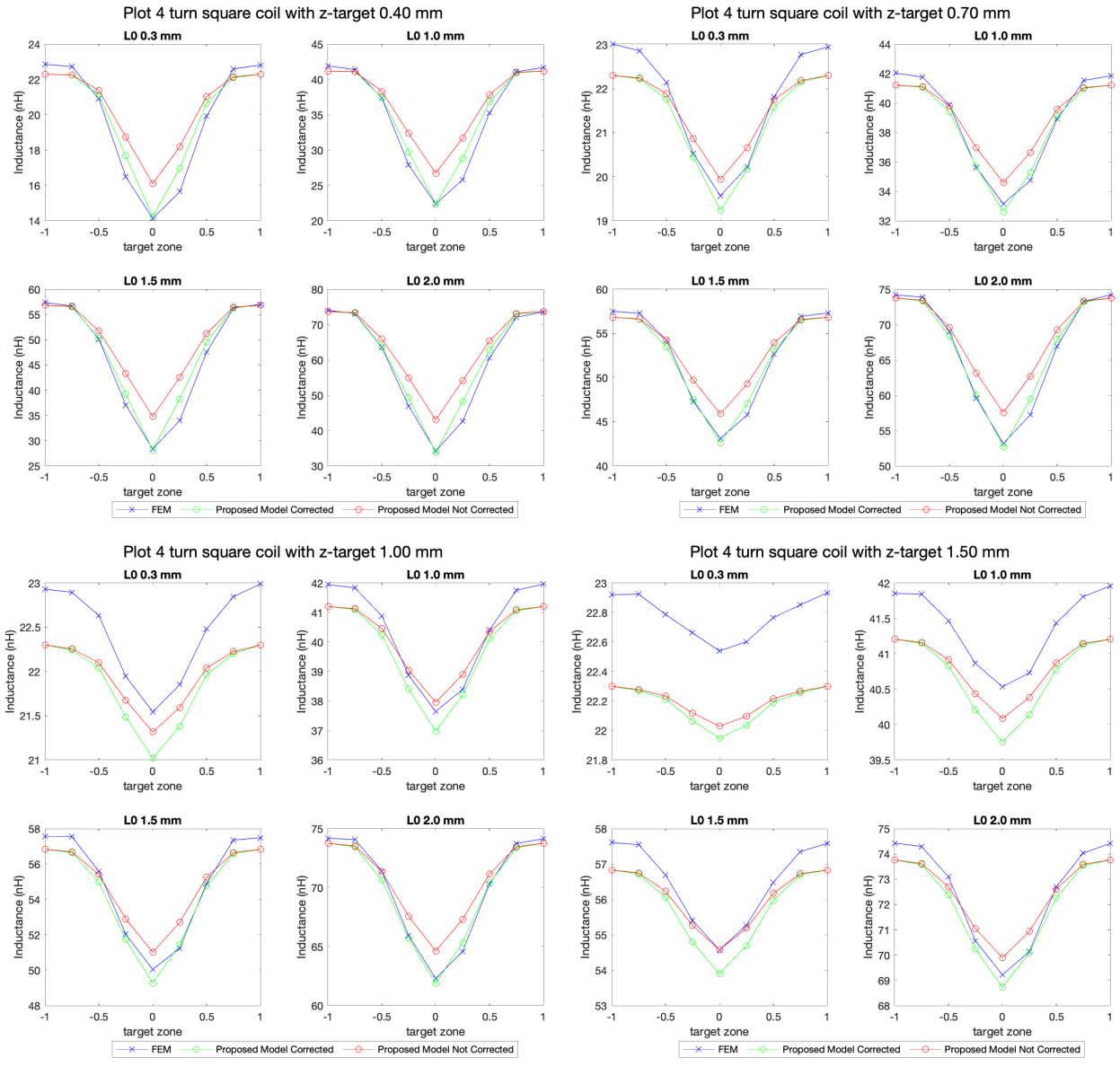

Figure 3.24: Inductance values for a moving target over a 4-turn square coil for several configurations of l_0, y_{target}, and z_{target}.

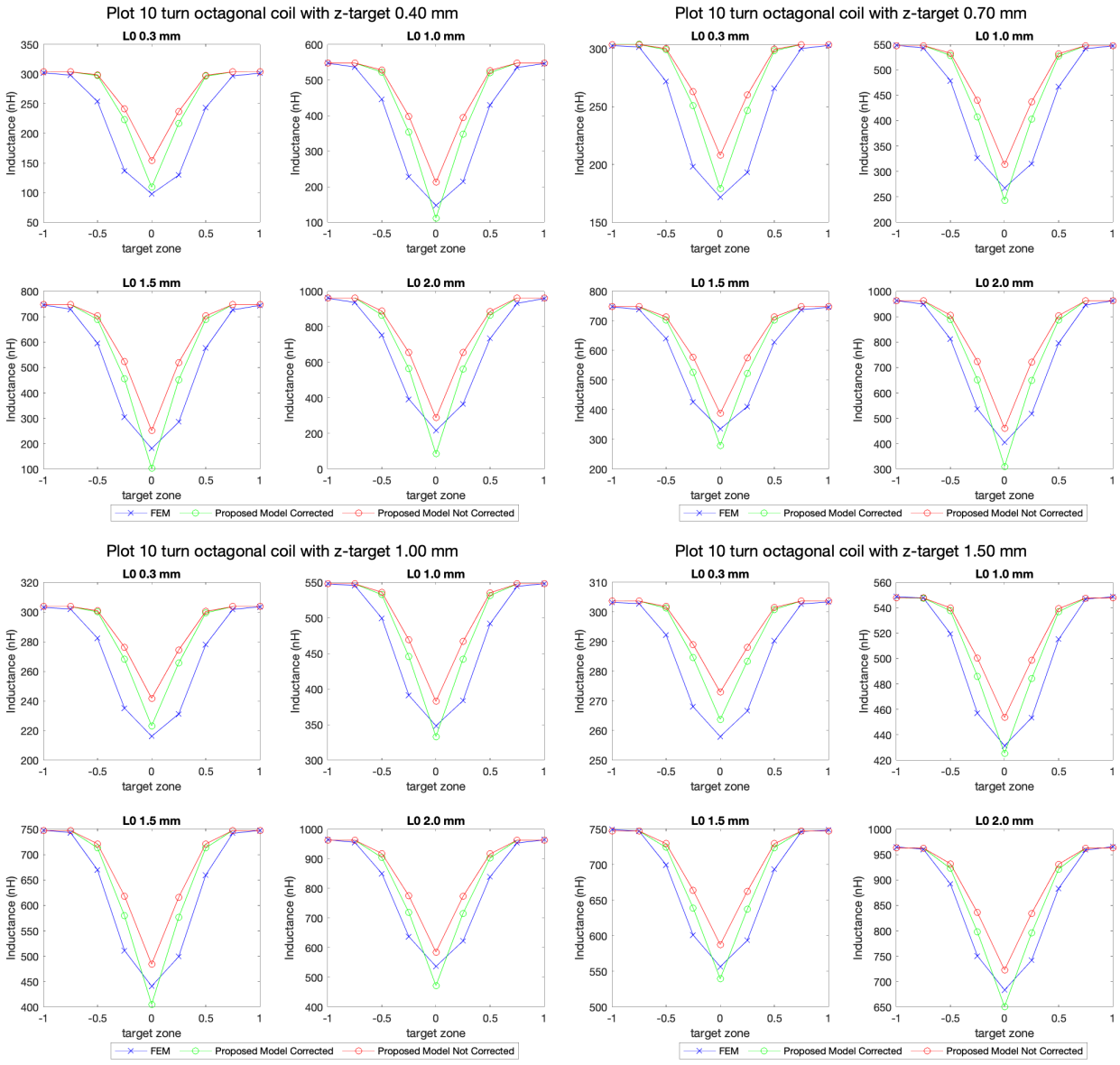

Figure 3.25: Inductance values for a moving target over a 10-turn octagonal coil for several configurations of l_0, y_{target}, and z_{target}.

increase. Thus, it can be concluded that this model offers greater accuracy for coils with smaller internal holes and with a smaller number of turns.

Table 3.2: The average error of the inductance value calculated by the proposed model in relation to the FEM model along with the target's translation movement.

*	**Coil**	$l_0 = 0.3$		$l_0 = 1.0$		$l_0 = 1.5$		$l_0 = 2.0$	
	layout	$N4$	$N10$	$N4$	$N10$	$N4$	$N10$	$N4$	$N10$
F	Square	2, 90%	4.37%	2.80%	4.34%	3.02%	4.35%	3.37%	4.37%
S	Square	2.07%	2.87%	1.55%	2.81%	1.66%	2.83%	1.90%	2.87%
F	Hexagonal	4.13%	10.80%	5.76%	11.31%	6.49%	11.74%	7.41%	12.07%
S	Hexagonal	1.96%	7.05%	3.27%	7.72%	3.99%	8.25%	4.89%	8.71%
F	Octagonal	4.60%	12.24%	6.03%	12.38%	6.58%	12.44%	7.33%	12.20%
S	Octagonal	2.23%	7.98%	3.53%	8.45%	4.19%	8.80%	4.99%	8.88%
F	Decagonal	6.65%	14.56%	7.38%	14.82%	8.02%	14.71%	8.86%	14.36%
S	Decagonal	3.94%	9.61%	4.68%	10.37%	5.48%	10.73%	6.36%	10.86%

* Where F corresponds to the average inductance value for all z_{target} values, and S to z_{target} from 0.7mm to 1.5mm.

3.4 Experimental results

3.4.1 1- and 2-Layer Planar Coils Experimental Validation

In order to have a complete validation of the proposed model, experimental measurements of self-inductance were performed on manufactured coils with several different geometries. For this experiment, the minimum coil wire's width (w) and space between turns (s) used in the test coils were of 0.15 mm. Figure 3.26A shows the PCB fabricated with the different one-layer coils namely 4, 6, 8, and 10 segments per turn, with an inner segment of 1.3 mm. These coils were grouped in two sets, one with ten turns (on the top line) and another with eight turns (on the bottom line).

In each line and for each geometry, there was a pair of coils, one with wire's width (w) and space between turns (s) equal to 0.15 mm, and another one with wire's width equal to 0.15 mm and space between turns equal to 0.20 mm. In Figure 3.26B the two-layer coils are visible, showing the different geometries of 4, 6, 8, and 10 segments per turn, with an inner segment of 1.3mm. For the two-layer coil, only coils with 10 turns were fabricated. The distance between each coil was chosen in a way that the space was maximized, without creating any effect in the single coil experimental measurement. This was confirmed by comparing the results of a single coil board with the multi-coil measurement setup, without detecting major differences. To minimize any error in the measurement setup, as well as in the coil manufacturing process, two sets of PCBs were produced and the self-inductances in both of them were measured thirteen

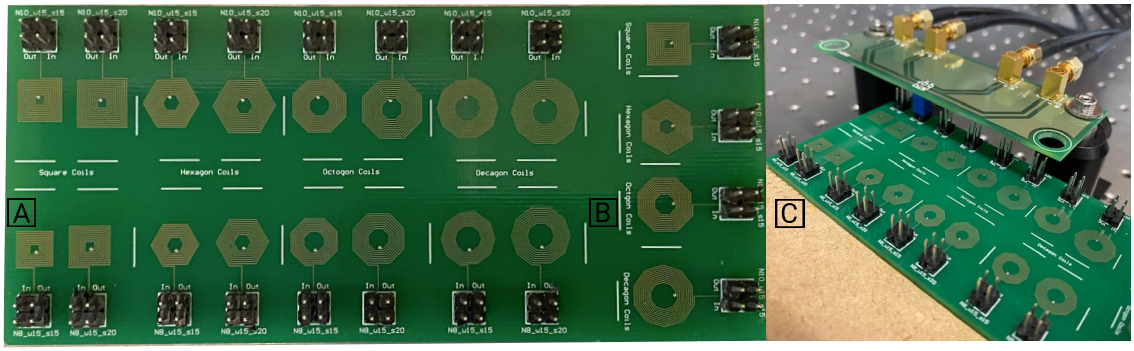

Figure 3.26: The PCB produced has coils with 4, 6, 8, and 10 segments per turn, all with an inner segment of 1.3 mm. In A: are represented the one-layer coils, in the top line are coils with ten turns and in the bottom line coils with eight turns; in B: are the two-layer coils, with ten turns; and in C: the measurement setup.

times. The Keysight Technologies E4980AL-102 LCR precision meter [3.6], was used for the inductance measurements at the test frequency of 1MHz, with a four point Kelvin customized probe set-up. In order to minimize measurement errors, the measurement setup depicted in Figure 3.26C was developed to plug the coils' PCB to the LCR meter, after the calibration process (Figure 3.27).

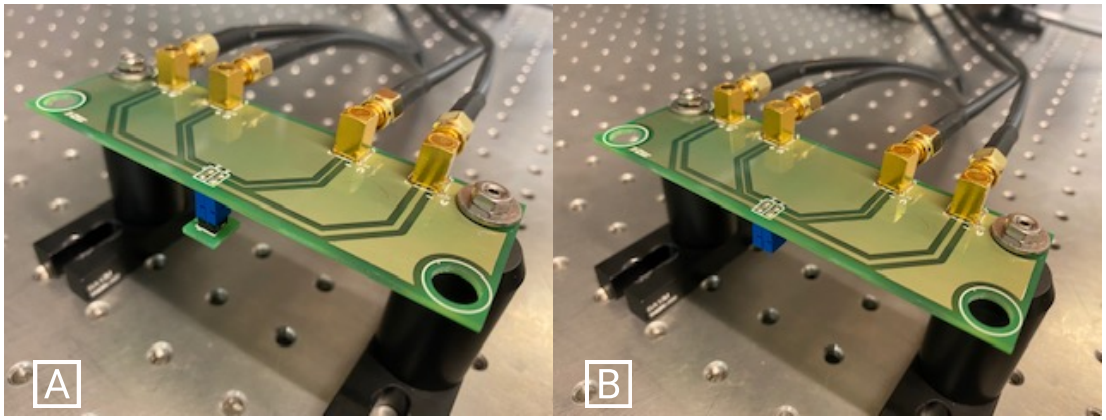

Figure 3.27: Calibration setup. (**A**): Short-circuit. (**B**): Open-circuit.

To compare the experimental measurement of the fabricated coils with the FEM model used as reference, the thirteen LCR measurements were averaged. During the experimental evaluation process, the maximum deviation registered in both PCBs was around 0.68% for the one-layer coils, and 0.48% for the 2-layer coils, which proves the high precision of the measurements. The results for the experimental, FEM simulations with connector, and the proposed model (for the one-layer coil designs) are depicted in Figure 3.28. The detailed analyses of the relative errors between the experimental measurements are visible in Figures 3.29 and 3.30.

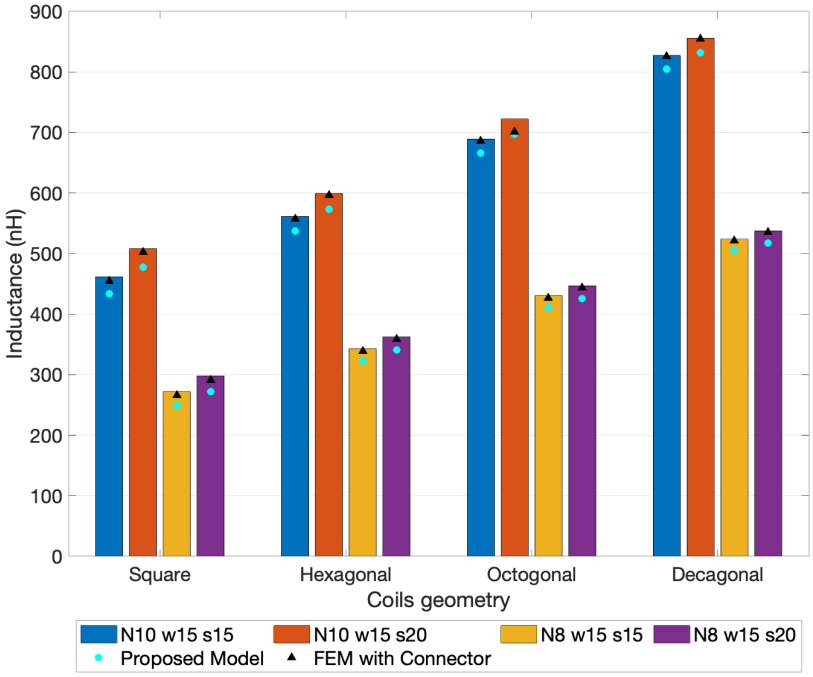

Figure 3.28: Graphic with the average inductance values from the experimental measurements and FEM simulation results.

In Figure 3.26A, it is noticeable that to perform the measurements, two traces were added to the printed coils, from the coil's extremities to the connectors. For this reason, it was expected that the inductance values measured with the LCR should be higher than the ones obtained from the model, and the FEM simulations presented before (as it only considered the coil element). In order to understand the impact and quantify this effect, a FEM model was made with two connecting traces coming out the coil towards the air box. As predicted, when considering the connecting traces, higher inductance was registered and the error to the experimental measurement was minimized. Comparing the data for single layer coil's from FEM model, one can observe that considering the connecting wires led to an error reduction of around 2% for $N = 10$, and 3% for $N = 8$.

Finally, the results calculated by the proposed model were compared with experimental measurements, as presented in Figures 3.29 and 3.30. The errors of the FEM models, with and without connectors, were also added to the representation always using the experimental measurement as reference. Note that the coils layouts simulated with the proposed model did not include the extended connecting traces (see Figures 3.10 and 3.16).

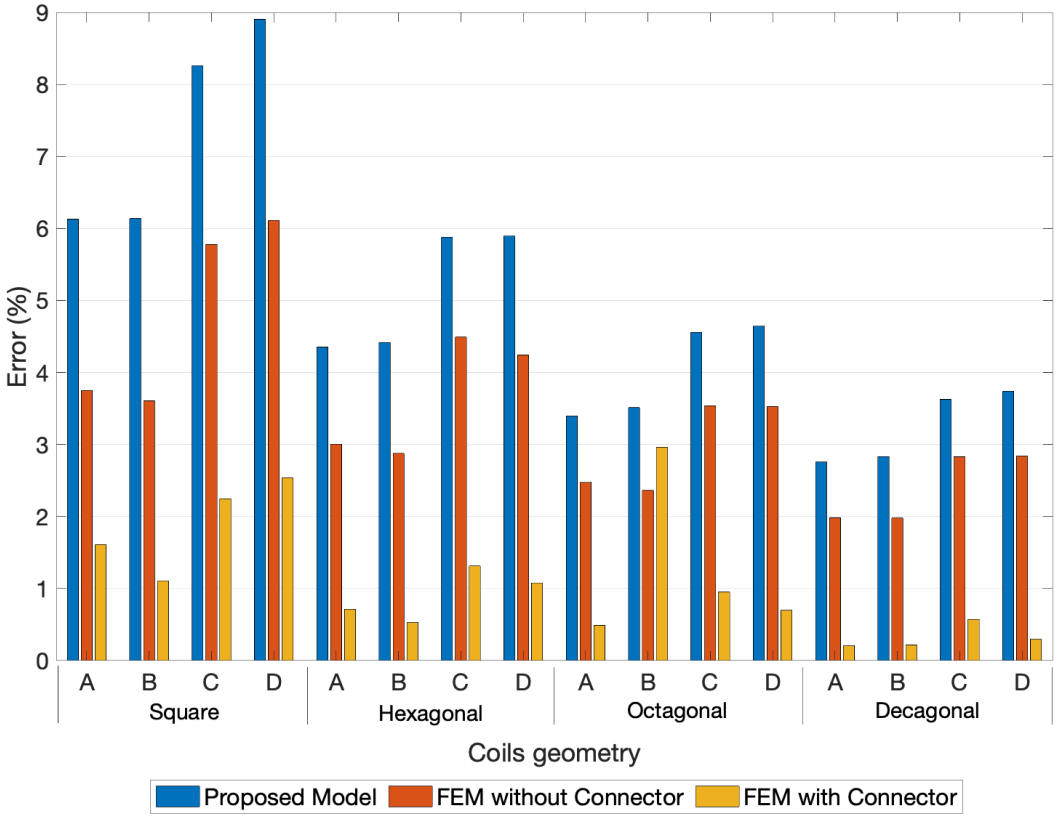

Figure 3.29: Relative errors module between the experimental measurements, the FEM simulations and the proposed model for the 1-layer coils. A-[$N = 10$, $w = 0.15$ mm, and $s = 0.15$ mm]; B-[$N = 10$, $w = 0.15$ mm, and $s = 0.20$ mm]; C-[$N = 8$, $w = 0.15$ mm, and $s = 0.15$ mm]; D-[$N = 8$, $w = 0.15$ mm, and $s = 0.20$ mm].

Comparing the errors of the FEM model without connectors and the ones from the developed model, it is perceptible that the major contribution to these errors was from the absence of the connecting traces in the analysis. Even with this geometry difference, the errors between the experimental measurements and the ones from the proposed model remain at an acceptable range, being in the case of the one-layer coils smaller than 9% for square coils, 6% for hexagonal coils, 5% for octagonal coils, and 4% for decagonal coils. In the case of two-layer coils, it was further minimized to values smaller than 5% for square coils, 3% for hexagonal coils, 2.5% for octagonal coils, and 2% for decagonal coils. It can thus be concluded that the developed model was valid and has good accuracy for both one- and two-layer coils induction calculation.

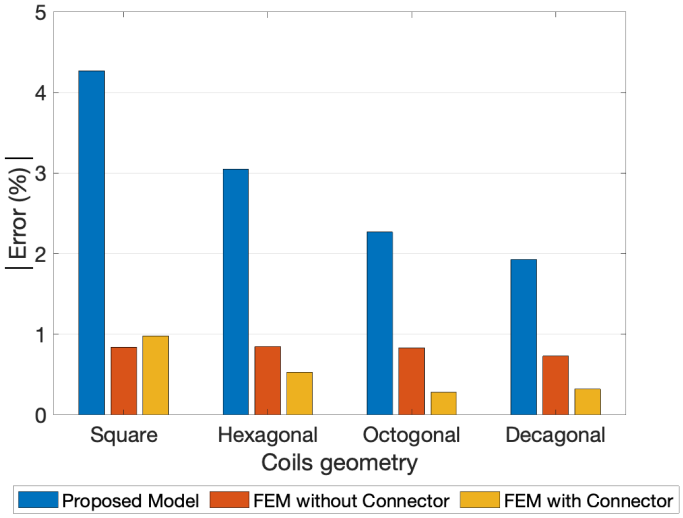

Figure 3.30: Relative errors module between the Experimental Measurements, the FEM simulations and the proposed model for the 2-layer coils with 10 turns, $w = s = 0.15$ mm, and a 1.3 mm inner segment.

3.4.2 1-Layer Planar Coils in the Presence of a Conductive Target Experimental Validation

After the validation of the proposed model to calculate the inductance values of 1- and 2-layer coils, the experimental validation of the approximation made to the model in the case of a planar coil in the presence of a conductive target was carried out. For this experiment, coils which geometry was already validated (Section 3.4.1) were used. Figure 3.31A shows front of the PCB produced with the different one-layer coils namely 4, 6, 8, and 10 segments per turn, with an inner segment of 1.3 mm and a wire's width (w) and space between turns (s) of 0.15 mm. These coils were grouped in two sets, one with ten turns (on the top line) and another with eight turns (on the bottom line). Figure 3.31B shows the back of the PCB produced, being perceptible that behind each coil there is a target under it. In each row of coils in Figure 3.31A there is a pair of equal coils with a target under them at different distances, as is perceptible in Figure 3.31B. The influence on the inductance of each coil is tested in the presence of a target at 1.105 mm (Δz_1) and 1.5 mm (Δz_2).

As previously evidenced, to perform the measurements, two traces were added to the printed coils, from the coil's extremities to the connectors. For this reason, larger deviations of the inductance values calculated by the proposed model in relation to those measured experimentally were expected.

Figure 3.32 shows the inductance values obtained from the proposed model (blue), FEM simulations (orange) and experimental measurements (yellow) for the set of coils presented in Figure 3.31. It is

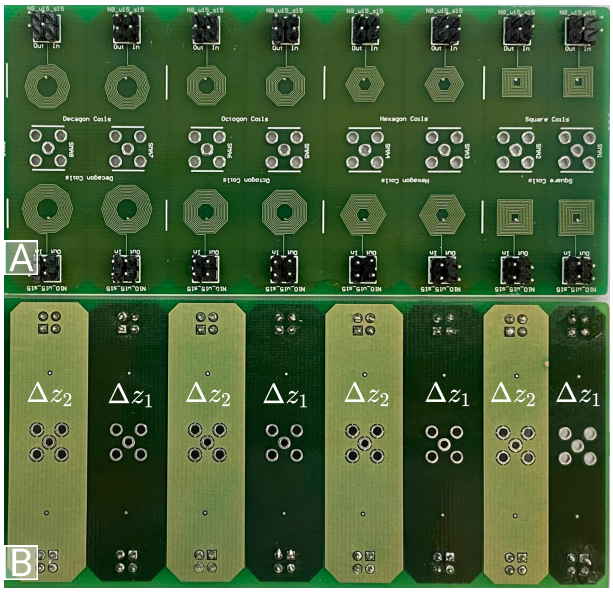

Figure 3.31: The produced PCB has 1-layer coils with 4, 6, 8, and 10 segments per turn, all with an inner segment of 1.3 mm. The coils with eight turns are on the upper row and the coils with ten turns on the lower row. Each equal pair of coils (on the same row) has a target at 1, 105mm (Δz_1) and 1.5 mm (Δz_2).

perceptible that for the case of the 8-turn coils the inductance values are closer to the experimental measurements than in the case of the 10-turn coils. The scenario in which the proposed model presents higher errors is for the case of the square coil with the target at 1.105 mm. In the case of the 8-turn square coil, the model has an absolute error of about 18% in relation to the experimental measurement and 10% to the FEM. In the 10 turns, the error is higher, as predicted, and around 23% when compared to the experimental value, while the FEM simulation presents an error of 22%.

For the cases of hexagonal, octagonal, and decagonal coils where the target is 1.5 mm apart, the model presents absolute errors smaller than 10% in relation to the experimental measurements and FEM simulations. Specially, in the case of the 8-turn coils, the absolute measurement error for the hexagonal is under 9%, for the octagonal is 8% and for the decagonal is 7%. However, the absolute errors between the proposed model and the FEM simulations in these cases are much lower, namely around 3% in the hexagonal coil, 2% in the octagonal and 1% in the decagonal. Concerning the 10-turn coils, the absolute errors between the proposed model and the measurements are around 10% in the case of the hexagonal coil, 9% in the octagonal , and 8% in the decagonal. Comparing the proposed model with the FEM model, the absolute errors in the case of the 10-turn hexagonal coil is around 9%, in the octagonal 8%, and in the decagonal 7%.

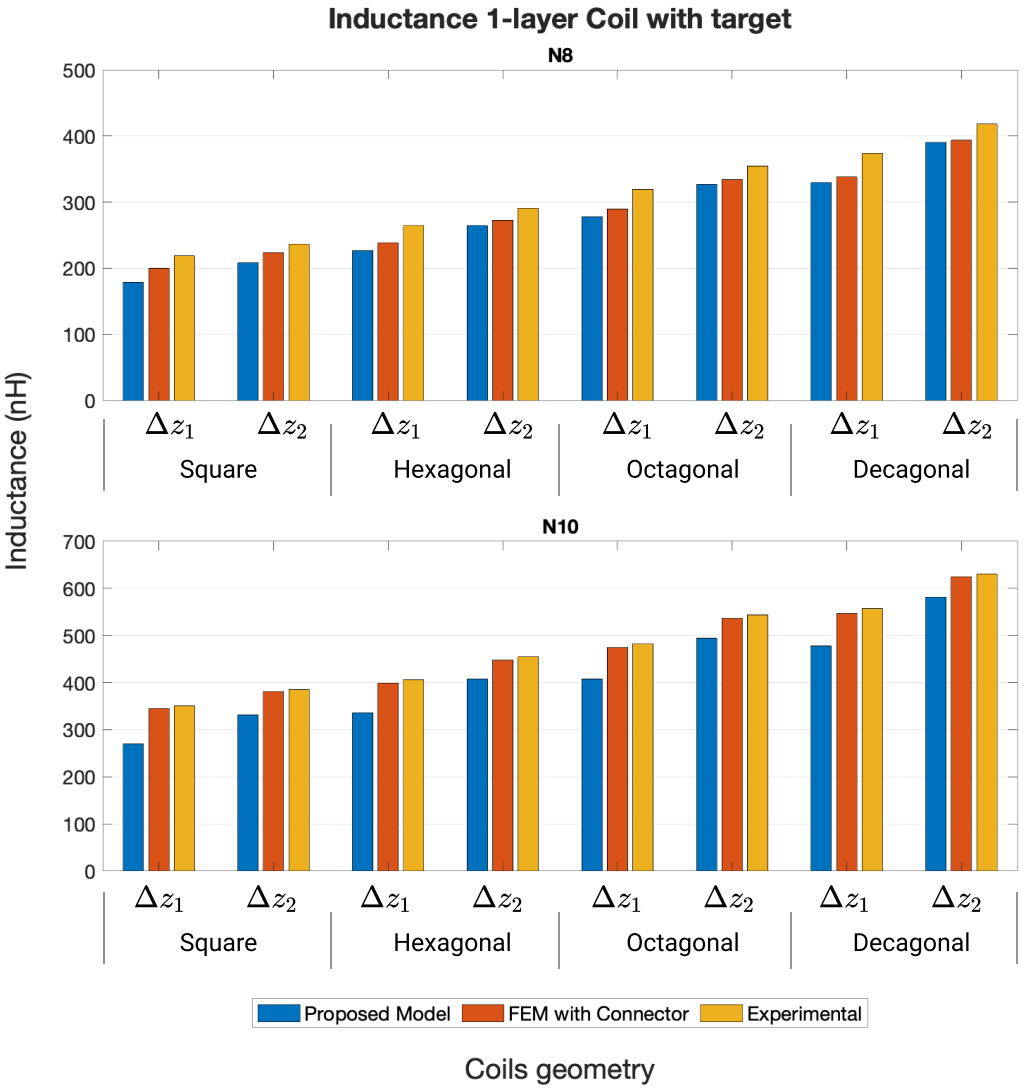

Figure 3.32: Inductance values of 1-layer coil in the presence of a target perfectly aligned obtained from the proposed model, FEM simulations and experimental measurements. Δz_1 and Δz_2 corresponds to the cases when the target is distanced from the coil 1.105 mm and 1.5 mm respectively.

3.5 Conclusion

In this chapter the implementation of the developed analytical model for three scenarios: (i) self-inductance of a 1-layer planar coil; (ii) self-inductance of a 2-layer planar coil; and (iii) self-inductance of a 1-layer planar coil in the presence of a conductive target was described. In order to validate the accuracy of the developed analytical model for all these scenarios, several approaches were simulated (i.e. varying the geometry of the coils, the number of turns, space between turns, coil's wire width, internal and external diameter, and the amount of coils used and their position). The inductance values obtained through the proposed model were compared with the methods used in the literature to calculate the inductance. In the case of the (i) and (ii) scenarios, the comparison with some analytical approximated formulas and FEM simulations was made, and in the (iii) case only FEM simulations were compared, since no other methods can be used.

Analyzing the results, it is possible to conclude that the main strengths of the proposed model compared to other approaches are the low computing time and cost associated with it, and its simplicity of use and adaptation to different geometries and combinations of coils and targets. As for its accuracy, comparing with the generic equations, it can be concluded that the developed method results are more precise, also presenting the advantage of being valid for more configurations of coils. Comparing with the simulations using FEM models, considering the computational resources, the time spent and the errors obtained, during a design phase of a sensor or planar coils, it can be concluded that the developed model is effective for a phase design approach. To validate the previous theoretical conclusions, experimental measurements of the three case scenarios ((i), (ii), and (iii)) were performed. For the scenarios (i) and (ii), was possible to conclude that the proposed model presents an accuracy in concordance with the one obtained through FEM simulations. The errors difference between the results obtained with the developed model and the FEM in relation to the measurements, are below 3%. For the case of the validation of the proposed model for the scenario (iii), with a conductive target aligned with the coil, the proposed model is not so accurate as FEM. However, an option to improve the accuracy of the proposed model is to consider the connectors that were used in the PCB coils and in FEM. Another option to improve the model is to enhance the approach that was made to the target, considering it as a coil with more than one turn.

Overall, it can be concluded that during the designing phase of a planar coil, the proposed model can replace the FEM simulations to calculate its inductance with a high approximation. With regards to the calculation of the inductance of planar coils in the presence of a target, it can be concluded that the approximation used in the proposed model is less accurate than FEM. It is not so precise for square coils and coils with a higher number of turns. However, in the remaining geometries, the errors between the

measurements and the calculated results are around 10%, which is still admissible for an approximation with an analytical model.

References

[3.1] J. N. Snyder and F. C. Grover, Inductance Calculations Working Formulas and Tables, 85. 180 Varick Street New York, N. Y. 10014: Dover Publications, Inc., 1964, vol. 18, p. 164, isbn: 0876645570. doi: 10.2307/2003443.

[3.2] H. Greenhouse, "Design of Planar Rectangular Microelectronic Inductors", IEEE Transactions on Parts, Hybrids, and Packaging, vol. 10, no. 2, pp. 101–109, Jun. 1974, issn: 0361-1000. doi: 10.1109/TPHP.1974.1134841. [Online]. Available: http://ieeexplore.ieee.org/document/1134841/.

[3.3] M. C. Lin, How to Simulate Script, 2019. [Online]. Available: https://github.com/linmingchih/HowtoSim_Script/blob/master/spiral.py.

[3.4] A. Faria, J. Cabral, L. Marques, F. Alves, and J. Gaspar, "High precision , geometry independent analytical method for self-inductance calculation in planar coils", in Proceedings of the 2021 22nd IEEE International Conference on Industrial Technology (ICIT), Valencia, 2021.

[3.5] A. Faria, L. Marques, C. Ferreira, F. Alves, and J. Cabral, "A fast and precise tool for multi-layer planar coil self-inductance calculation", Sensors, vol. 21, no. 14, pp. 1–18, 2021, issn: 14248220. doi: 10.3390/s21144864.

[3.6] Keysight, Keysight Technologies E4980A Precision LCR Meter E4980AL Precision LCR Meter. [Online]. Available: https://www.newark.com/keysight-technologies/e4980al-102/lcr-meter-20hz-1mhz-5-3kg/dp/28Y7427.

[3.7] H. Wakiwaka, D. Ito, K. Tashiro, H. Yajima, Y. Manta, T. Kanazawa, and N. Fujiwara, "Simplified calculation method of planar coil impedance considering the eddy current distribution by using finite element method", Materials Science Forum, vol. 792, pp. 215–220, 2014, issn: 02555476. doi: 10.4028/www.scientific.net/MSF.792.215.

[3.8] N. Misron, L. Q. Ying, R. N. Firdaus, N. Abdullah, N. F. Mailah, and H. Wakiwaka, "Effect of inductive coil shape on sensing performance of linear displacement sensor using thin inductive coil and pattern guide", Sensors, vol. 11, no. 11, pp. 10 522–10 533, 2011, issn: 14248220. doi: 10.3390/s111110522.

Chapter 4

Development of an Angular Position Sensor based on Multi-layer Planar Coils

After the assessment and validation of the functionalities of the developed tool that calculates with high accuracy the self and mutual inductances of PCB printed planar coils, and the resultant inductance of a planar coil when in the presence of a conductive target, this tool will be used to design and assess an automotive angular position sensor.

In this way, and considering the motivation of this thesis, the sensor chosen to validate the tool was the Differential Coils APS, which was developed during the Sensible Car Project.

In Section 4.1 the working principle of the sensor is described, as well as its constraints and requirements, and how it was developed. Section 4.2 describes the development and validation of the coils design, the integration of the developed tool on the coils design phase, and in which way it defers from the conventional design. Section 4.3 presents the experimental validation of the sensor's behavior and the comparison of the obtained values, using conventional and this thesis proposed methodologies, from real measurements. In the end, the impact that the developed tool has on the designing process of a sensor based on planar coils is shown, highlighting its advantages and disadvantages face to the commonly used method.

4.1 Differential Coils APS

In Section 3.3 the application of the analytical developed model for a planar coil with a electrically conductive target moving linearly over it, is described. However, the model is flexible enough to be applied to angular position sensors, when the conductive target has a rotational displacement. Figure 4.1 depicts

the linear (left) and angular (right) displacements of the target. As expecting, the inductance of the coil has a sinosoidal shape (minimizing the harmonics) for both type of displacements.

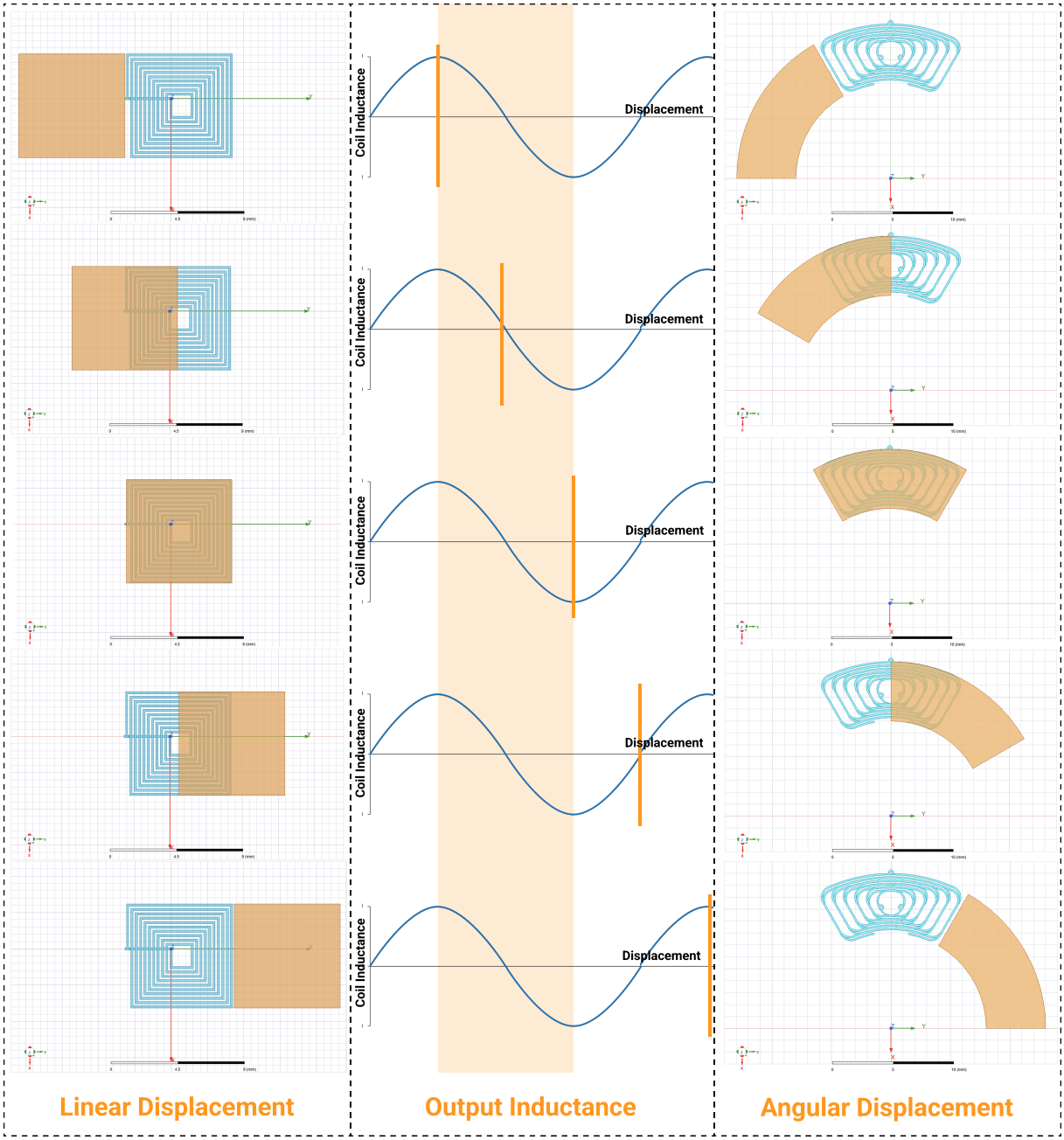

Figure 4.1: Inductance variation for a linear and angular movement of a conductive target over a planar coil.

In the case of the angular displacement, it can be noted that for a target rotation of 90 mechanical degrees, the inductance signal has one period (which represents 360 electrical degrees). So, in order to have a measurement of 360 mechanical degrees (a complete turn), four periods are needed. Figure 4.2 shows an example of a sensor's design, for a full turn measurement. Three pair of coils (L_{blue}, L_{red}, and L_{purple}) and a target with four parts (in black) are depicted. This configuration allows to have three

inductance sinusoidal signals (from each pair of coils) shifted by 120 electrical degrees. Then, these signals are used to calculate the angle of rotation, as some encoders use (Section 2.1).

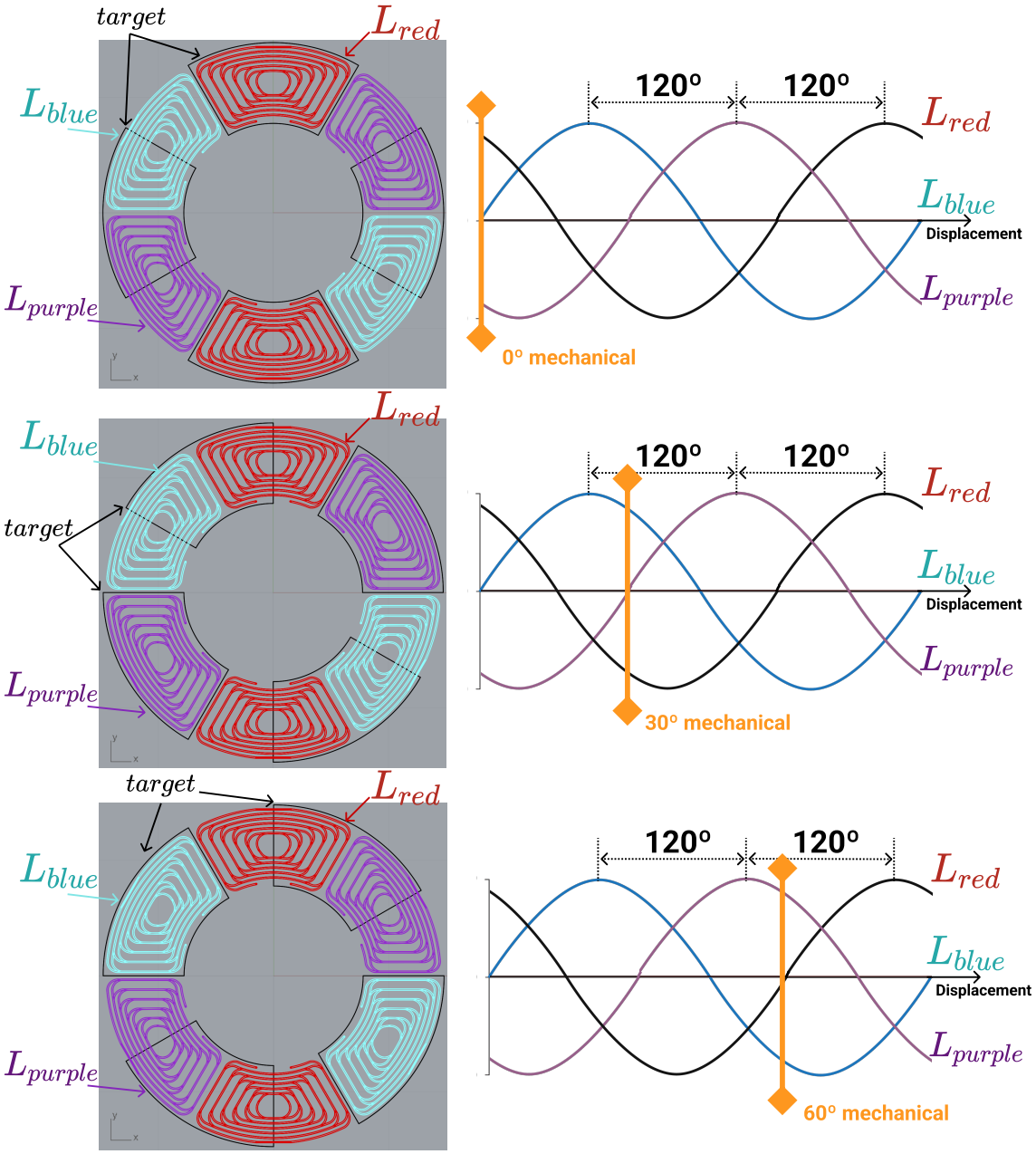

Figure 4.2: Inductance variations for a 90 degrees mechanical rotation of a conductive target over a planar coil.

To validate and highlight the impact that the developed tool has on the designing process of a sensor based on eddy currents, the Differential Coils APS was selected. This sensor can be applied, for example, to sense the angular position of a vehicle's auxiliary braking motor steering wheel position (Bosch LWS sensor). Thus, to measure the motor's angle of rotation with this sensor, it is necessary to mechanical couple on a electrically conductive plate (the motor shaft, which geometry is visible in Figure 4.3B) and

the PCB board with the reading circuit, as depicted by Figure 4.3A. The target rotates with the motor and the PCB remains stationary.

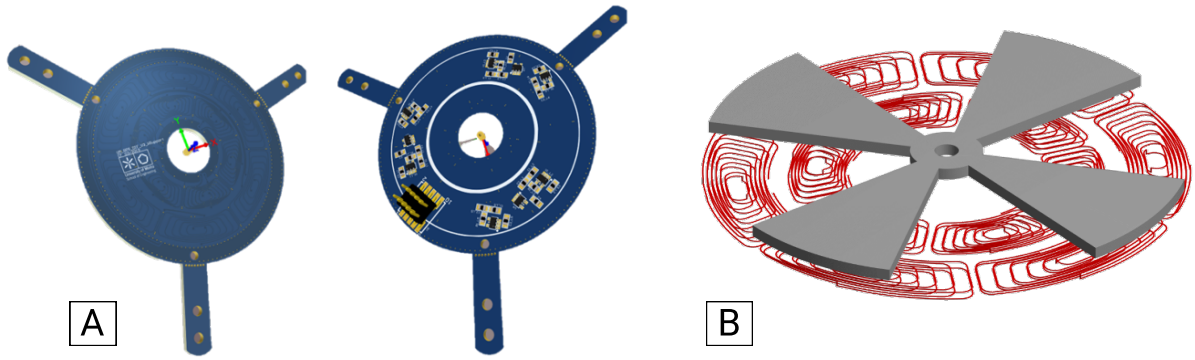

Figure 4.3: Differential Coils APS: A: PCB sensor; B: Coils and target geometry.

The main objective of this sensor is to measure the angular position based on the eddy current effect, using multi-layer planar coils printed on PCB and electrically conductive plates, both strategically designed to measure a range of 90 degrees, with a maximum error of 0.15 degree.

This automotive sensor features a particular design and positioning of its coils. This design was the result of an intensive research work in order to achieve the best combination between the geometry of the coils, their interconnection, and positioning, so that the sensor would offer the best performance in terms of resolution and precision. An innovative design was proposed that ended up being patented (currently in approval phase).

From previous published patents [4.1]–[4.3], in order to make the sensor immune to external interferences that may occur during measurements, the design uses inner and outer coils (depicted in Figure 4.3B)), thus allowing a differential measurement. In this way, it is possible to mitigate external interferences such as: (i) temperature variations, since these variations are reflected in the magnetic permeability of materials, thus changing the inductance of the inductors; (ii) noise in interface the bus lines and from the oscillators; and (iii) influence of stray magnetic fields external to the system.

In what concerns the drive of the inductors, this sensor uses a low cost and simple LC oscillator for each pair of coils, creating this way an alternating current that generates an alternating magnetic field. The automotive LC digital oscillator Texas Instrument SN74AHC1G00 Integrated Circuit (IC) (composed by one resistor, two capacitors, one inductor and a simple NAND logic gate) was the oscillator chosen. Its simple logic gate, in addition to conditioning the signal, also allows the direct connection of the measurement system to a microcontroller, since its output values oscillate between common digital voltage values. In

order to simplify even more the structure, the oscillator's inductor corresponds to the own coils used by the sensor for the measurements. Figure 4.4 illustrates the oscillator circuit used by the selected APS, corresponding the coil **L1** to a pair of inner or outer coils of the sensor. This way, each pair of coils is driven by its own oscillator, which is tuned onto a unique frequency, to avoid frequency locking and "cross-talk" between adjacent pairs of coils.

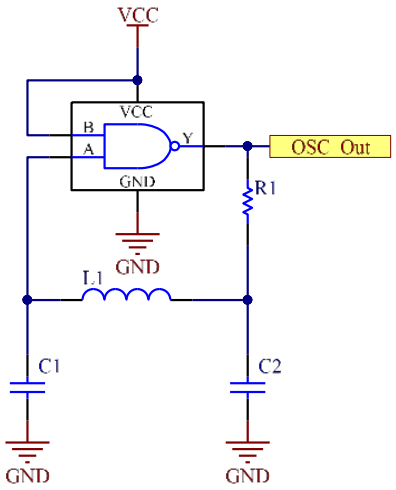

Figure 4.4: Electronic schematic of LC oscillator of the Differential Coils APS.

The output of each oscillator is a square wave whose frequency is dependent on the inductance of its own pair of coils, so every time there is a variation in the inductance of the coils, due to the effect of the eddy currents generated in the metallic target, there is a variation in the frequency of the oscillator. This frequency value can be roughly approximately by:

$$f_{osc} \approx \frac{1}{2\pi\sqrt{LC}} \tag{4.1}$$

where L corresponds to the inductance of a pair of coils and C to the capacitance value of the capacitors of the oscillator circuit.

The differential measurement principle is obtained using a D-type flip-flop. It receives at its inputs the frequency signals of both, inner and outer, oscillators. In **D** the signal from the outer pair of coils and in **CLK** the one from the inner pair of coils, as is visible in Figure 4.5. Thus, in the flip-flop output (**OSC Out**) will be the result of a sliding window subtraction of both signals, $f_{output} = f_{osc_{Inner}} - f_{osc_{Outer}}$. The resulting signal corresponds to a square wave with a sinusoidal variation of the frequency value with the angular displacement.

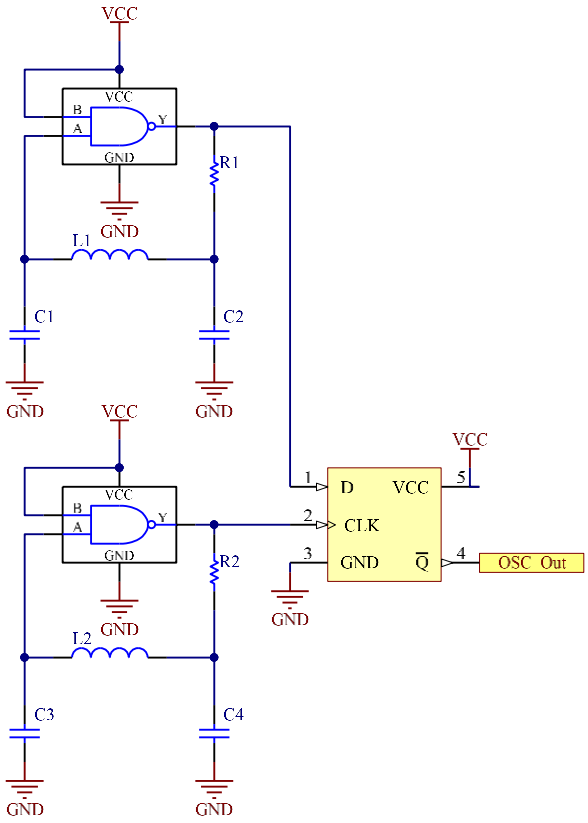

Figure 4.5: Electronic schematic of LC oscillators and the D-type flip-flop frequency subtractor (sliding window).

Figure 4.6A and B shows, in more detail, the coils architecture used by the sensor selected. It is noticeable that there are six equal coils in an inner radius (illustrated in a lighter tone) and another six in an outer radius (illustrated in a darker tone). Each of these coils is connected to its similar coil displaced 180 degrees, originating three pairs of coils in each inner and outer radius. In order to better understand this connection, in Figure 4.6A each pair of coils in the inner and outer radius coils is highlighted in the same color, having the inner coil a lighter tone, and the outer one a darker tone. Figure 4.6B shows that all the coils of the sensor have two layers, which increase the overall inductance of each coil without increasing its size across.

Each of these pairs of coils has its own oscillator tuned to a unique frequency. Thus, the APS differential sensor has six oscillator circuits and three flip-flops to perform the subtraction (in sliding window) between the inner and outer coil pairs. This way, there are three frequency output signals, one for each differential pair of coils ($f_{L_{red_{inner-outer}}}$, $f_{L_{blue_{inner-outer}}}$, and $f_{L_{purple_{inner-outer}}}$ as depicted in Figure 4.7).

As mentioned before, the inductance value of each pair of coils differs according to the amount of area that the target is overlapping the coil. The larger the overlapping area, the greater the amount of eddy currents

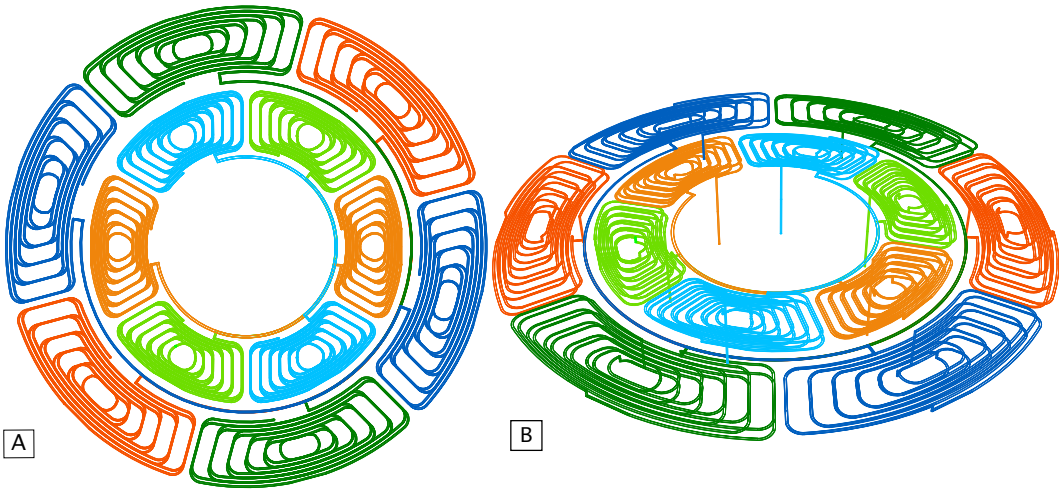

Figure 4.6: Sensor coils design. A: top view; B: perspective view.

generated in the target and smaller will be the precept coil inductance by the sensor. Based on the operating mode depicted in Figure 4.2, Figure 4.7 shows the three differential pairs of coils ($L_{blue_{inner\&outer}}$, $L_{red_{inner\&outer}}$, and $L_{purple_{inner\&outer}}$) of this differential APS sensor, and how it works. In a target rotation of 90 mechanical degrees, the frequency signal from each differential pair of coils, $f_{L_{red_{inner-outer}}}$, $f_{L_{blue_{inner-outer}}}$, and $f_{L_{purple_{inner-outer}}}$ (shifted by 120 electrical degrees), does one period (which represents 360 electrical degrees).

Through the analysis of Figure 4.6A it is perceptible that both inner and outer coils are misaligned. As this is a differential sensor, if both inductances are in phase (internal and external coils aligned), the subtraction between them would not be favorable. By subtracting these two in-phase signals, the final inductance value would be much smaller when compared to subtracting out-of-phase signals. Thus, to maximize the output amplitude, the internal coils were rotated 45 degrees in relation to the external ones. In this way, the maximum inductance of one coil corresponds to the minimum of the other. Therefore, the signal resulting from the subtraction of both inductances has the maximum possible amplitude, which allows the sensor to have a higher resolution.

In the results of the first tests, erroneous sensor readings were obtained. It was noticed that magnetic coupling ("cross-talking") were happening between the coils, and that these were causing non linearities in the readings. In order to decrease the coupling factor and attenuate the amount of harmonics generated, different distances between the wires of the coil were used, as depicted in Figure 4.6. This design aims to concentrate the magnetic field generated by each coil at its center, significantly reducing the coupling between adjacent coils. Allied to this is the displacement between the inner and outer coils, explained above, and the frequency of the different oscillator circuit, which further reinforces this attenuation effect,

by moving the centers of the coils further apart.

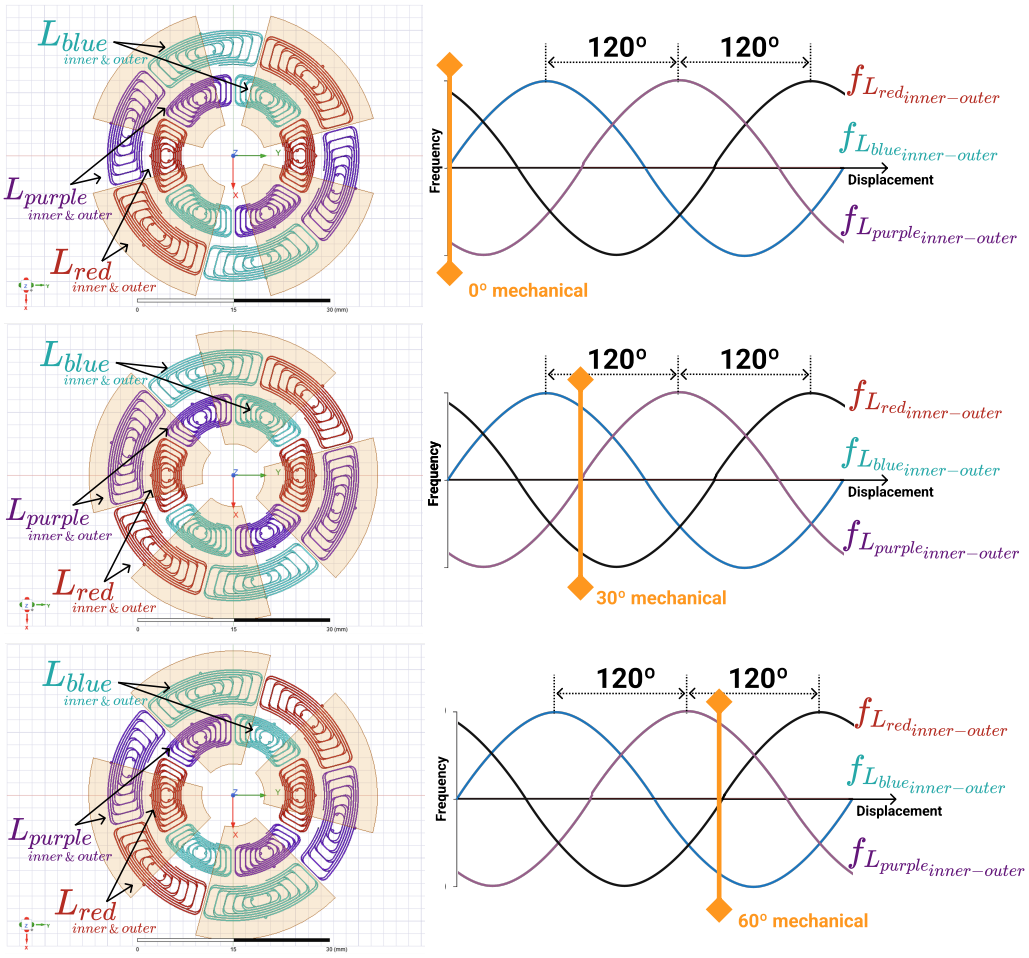

Figure 4.7: Inductance variations from each differential pair of coils, for a 90 degrees mechanical rotation of the Differential Coils APS (amplitude and phase corrected by software).

Figure 4.8 explicitly illustrates this magnetic field concentration. The values of both graphics were obtained experimentally using an Radio Frequency (Radio Frequency (RF)) probe. From a single axis and operating at nominal frequencies, the sensor signal amplitude was measured, every 100 μm, using an oscilloscope, in order to linearly traverse the entire PCB board. From the color scale of the graphics, it is clear that there is a concentration of the magnetic field of each coil at its center, and that on the borders of the adjacent coils the field values intensify slightly. Thus, it can be inferred from these measurements that this coil design enables an efficient minimization the interference between adjacent coils. In addition, this feature combined with the differential measurement significantly reduces the amount of noise in the system, contributing to the improvement of the linearity of the sensor's response.

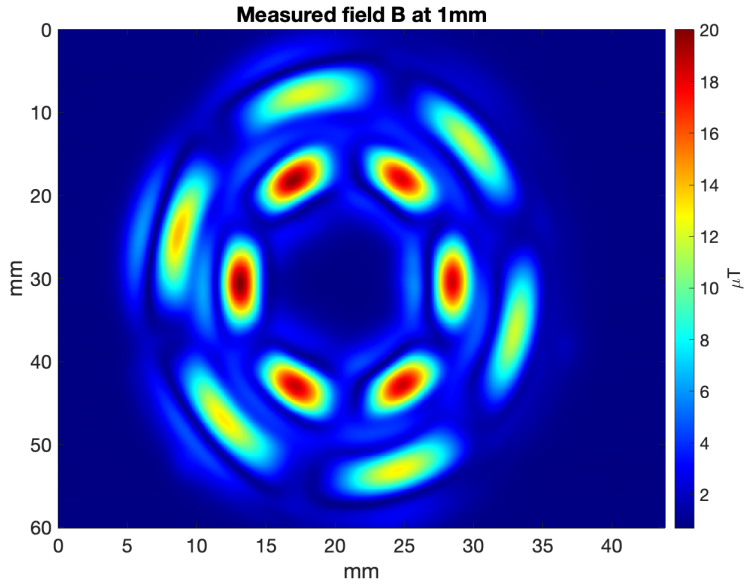

Figure 4.8: Graphics with the measured magnetic field of the sensor coils.

4.2 Coils Design and Validation

The coil design of the Differential Coils APS was carried out using Rhinoceros®Software plug-in, in order to make the coil's more flexible, versatile, and efficient. Thus, by programming the coil design, it is possible to easily modify the configuration of the APS coils, such as (i) changing its dimensions, changing only the values of the respective variables (number of turns, space between turns, wire's width, and inner and outer radius); (ii) manipulate its geometry, easily adding or removing commands in the script; (iii) add and correctly connect different geometries, avoiding problems with intersections or connections; and (iv) save the various structures (points, curves, surfaces, solids) through variables, facilitating their selection for future iterations. After the design using the script the coil can be imported to Ansys®and to Altium®.

Figure 4.9 shows the implemented coil geometry in more detail. To increase the inductance of the coil without increasing its area, it can be said that four coils have been compiled into one, two in the upper layer and another two in the lower layer. When analyzing the coils in Figure 4.9, it is noticeable that the current flows from point **A** to **B** of the upper **coil 1**, going down to **coil 2**, flowing from **B** to **C**. Then it goes back to the upper layer, to **coil 3**, flowing from **C** to **D**, back to the lower layer, to **coil 4**, flowing from **D** to **E**.

A set of parameters had to be defined to allow the implemented script to generate the inner and outer coils of the sensor (presented on Figure 4.6), namely: number of coil's turns; amount of coils; wire's width; space between turns; thickness of the wire; distance between layers; minimum radius of the coil;

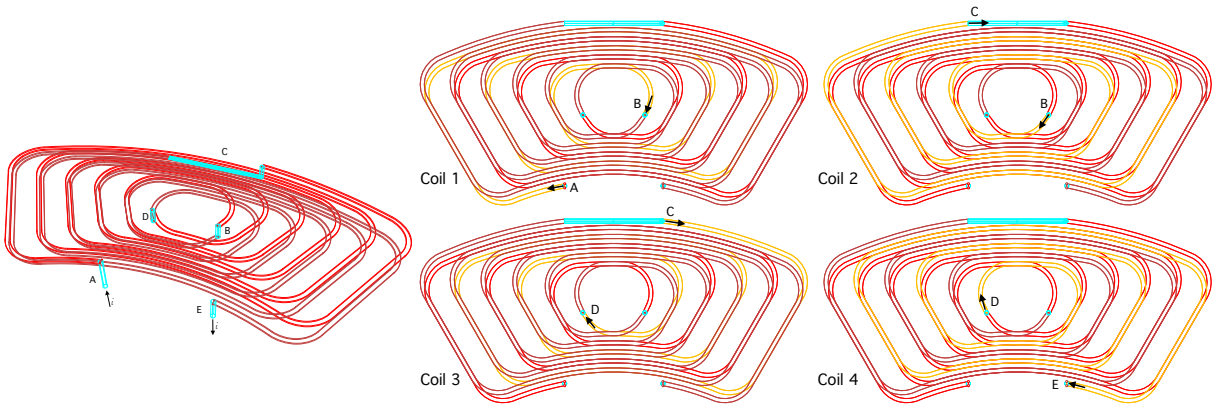

Figure 4.9: Coil's Design. In blue are represented the coil's connectors, in red the four "sub-coils", and at right is highlighted in yellow each one of the "sub-coils".

maximum radius of the coil.

4.2.1 Conventional Validation of the Coils Design Phase

When the planar coil geometry does not follow any of the regular patterns mentioned in Section 2.2 or falls outside the range of application of the presented approximation formulas, the way that is usually used to calculate the coil inductance is through finite element simulations. In the development of the Differential Coils APS to perform this type of simulation, the Ansys®Software was used, specifically the eddy current mode.

To develop the FEM simulation model, first, the geometry had to be defined to be simulated. Since Ansys®cannot interpret files with the Rhinoceros®extension, it was necessary to export the coil's geometry into a STEP file. After importing this file into Ansys®, it was necessary to check the geometry and delete some unwanted surfaces/solids that were generated upon file conversion import. In order to enable the software to simulate the magnetic simulation of the coil an air-box had to be inserted in the model. Since the size of the air-box corresponds to the volume where the magnetic field will be calculated, thus its dimensions influence the results of the model. Several simulations were carried out in order to identify the offset value between the air-box and the coil design, which is more suitable for this model. After an iteration process, it was found that there is a saturation of results from a 6 mm offset. In this way, the sensor model was simulated using an air-box with this offset value so that there was no interference in the results. Then follows the application of the current in the coil's terminals, as can be seen in Figure 4.10. A test current of 500 mA was used, with the solver frequency selected to be 1 MHz, in order to match the experimental test frequency, that was later performed. The adaptive setup was configured with a percent error of 1%, and a minimum of two convergence steps.

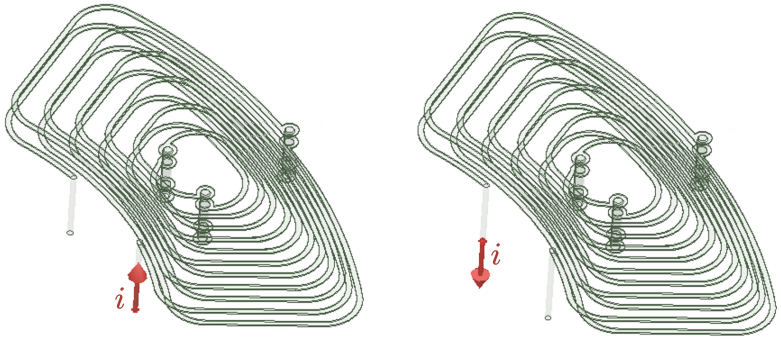

Figure 4.10: Inner Coil with the current applied in its terminals.

With all the simulation's parameters defined the simulation could be made. Table 4.1 shows the inductance results obtained from the simulation **A** and **B**, for a inner and a outer coil. The simulation **A** was configured with an air-box with a 6 mm offset from the coils, and with no refinement of the mesh. The simulation **B** was configured with an air-box with a 21 mm offset from the coils, and with a refinement of the mesh in the coil and air-box. It was applied the curved surface mesh on both simulations, using the level 9 of refinement in the coil, and level 5 in the air-box. Considering the significant differences in the size of the air-box and the refinement of the mesh used in both simulations, when analyzing Table 4.1, it can be seen that the results obtained are identical. Thus, it can be concluded that the results of the simulation model with an air box size with 6 mm offset and no mesh refinement are valid.

Table 4.1: Inductance values obtained by the FEM simulation for the coils of simulation groups, **A** and **B**.

	Simulation A	**Simulation B**
Inner Coil	535.71 nH	536.01 nH
Outer Coil	761.22 nH	760.82 nH

4.2.2 Validation of the Coils Design Phase by the developed tool

As detailed in Chapter 3, the developed tool that implements the proposed analytical model is based on straight filaments, and in their central position in the wire. As depicted in Figure 4.6 the coils used by the sensor (APS) have curves, and without any geometry manipulation the developed tool it is not valid. This way, in order to import the geometry in MATLAB®, to be used by the developed tool, is necessary, for each one of the four "sub-coils" highlighted in Figure 4.9, to: (i) draw the central curve of the wire of the coil; (ii) convert the curve to a polyline, in order to discretize the curve into small straight filaments; (iii) extract the points of the polyline; and (iv) export the points into a CSV file. This way, for each outer or inner coil it will be exported four CSV files. This was the file format chosen, because it was the one

founded that could export the points through a predictable order (unlike STEP format), and that could be used by MATLAB®. Figure 4.11 shows the filaments and the points of the outer and inner coils geometries exported from Rhinoceros®to MATLAB®.

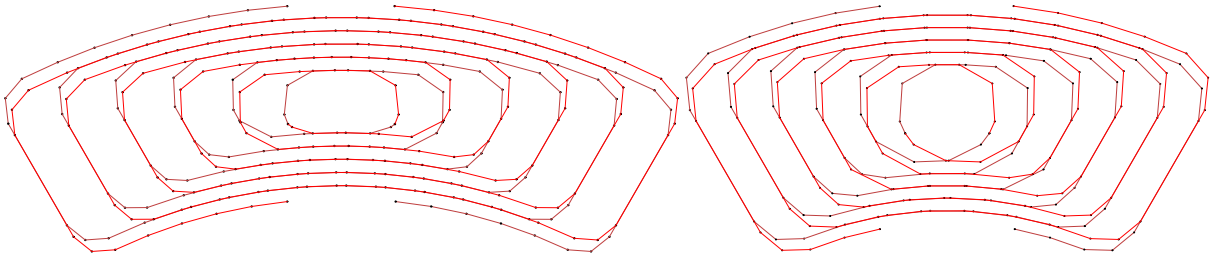

Figure 4.11: Points of the outer and inner coils geometries exported from Rhinoceros®to MATLAB®, using a minimum edge length of $1mm$ in the discretization process.

Once the four "sub-coils" are separated, it is possible to manage in MATLAB®the direction of the current in each of them, to follow the flow depicted in Figure 4.9. This way, after uploading and convert the data from the CSV files into matrices with the coils coordinates, the inversion of the orientation of the coordinates of the coils is done to guarantee the correct direction of the current. In order for the developed tool to calculate the inductance of the coil, it is only necessary to configure two parameters, the thickness and width of the coil wire. With this information, it is possible to calculate the self-inductance of each of the four "sub-coils", and the mutual-inductance between them. As explained in Section 2.2.1, the total inductance of the coil, composed by the four "sub-coils", is given by:

$$\begin{aligned} L_{total} = L_{Coil_1} + L_{Coil_2} + L_{Coil_3} + L_{Coil_4} + \\ 2 * (M_{mutual_{12}} + M_{mutual_{13}} + M_{mutual_{14}} + M_{mutual_{23}} + M_{mutual_{24}} + M_{mutual_{34}}) \end{aligned} \tag{4.2}$$

where L_{Coil_1}, L_{Coil_2}, L_{Coil_3}, and L_{Coil_4} are the self-inductances of "sub-coils" 1, 2, 3, 4, respectively, and $M_{mutual_{12}}$,$M_{mutual_{13}}$, $M_{mutual_{14}}$, $M_{mutual_{23}}$, $M_{mutual_{24}}$, and $M_{mutual_{34}}$ are the mutual-inductances between the four "sub-coils".

However, this inductance can be calculated in a different way. Instead of considering four "sub-coils" connected, both the sub-coils of the upper layer can be considered as one (concatenating their coordinates), and the same logic can be applied to the ones from the lower layer. In this way, the total inductance can be calculated by:

$$L_{total} = L_{Coil_{Up}} + L_{Coil_{Down}} + 2 * M_{mutual_{UpDown}} \tag{4.3}$$

where $L_{Coil_{Up}}$, and $L_{Coil_{Down}}$ are the self-inductances of the upper and lower "sub-coils", and $M_{mutual_{UpDown}}$ is the mutual inductance between them.

In order to validate the discretization of the coils, two sets of inner and outer coils were generated with different discretization parameters. Figure 4.12 shows the several function parameters that are possible to manipulate. Thus, the set **AA** of coils was created with all the default values of the function parameters, and the set **BB** was generated with a minimum edge length (dblMinEdgeLength) of 1 mm. In the set **AA** the inner coil is composed of 946 points, and the outer coil of 1006 points. In the set **BB** the inner coil is composed of 216 points, and the outer coil of 288 points.

ConvertCurveToPolyline

Converts a curve to a polyline curve.

Syntax

```
Rhino.ConvertCurveToPolyline (strObject [, dblAngleTolerance [, dblTolerance [, blnDeleteInput [, dlbMinEdgeLength [, dblMaxEdgeLength]]]]])
```

Parameters

strObject	Required. String. The object's identifier.
dblAngleTolerance	Optional. Number. The maximum angle between curve tangents at line endpoints. If omitted, the angle tolerance is set to 5.0.
dblTolerance	Optional. Number. The distance tolerance at segment midpoints. If omitted, the tolerance is set to 0.01.
blnDeleteInput	Optional. Boolean. Delete the curve object specified by *strObject*. If omitted, *strObject* will not be deleted.
dlbMinEdgeLength	Optional. Number. The minimum segment length. Specify 0.0 (Default) for no minimum limit.
dblMaxEdgeLength	Optional. Number. The maximum segment length. Specify 0.0 (Default) for no maximum limit.

Returns

String	The identifier of the new object if successful.
Null	If not successful, or on error.

Figure 4.12: Rhinoceros function used for the discretization of the coils.

The inductance values obtained by the developed tool for both set of coils, **AA** and **BB**, are visible in Table 4.2. It is possible to see that for both inner and outer coils the inductance values calculated by Equation 4.2 (L_{4Coils}) are always a littler higher than the ones calculated by Equation 4.3 (L_{2pairs}). However, this increase is less than 0.9% in all cases.

Table 4.2: Inductance values obtained by the developed tool for the coils of both sets, **AA** and **BB**.

	Set AA		**Set BB**	
	L_{4coils}	L_{2pairs}	L_{4coils}	L_{2pairs}
Inner Coil	558.77 nH	554.62 nH	540, 30 nH	535.70 nH
Outer Coil	845.83 nH	840.88 nH	825, 51 nH	820, 13 nH

Looking into the differences between the sets of coils, for the case of the inner coils there is a difference between the sets of around 3%, and for the outer coils around 2%. Considering this difference between the inductance results, the difference between the amount of coil points of both sets, and the time consumed by the developed tool in each sets, if a fastest solution is desired, the set **BB** with Equation 4.2 (L_{4coils}) is the better approach to use. However, if the simplest approach is desired, allied with low time consumption, the developed tool through the method L_{2pair} (Equation 4.3) is the most adequate, because

regardless of the number of sub-coils per layer they will be treated just as two, facilitating the calculations of interference from mass planes and targets in the coil inductance, which are explained in detail in the next section.

4.2.3 Difference from conventional and proposed methods

The main difference between the conventional method (FEM simulation) and the developed tool to calculate the inductance of a planar coil with an arbitrary geometry is the time-consumed by each method. The FEM models were simulated in a server with two processors Intel(R) Xenon(R) Gold 6130 CPU @2.10 GHz, and a RAM of 128 GB. The developed tool was executed in a common computer, a MacBook Pro with the processor Intel Core i7 2.6 GHz and 16 GB of memory. Table 4.3 is possible to see that the developed tool with the method L_{4Coils} spent always less time to compute the inductance value, even in the set **AA** where the coils have about a thousand points. For the case of the set **BB**, the difference in time spent by the proposed tool in relation to FEM simulations is drastically less, more than 20 times.

Table 4.3: Absolute relative Error between the FEM Model results of the Simulation **A** and the developed tool results of the sets of coils **AA** and **BB**.

	Developed Tool				**FEM Model**
	Set AA		**Set BB**		
	L_{4coils}	L_{2pairs}	L_{4coils}	L_{2pairs}	
Inner Coil	$4min$	$7min$	$7seg$	$10seg$	$5min$
Outer Coil	$4min$	$9min$	$13seg$	$19seg$	$5min$

Taking into account the conclusions taken in the previous sub-sections, Table 4.4 has the errors between the FEM Model results of the Simulation **A** (that corresponds to the one with an air-box with a 6 mm offset from the coils, and with no refinement of the mesh) and the several approaches tested with the developed tool. Despite the set **AA** having more points in the geometry of the coils than in set **BB**, this last presents lower errors when compared with the FEM results.

Table 4.4: Absolute relative Error between the FEM Model results of the Simulation **A** and the developed tool results of the sets of coils **AA** and **BB**.

	Set AA		**Set BB**	
	L_{4coils}	L_{2pairs}	L_{4coils}	L_{2pairs}
Inner Coil	4.306%	3.531%	0.857%	0.002%
Outer Coil	11.115%	10.465%	8.446%	7.739%

Analyzing the errors between L_{4Coils} and L_{2pairs}, it can be seen that they are similar to each other. However the method L_{2pairs} is the simplest, and therefore the one that presents lower errors, so it can be concluded that this is the best approach to select.

4.3 Angular Position Sensor Design and Validation

This section describes how the angular position sensor design was validated through the developed analytical model, FEM models and experimentally. It explores the results obtained by a complete and approximate FEM model, comparing these results with those obtained by the analytical model developed. The comparison of the experimental measurements with the results of both tools was also performed. Thus, it was possible to identify the potential of the tool developed in relation to the one usually used (FEM).

4.3.1 Angular Position Sensor Design validation by the proposed analytical model and FEM

During the development of the Differential Coils APS two layers of GND were placed under the coils, to make the sensor less sensitive to external magnetic fields interference. In order to validate, using experimental measurements the FEM model and the developed tool, it is necessary to introduce, in both models, these two GND planes that the sensor has. After, the inductance calculation can be made, in each model, of one pair of inner coils and one pair of outer coils with these GND planes. As the sensor is composed by 3 identical pairs of inner and outer coils, it is just necessary to simulate one pair of each coil (one inner coil pair and one outer coil pair) to be able to have the output of the sensor. As FEM simulations are very time consuming to perform this validation, the research team decided not to simulate the pair of coils. Instead of that, just one inner and outer coils were simulated, multiplying by two the inductance obtained for each one, in order to have the complete inductance of each pair, thus neglecting the mutual inductance between the coils. The error introduced should not be very large, due to low number of turns of the coils. Figure 4.13 shows the FEM model simulated by them, having obtained the inductance values of 414.82 nH for the inner coil and 578.86 nH for the outer coil. Multiplying by two, they estimated that the inductance of the inner coil is equal to 829.63 nH and the outer coil to 1157.72 nH.

In order to understand the error that was obtained with this approximation, a FEM model for each pair of coils was developed, depicted in Figure 4.14. Using the same current, air-box and mesh configurations as the FEM approximated model, it was obtained an inductance value for the inner coil of 857.67 nH and for the outer coil of 1197.09 nH. Thus, it can be concluded that the approximation that was made added about 3.3% of error to the model. Comparing Figures 4.13 and 4.14, it is visible that in the first one, to obtain the inductances of the inner and outer coils, only one inner and one outer coil is used, and that in the second two simulations are performed for each pair. Taking into account what is described in Section 4.1, the geometry of the coils makes its magnetic field concentrate at its center, practically not interfering

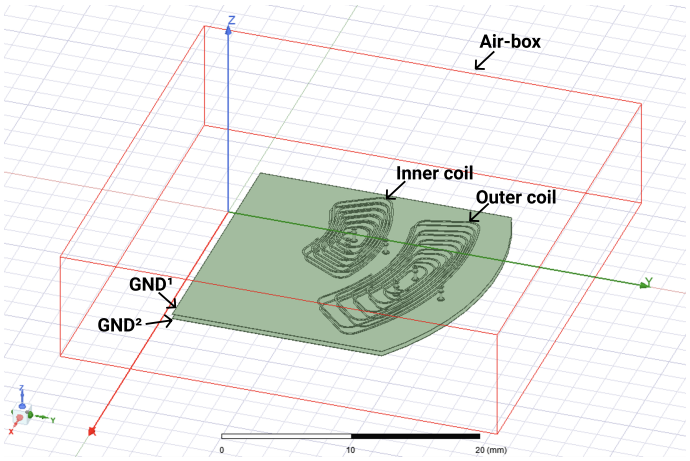

Figure 4.13: FEM model simulated by the research team of the laboratory for validating the inductance values of the pairs of coils of the APS.

with the surrounding coils. However, in order to quantify this interference a new FEM model was made, where in one simulation both inner and outer coil pairs were joined. In the case of the inner coil pair, an inductance of 855.25 nH was obtained and in the case of the outer 1189.19 nH.

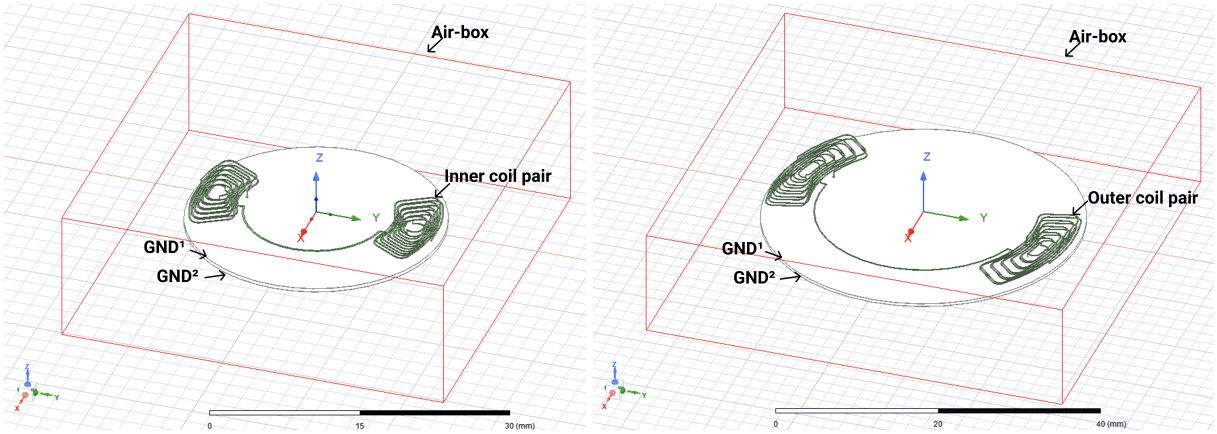

Figure 4.14: FEM model simulated by the author for validating the inductance values of the pairs of coils of the APS.

In what concerns the developed tool, to implement the GND layers in the model, the approximation done for a conductive plate moving over or under the coils presented in Section 3.3 was used. In this way, the GND layer is treated as a one-turn coil, where its inner filament corresponds to the average position of the coil area. As can be seen in Figure 4.15, the internal and external edges of the coil are indicated in black, and in red the average position between the edges, which corresponds to the filament representing the GND layer. For the width of this filament, the distance between it and the coil's outer edge plus twice the value of the wire's width of the coil will be considered. Thus, using these configurations in the proposed model, the inductance values obtained for both inner and outer pair of coils of 791.56 nH and 1188.33 nH, respectively.

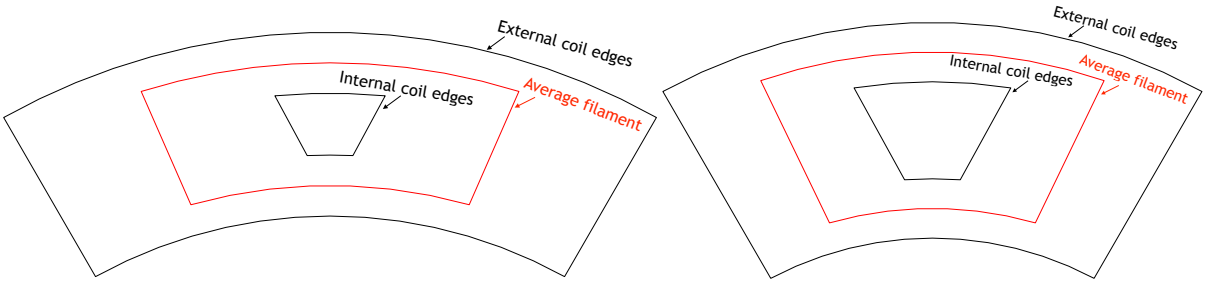

Figure 4.15: GND filament geometry considered in the developed tool (in red). In black the lines representing the internal and external edges of each coil, in red the average position between the edges.

As in the case of FEM models, also in the developed tool, a model was implemented with both pairs of coils and respective connectors and ground planes (visible in Figure 4.16), in order to validate the concept of low interference between adjacent coils. An inductance of 791.56 nH was obtained for the case of the inner pair of coils, and of 1188.33 nH for the outer pair. The results obtained by the model integrating both pairs of coils (inner and outer) or considering them separately was exactly the same. Thus, it can be concluded that the sensor's coils have a low influence between adjacent coils, in the same way as the error obtained by the FEM model. However, the model that calculates individually the inductance for each pair of coils is faster to compute than the one that integrates both pairs of coils. The first one takes 2 minutes and 40 seconds to calculate the inductance of the inner pair and 3 minutes and 45 seconds of the outer pair, and the second takes 7 minutes and 12 seconds for both inductances. This happens because it is not necessary to do so many mutual inductance calculations (in the first case), due to the smaller amount of filaments that is considered (less one pair of coils and less two mass planes). Thus, considering the non-existent error between both approaches and the time that they take to calculate the inductance, it is recommended to use the model that individually calculates the inductance of each pair of coils, since it is the simplest and fastest.

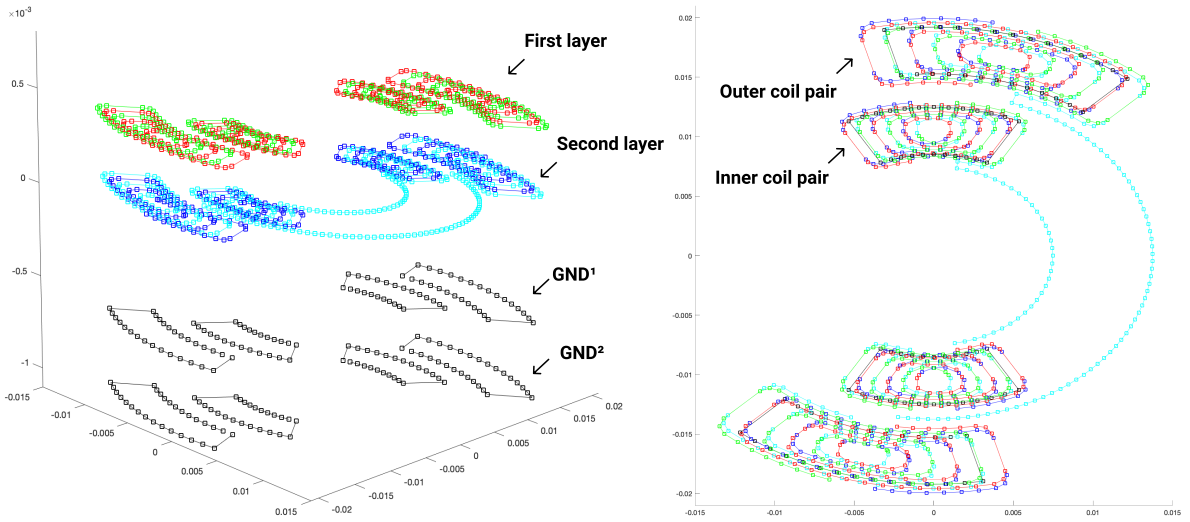

Figure 4.16: Filaments for an inner pair coil, an outer pair coil and respective GND planes, considered by the developed tool.

4.3.2 Angular Position Sensor Design Experimental Validation

Regarding to the experimental measurements, the same measurement setup was used (the one presented in Section 3.4). In Figure 4.17 depicts the PCB that was used to measure the pairs of inner and outer coils, and the setup of measurement.

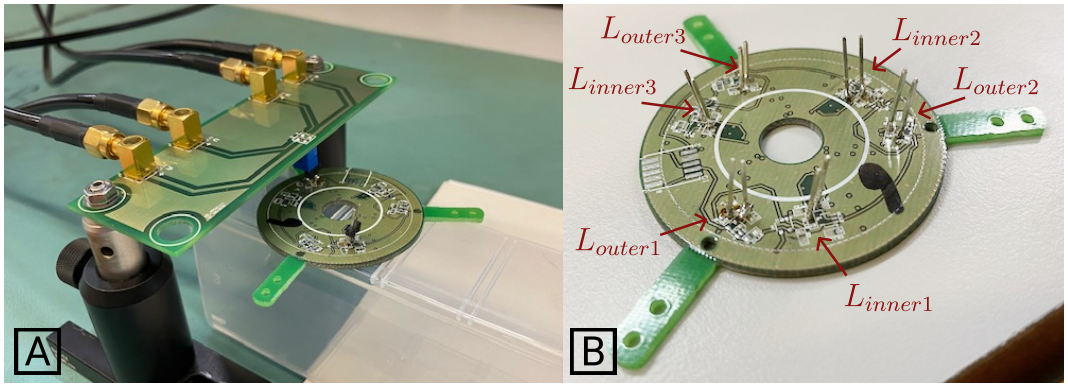

Figure 4.17: A: Setup of measurement. B: PCB with the coils from the APS.

Table 4.5 presents all the values measured, being evident the high concordance between all of the measurements. It can be traduced in a standard deviation of 0.053% for the case of the inner pair of coils, and around 0.040% for the outer pair. By averaging the measurements of the two pairs of inner (L_{inner1} and L_{inner2}) and outer coils (L_{outer1} and L_{outer2}), the inductance values of 888.66 nH and 1218.18 nH are obtained, respectively.

Table 4.5: Inductance values measured experimentally for two pairs of inner (L_{inner1} (nH) and L_{inner2}) and outer (L_{outer1} (nH) and L_{outer2}) coils.

Inner Coil Pair		**Outer Coil Pair**	
L_{inner1} (nH)	L_{inner2} (nH)	L_{outer1} (nH)	L_{outer2} (nH)
889.22	888.44	1215.2	1220.9
888.81	887.80	1214.3	1220.9
889.05	888.89	1214.9	1221.3
888.96	888.78	1215.3	1221.7
888.91	888.35	1215.2	1221.3
889.27	889.43	1215.7	1221.6
888.57	888.99	1213.9	1220.9
887.66	888.28	1214.5	1221.9
889.13	888.32	1214.6	1221.8
888.44	888.31	1215.7	1221.2

Thus, in order to better analyze the performance of the FEM model and the developed model face to the experimental measurements, Table 4.6 presents the relative errors between the mean values measured experimentally for each pair of coils, and the inductance values obtained from both models. Based on the values in the table, it can be concluded that both the FEM approach and the tool developed are quite reliable. In the case of the developed tool, it is perceptable that its results are more accurate in the case of the outer coils. With regard to the time taken by each one of the tools to calculate the inductance value, the developed tool stands out. The FEM Model takes about 13 minutes for the inner coils and 23 minuntes for the outer coils, which is 4.89 times slower than the proposed tool for the inner coils, and 6.13 times for the outer coils.

Table 4.6: Absolute relative Error of the FEM Models, the developed tool in relation to the experimental measurements

	Developed	**FEM Model**	
	Tool	Approx. one Coil	Pair of coils
Inner Coil	10.93%	6.64%	3.49%
Outer Coil	2.45%	4.96%	1.73%

4.4 Angular Position Sensor's Response Validation

This section describes the validation of the angular position sensor response. To the FEM and developed analytical models, presented in Section 4.3, a rotating target was added over the coils. Since the analytical developed model presents an approximation to the target geometry (for a single-turn coil), the results obtained by this model are compared with the FEM model. This way, it is possible to perceive the impact of this approximation, since in the previous section both models present similar results. The results of both tools are also compared with the experimental results.

4.4.1 Angular Position Sensor's Response Validation by the Proposed Model and by FEM

With the models of the sensor (FEM and developed tool) considering its coils and GND layers validated, follows its validation by integrating a moving target over the coils. This target is fixed to the axis of rotation, and its movement changes the induced eddy currents, which in turn changes the value of the inductance of the coils.

Figure 4.18 shows the FEM model implemented to analyze the response of the sensor's coils in the presence of two ground planes and a target with four parts rotating over them. The target was positioned at 1 mm of a distance from the upper coils. The same current, air-box dimensions, and mesh configurations of the previous simulations were used. To have the complete sensor response for each pair of coils, simulations rotating the target from 0° to 90°, with a step of 0.5°, were performed.

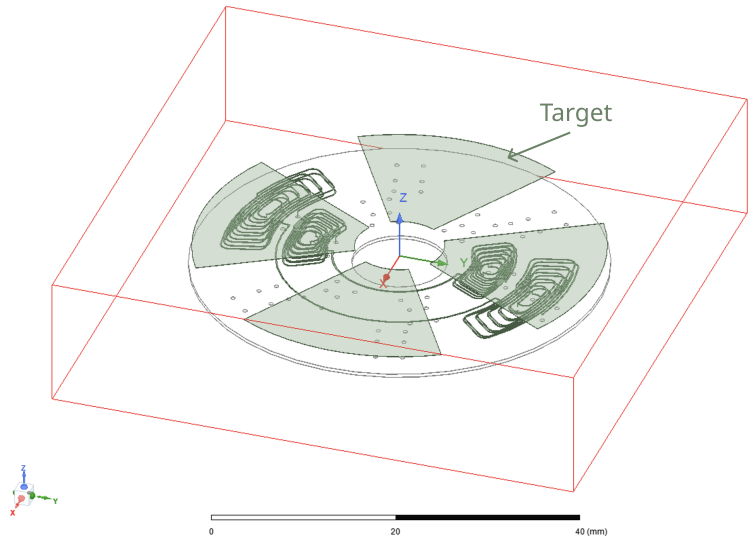

Figure 4.18: FEM model of both inner and outer pair of coils, in the presence of four targets and two ground planes.

In the same way as in FEM, the target was integrated into the sensor model implemented in the developed tool. Previously, each one of the GND layers was approximated to a one-turn coil having considered a correction factor of 30% (Equation 3.5) in its inductance influence. This was because the generated currents are distributed beyond the external dimensions of the coils. Comparing A_0 and A_1 in Figure 4.19, this effect is noticeable. Also, analyzing Figure 4.19, specifically B_0 and B_1, it is clear that the currents are not distributed over such a vast area, being limited by the target dimensions. Therefore, the compensation factor was not used in the case of the targets.

As mentioned before, due to calculation time optimization and model simplification, each pair of coils are analyzed separately. Thus, the four components of the target are integrated in each one of the models, 1 mm apart from the upper layer of the coils, and they are rotated from 0° to 90°, with a step of 0.5°. Figure 4.20 shows the filaments used by the developed tool to calculate the inductance resultant in each pair of coils. The inner filaments used to represent each of the target parts are signed in green, and in light blue and red those used to represent the GND layers.

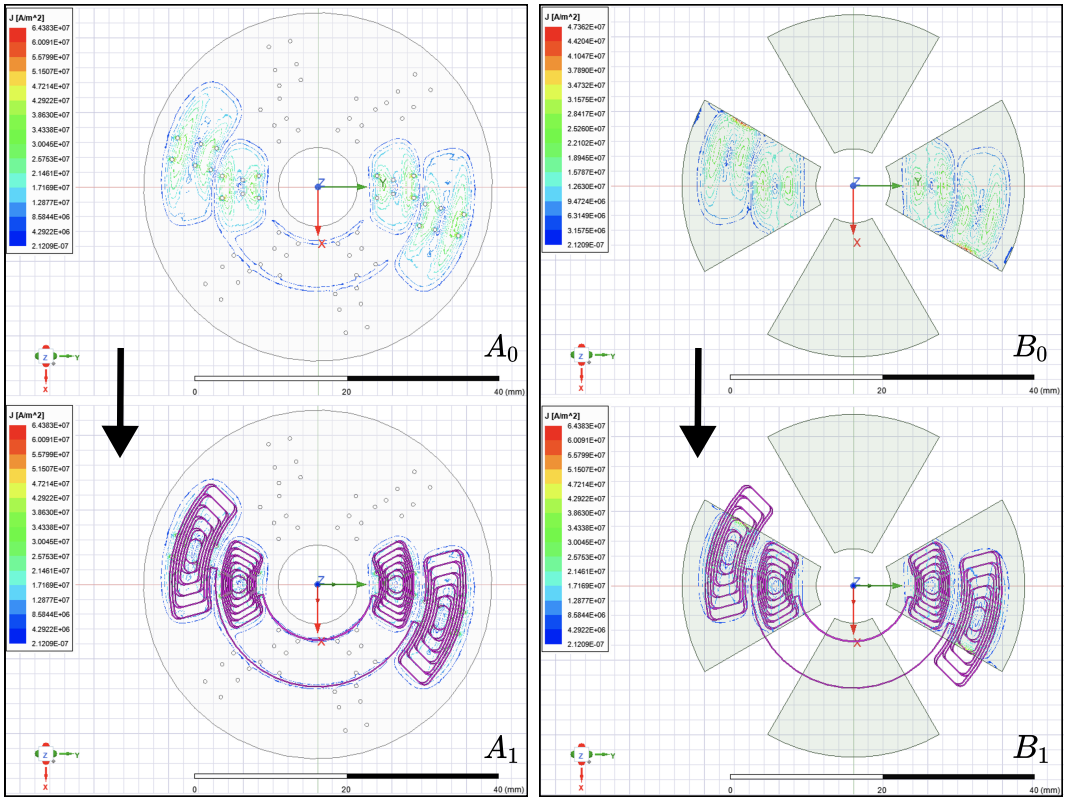

Figure 4.19: Eddy current distribution in the GND (A_0: coils hidden and A_1: coils visible), and in the targets (B_0: coils hidden and B_1: coils visible).

With both approaches, FEM and proposed tool, analysing the same sensor components under the same conditions, it is possible to compare their inductance results and time spent to obtain them. Considering the FEM simulations as the most accurate approach, the graphic visible in Figure 4.21 shows the error modulus of the inductance values obtained by the developed tool in relation to those of the FEM, during the target rotation (0° to 90°). In blue is represented the error obtained in the case of the inner pair of coils, and in orange of the outer pair. It is visible that in both coil cases the errors are quite below the stipulated maximum error limit of 10%. In the case of the inner pair, the higher error registered was 6.6%, and in the outer pair was 6.7%. This happens when the target is at 0° and 90° positions, which is when the target is overlapping the coil completely. The average error obtained during the full target's rotation is 4.46% for the inner coils, and 3.81% for the outer coils. Thus, it can be concluded that the

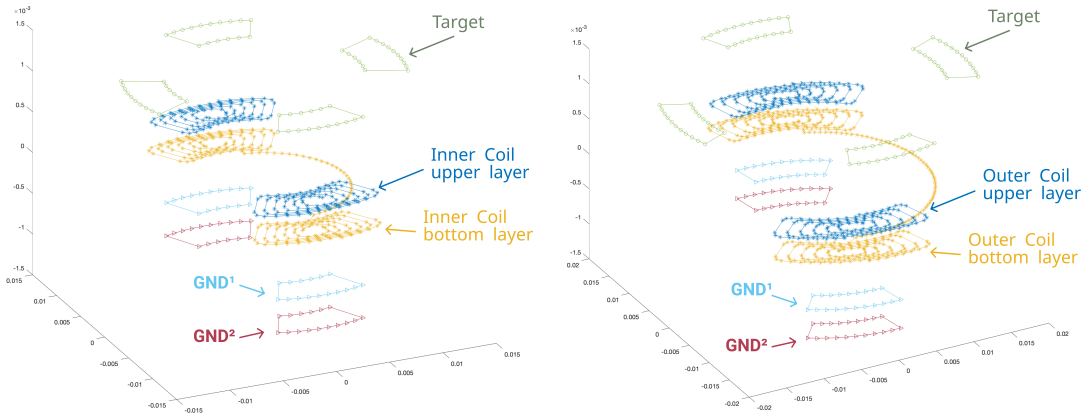

Figure 4.20: Filaments used by the developed tool to calculate the inductance resultant in the inner and outer pair of coils, in the presence of four targets and two ground planes.

developed tool has a good accuracy, when compared with the FEM simulator, to to calculate the response of a sensor with planar coils in the presence of several targets and mass planes.

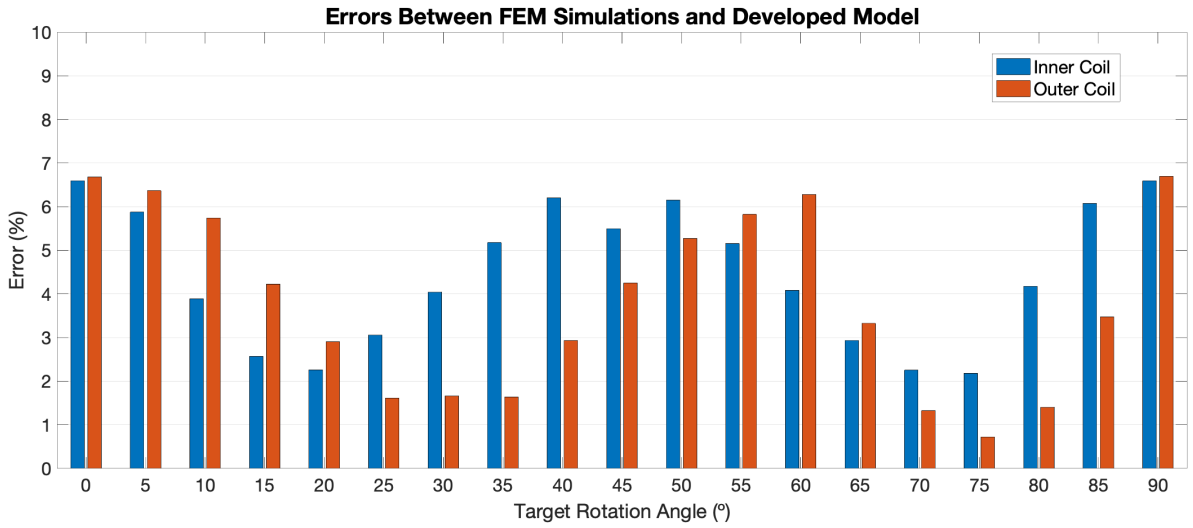

Figure 4.21: Errors between the FEM simulations and the developed model of both inner and outer pair of coils, in the presence of a rotating target and two ground planes.

In this particular case, the developed tool took 1 minutes and 31 seconds to calculate the resultant inductance for the inner coils, and 3 minutes and 38 seconds for the outer. In the other hand, the FEM simulations took over 12 hours to achieve similar results. Thus, the developed tool is 144 times fastest than the FEM.

4.4.2 Experimental Validation of Angular Position Sensor Response

After the sensor's response validation by FEM simulations and the developed tool, described in Subsection 4.4.1, follows an experimental validation of the results was carried out. The testing setup used is depicted

in Figure 4.22. This setup includes two motorized actuators, one linear (Thorlabs LTS300/M) and another angular (Thorlabs NR360S/M). They are responsible for positioning the target at the intended position (distance and angle) in relation to the sensor coils. To control these actuators, the Thorlabs BSC201 controller was used. To perform the inductance measurement readings, a LCR meter (Keysight E4980AL) was used (at 1 MHz), similar to the previous experimental tests.

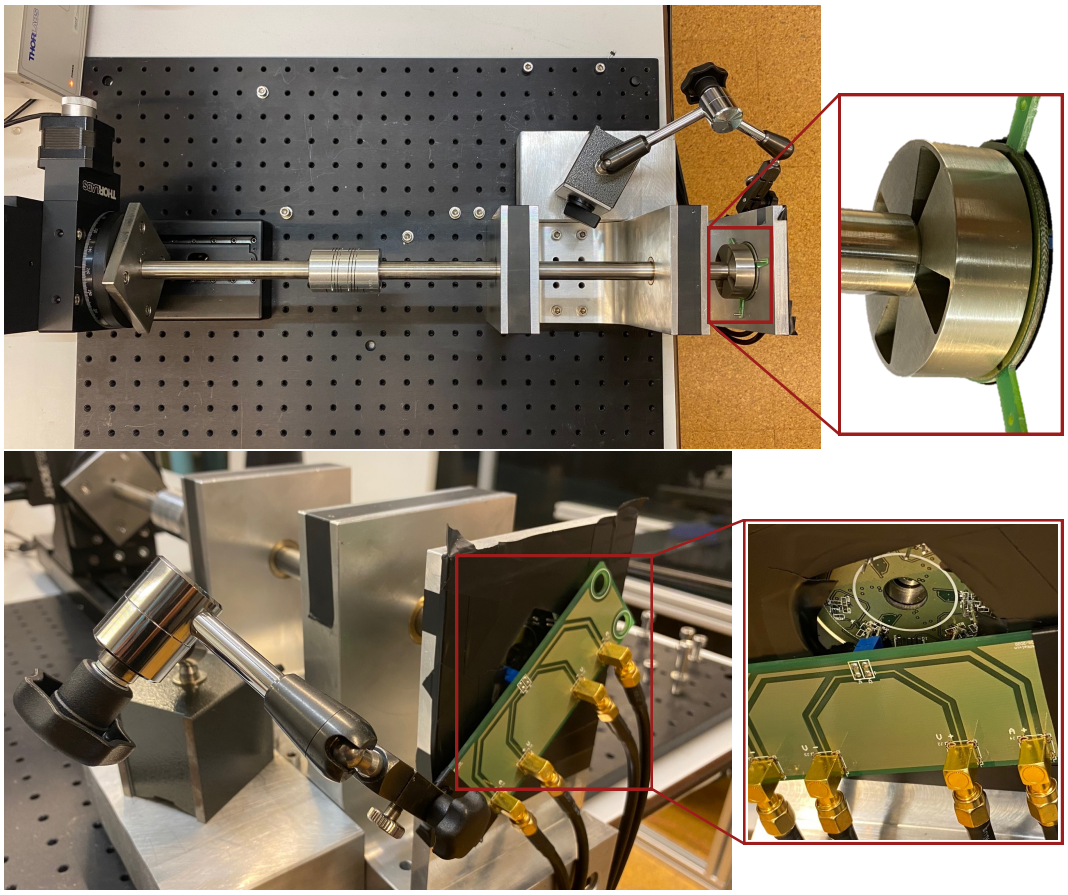

Figure 4.22: Sensor's setup measurement.

As the setup was configured in the same conditions as in the sensor's response validation by the proposed model and FEM (Subsection 4.4.1), the target was positioned at a distance of 1 mm from the APS sensor. The inductance readings were done at each $0.1°$ rotation of the target, from $0°$ to $360°$. It was considered full rotation range, and not just $90°$ as before, to mitigate possible asymmetries that derive from the manufacturing tolerances of the sensor PCB but also from the setup and target mechanics (tilt, offset, etc.). In order to have the most correct measurement, for each position 100 samples were obtained from the LCR meter, and the median was calculated from these. In addition, two sets of these measurements were done for an inner and the outer pair of coils. Figure 4.23 shows the frequency distribution of 100 samples collected when the target is in position $0°$ for a pair of inner and outer coils. It is visible how much the precision of the measurement setup is enhanced, in accordance with what was previously

mentioned. The maximum deviation of measurements for the inner pair is 0.016 nH (0.0019%) and 0.04 nH (0.0034%) for the outer pair.

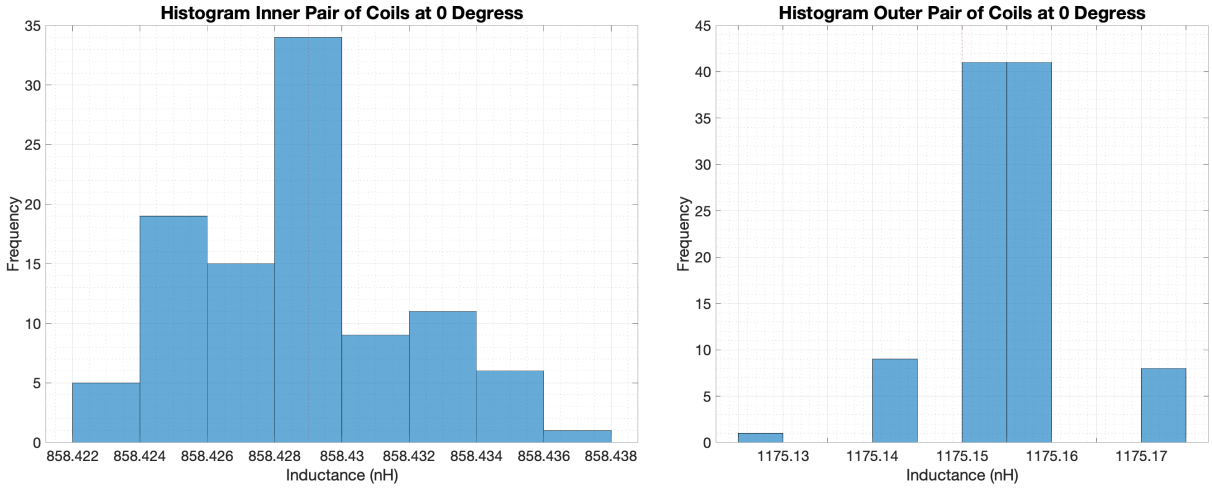

Figure 4.23: Histogram of 100 samples collected when the target is in position 0° for a pair of inner and outer coils.

Figures 4.24 and 4.25 show the results of the measurements for the rotation of the target from 0° to 360°. In A_i and A_o is visible the wave signal resultant from the rotation of the target from 0° to 360°, and in B_i and B_o it is overlapped the four periods of 90° that exists in the full rotation.

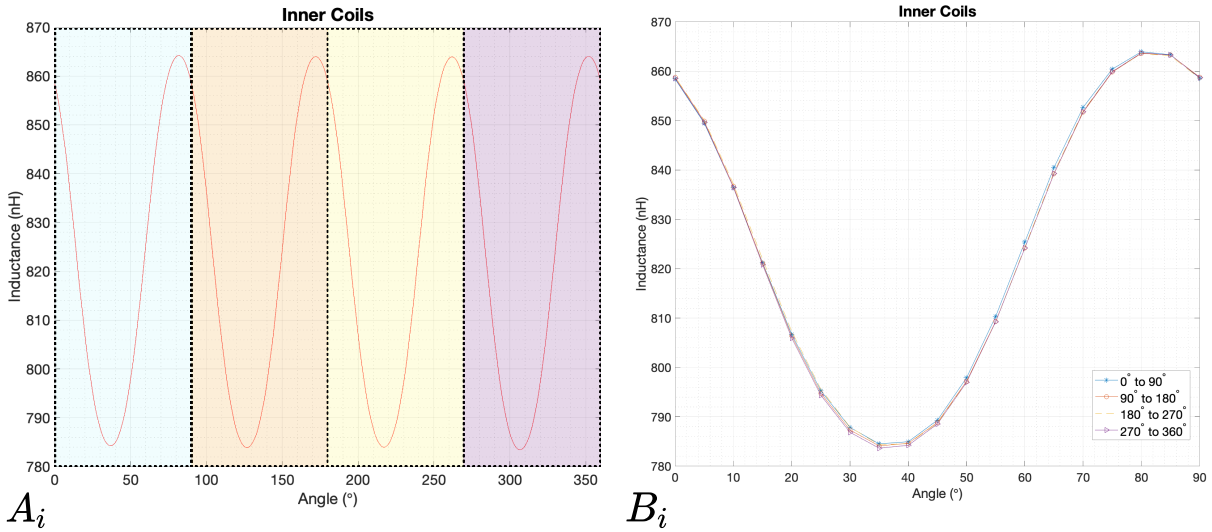

Figure 4.24: [Results of the measured inductance values of an inner pair of coils.

It is possible to see, specially in B_i and B_o, that the peaks does not have exactly the same value and that the wave shape has some deviations. In addition to production and mechanical tolerances, these differences may be due to the detected tilt of the target. This has a value of 0.187°, and is reflected in the distance between it and the sensor, ranging from 1 mm to 0.85 mm.

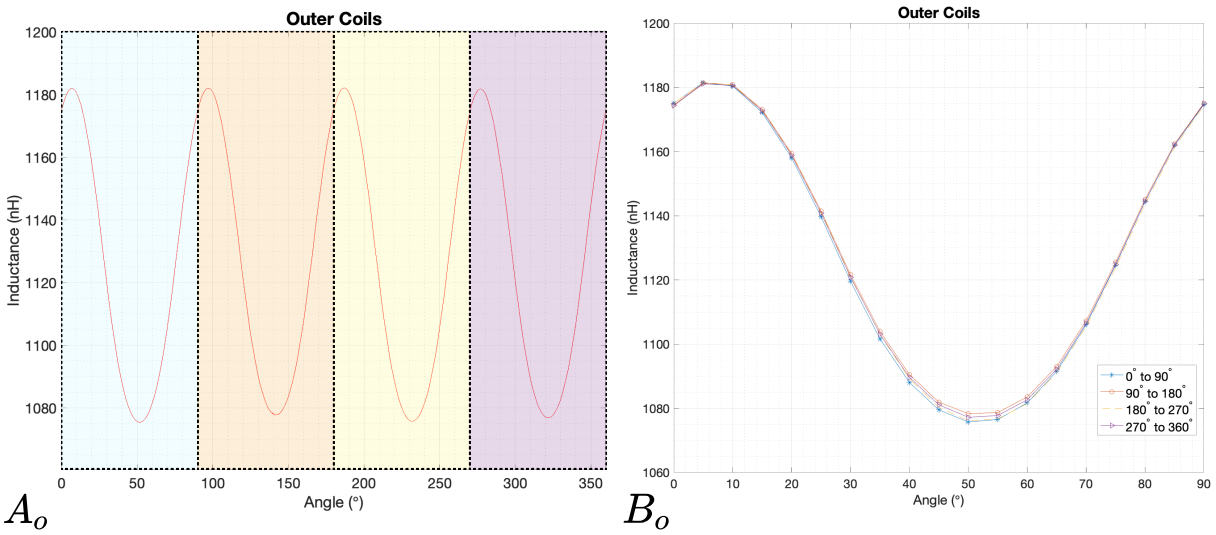

Figure 4.25: [Results of the measured inductance values of an outer pair of coils.

4.4.3 Comparison between the Proposed Tool, FEM Simulations and Experimental Measurements

After obtaining the inductance values of the sensor coils via experimental measurements, FEM simulation and developed model, the analyzis of these data follows. The resultant value of the median, for each position, of the two groups of measurements performed for each pair of coils was used to have the most accurate experimental value. Figures 4.26 and 4.27 show the errors between those inductance values with the ones got from the developed model and FEM simulations. It is visible that for the case of internal coils, the errors between the experimental values and the proposed model are higher than when compared to the FEM model. The average error for a $90°$ target rotation in the developed model is 8.38%, and in the case of the FEM is 4.10%. However, the same does not happen in the case of external coils. In this case, an average error of 2.09% for the proposed model and of 3.55% for the FEM.

As mentioned in Section 4.3, for approval of the design of the sensor coils, an approximate FEM simulation was used. Only one coil of each pair, a quarter of the mass planes, and only two target components were simulated, as the time factor is critical during the design phase. Comparing the values obtained by these simulations with those measured experimentally, it is verified that the average error they present for both inner and outer coils is around 6.5%. In turn, comparing the performance of this approximate FEM model with the developed analytical model, it can be seen that the proposed model meets the needs of the research and validation teams. In the case of the inner coils, the proposed model has an average error higher than the one from the approximate FEM model in 1.86%, and in the case of outer coils, it has an inferior average error of 4.37%. In addition to these results, the proposed model also has the

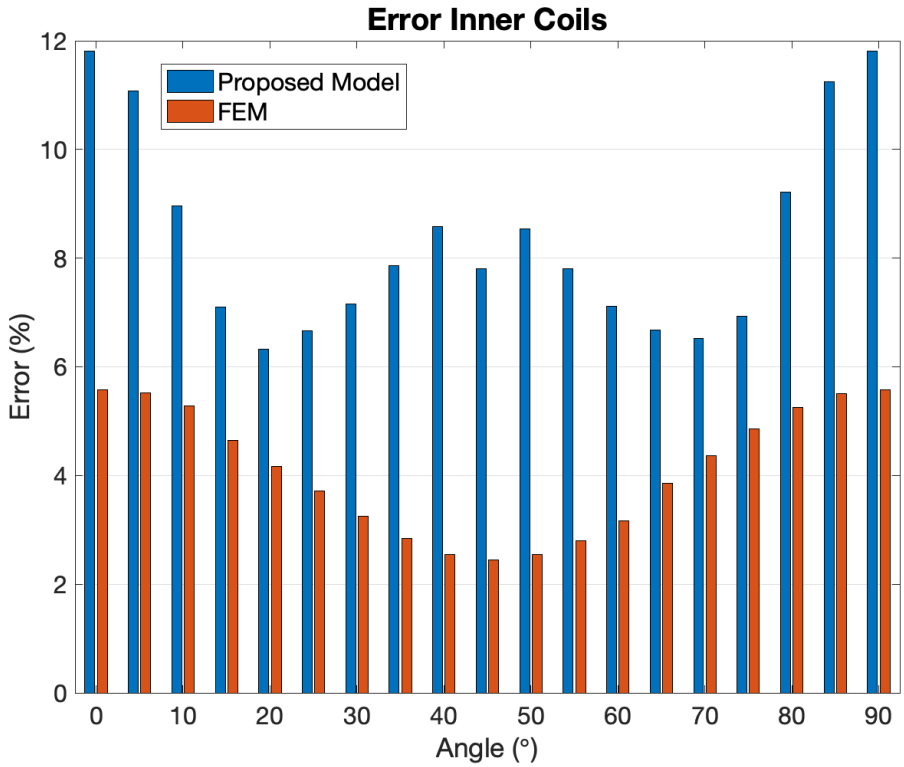

Figure 4.26: Module of the error between the experimental inductance values and the proposed model (at blue) and the FEM simulation (at orange), for the inner coils case.

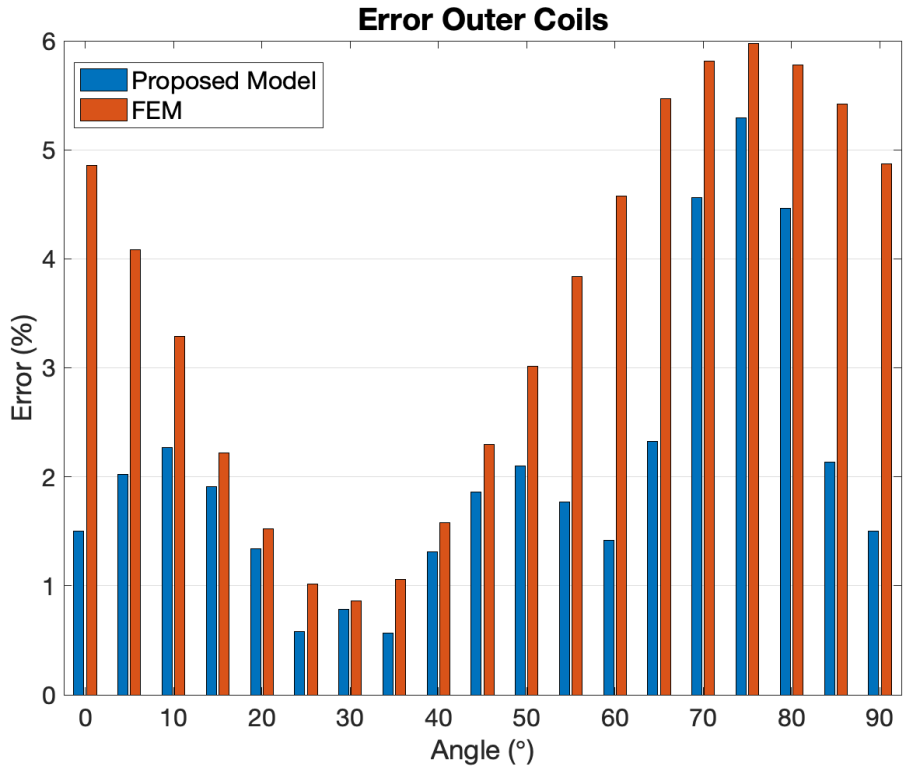

Figure 4.27: Module of the error between the experimental inductance values and the proposed model (at blue) and the FEM simulation (at orange), for the outer coils case.

advantages of requiring less computational resources, requiring lower cost software and taking less time to obtain the sensor inductance.

4.5 Angular Position Sensor Full Electrical Simulation

After the implementation and simulation of the value of the inductances of the sensor coils, the analysis and validation of the sensor output follows. To this end, a simulation model of the oscillator circuit was implemented (Section 4.1), using the MATLAB Simulink® software. Figure 4.28 shows the oscillator circuit implemented for a pair of an inner and an outer coils, with a D-type flip-flop. This flip-flop, as mentioned previously, is responsible for subtracting the frequency signal from both pair of coils, in order to have the differential measurement. The **L0** and **L1** represent the coils printed on the PCB, an inner pair and an outer pair. **C0** and **C1** allow the adjustment of the operational frequency of the oscillators for the inner pair of coils, being configured with the same value. The pair of capacitors **C2**, **C3** follows the same configuration pattern, but related to the outer pair of coils. The values of **R0** and **R1** are chosen to limit the current when **C0** and **C3**, respectively, are discharged. The 'Voltage Sensor' block is responsible for converting the electrical-signal type to a physical-signal type. Then, this signal is converted to a logical type by the comparison block (where the value 2.3 is the flip-flop voltage threshold), as this is the only type that the flip flop accepts. The differential output is then converted to a double type (**flip-flop**).

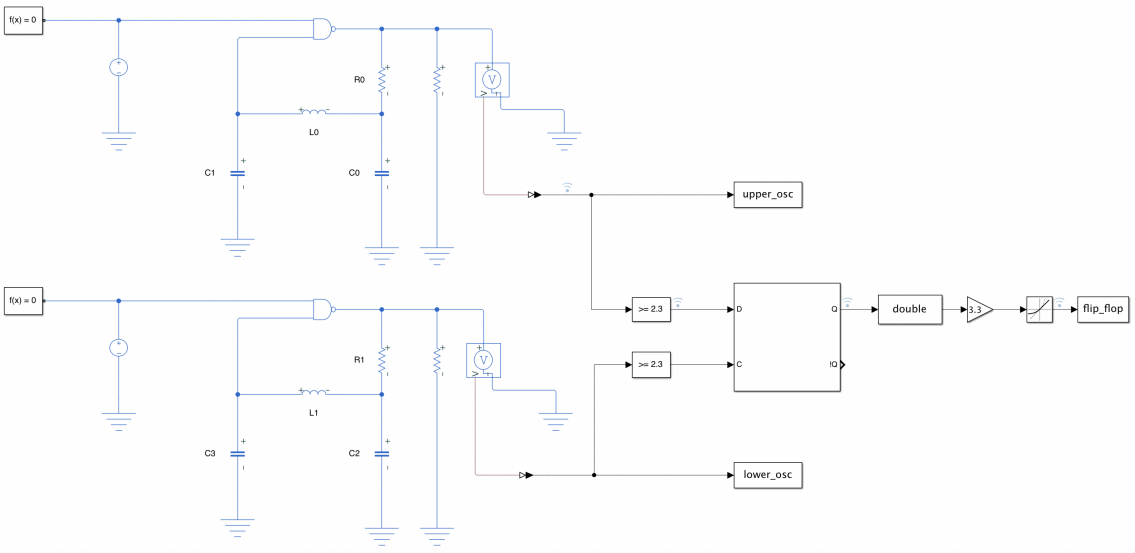

Figure 4.28: MATLAB Simulink® circuit representation of an oscillator and a Flip-flop 'D' block, to simulate the sensor's differential signal.

The selected sensor contains six pairs of differential coils tuned to different frequencies so that there is no locking between them. With the application of the flip-flop, only three output signals are produced. These

signals are frequency modulated, with a 120-degree phase difference.

To evaluate the behavior of the sensor, in the case of experimental measurements and values calculated by the developed analytical model, two simulations of the oscillator circuit were performed with each of these values. Figures 4.29, 4.30 and 4.31 show the frequency values generated for each oscillator circuit in red and blue for both cases.

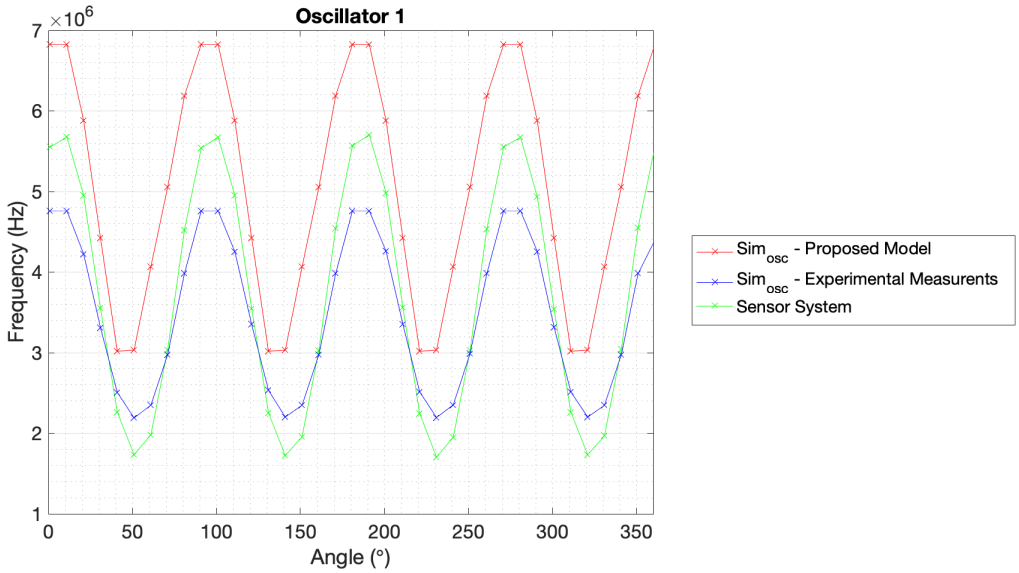

Figure 4.29: Frequency sensor's differential signal of oscillator 1.

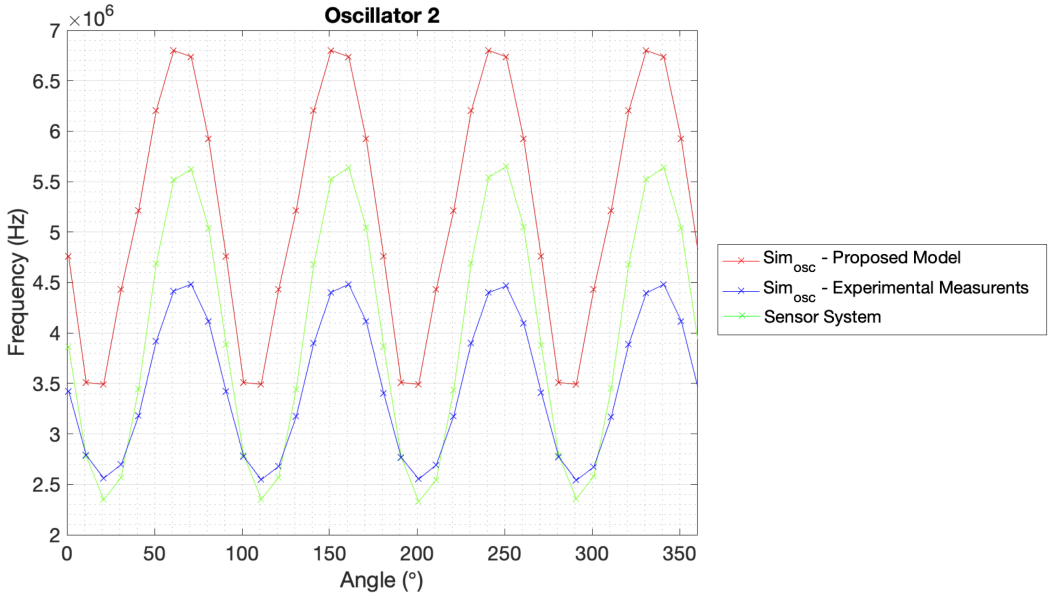

Figure 4.30: Frequency sensor's differential signal of oscillator 2.

In order to validate the oscillator circuit simulator, the data measured experimentally with the sensor system developed [4.4] was used. Thus, it was possible to perform an evaluation of the behavior for the

two cases simulated in the oscillator circuit. Figures 4.29, 4.30 and 4.31 show at green the signal in frequency referring to data measured with the sensor system for the three oscillators.

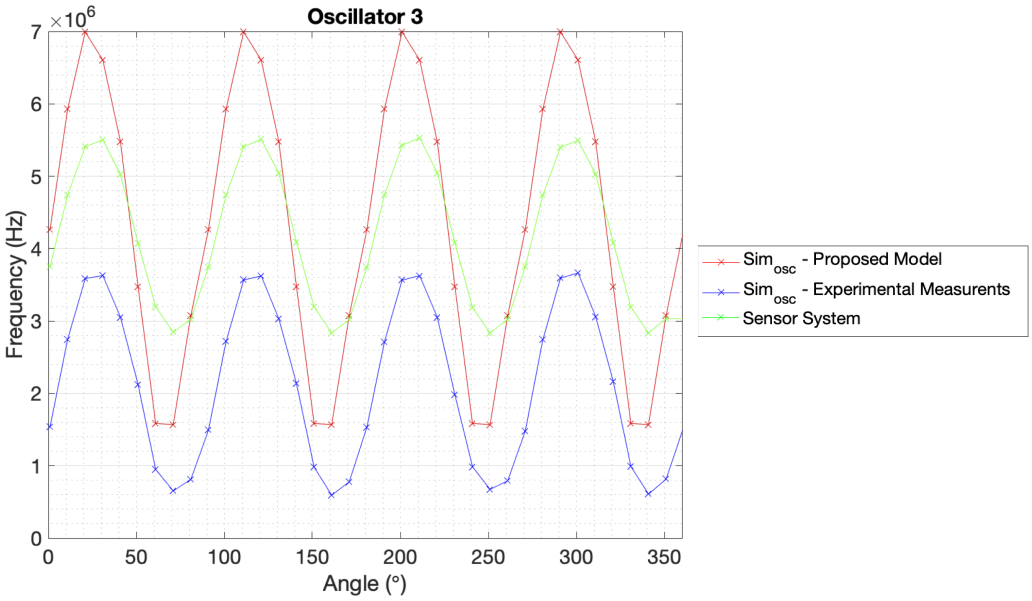

Figure 4.31: Frequency sensor's differential signal of oscillator 3.

By comparing the various signals, it can be seen that there are some discrepancies between the simulated signals and the measured signal. These differences happen due to several factors. One is because the sensor's oscillator circuits work between 20 MHz and 40 MHz. Taking into account that the LCR used perform the measuremts at 1 MHz, when introducing these data into the oscillator circuit simulator, it is expected that there will be discrepancies. The oscillator circuit simulator itself is a mere approximation, thus also introducing errors in the results. Finally, the tolerances existing in the components are factors that also contribute to the differences in the observed values.

To interpret the three output signals and extract the angular position of the target, a signal conditioning must be done first. As oscillators have different resonant frequencies, they do not form a perfect three-phased system. To do so, the average value must be removed from each signal and equalize all amplitudes, before applying the Clarke Transform. After the normalization of the signals, the Clarke transformation is applied. The Clarke transformation is a mathematical transformation to achieve a simplified 2-axis stationary reference frame for the analysis of three-phase circuits. So, with basic trigonometry functions, the angular information can be calculated from the product of the Clarke transform. In Figure 4.32 is visible the sensor's output for a target rotation from 0° to 360°, by the two cases simulated in the oscillator circuit and by the sensor's system.

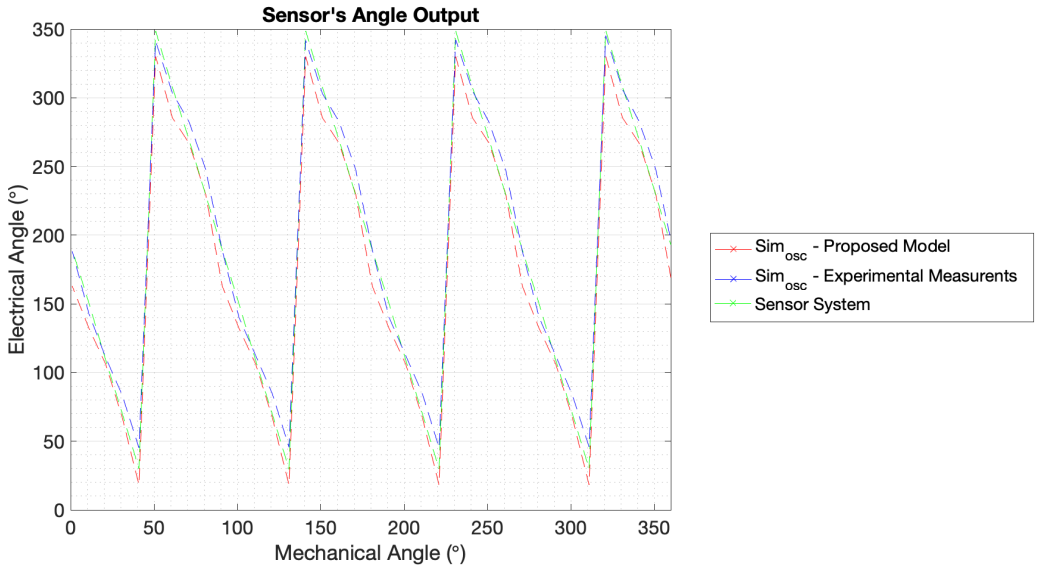

Figure 4.32: Sensor's angle output.

Figure 4.32 highlights that the angles obtained by the oscillator circuit simulator have some nonlinearities. This is because the oscillator signals are not perfect sine waves. Thus, the harmonics they present are reflected in the calculation of the Clarke transformation and the arctangent that computes the angle. To attenuate these limitations, the sine waves of the oscillators were constructed from the simulation data. Figures 4.33 and 4.34 show the signals from each oscillator approximated to a sinusoid and the respective points generated by the oscillator simulation. The data in Figure 4.34 are related to the oscillator circuit with data measured experimentally and those in Figure 4.33 with those calculated by the developed model.

With the sinusoidal signals of each oscillator generated, the normalization and also the application of the Clarke transform follows (as performed previously for the calculation of the respective sensor angles). Figure 4.35 shows the sensor's output for a target rotation from $0°$ to $360°$ by the sensor's system (in green) and by the two cases simulated in the oscillator circuit that were approximated to a sinusoidal wave. In red is the case that is based on the proposed model data and in blue the one that is based on the experimentally measured data.

Comparing Figures 4.32 with 4.35, the signals obtained by the oscillator circuit simulator present a significant reduction in nonlinearities. The three signs practically overlap. To quantify the errors between the angles obtained by the sensor system and the oscillator simulator, their wave signals were subtracted. Figure 4.36 shows the error modulus graph of the simulated oscillator angles versus the sensor system. It is visible that the errors of the simulated oscillator circuit are less than $2.5°$, for both cases (data from

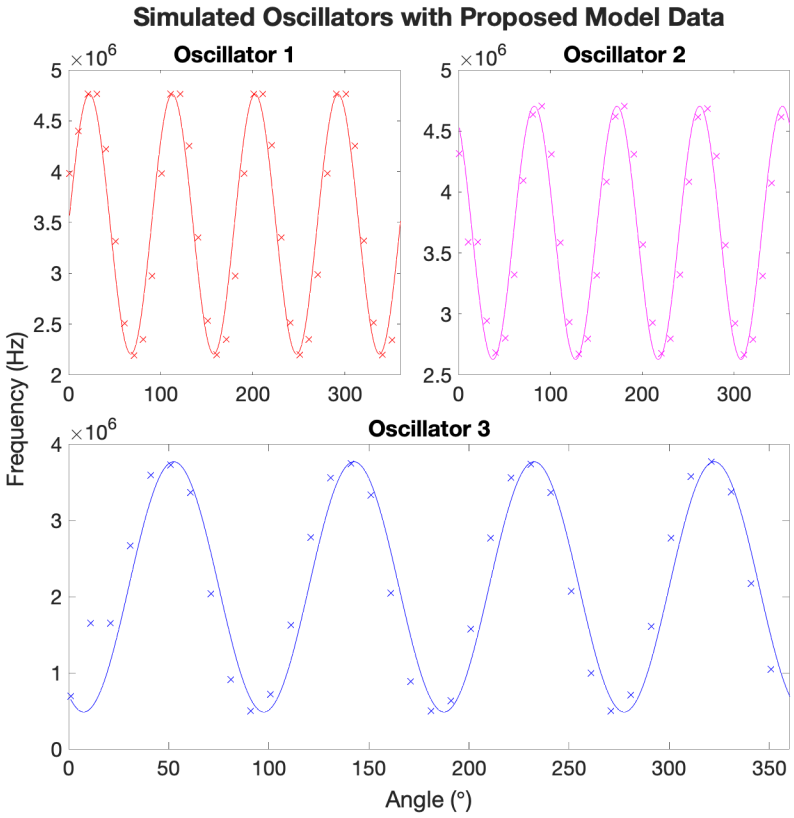

Figure 4.33: Simulated oscillators with proposed model data.

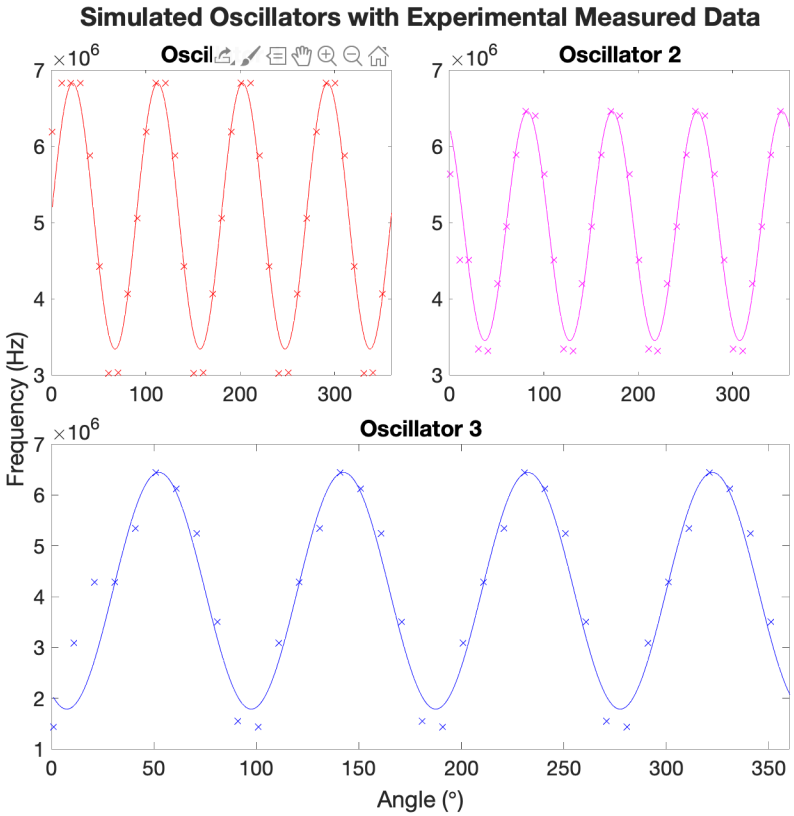

Figure 4.34: Simulated oscillators with experimental measured data.

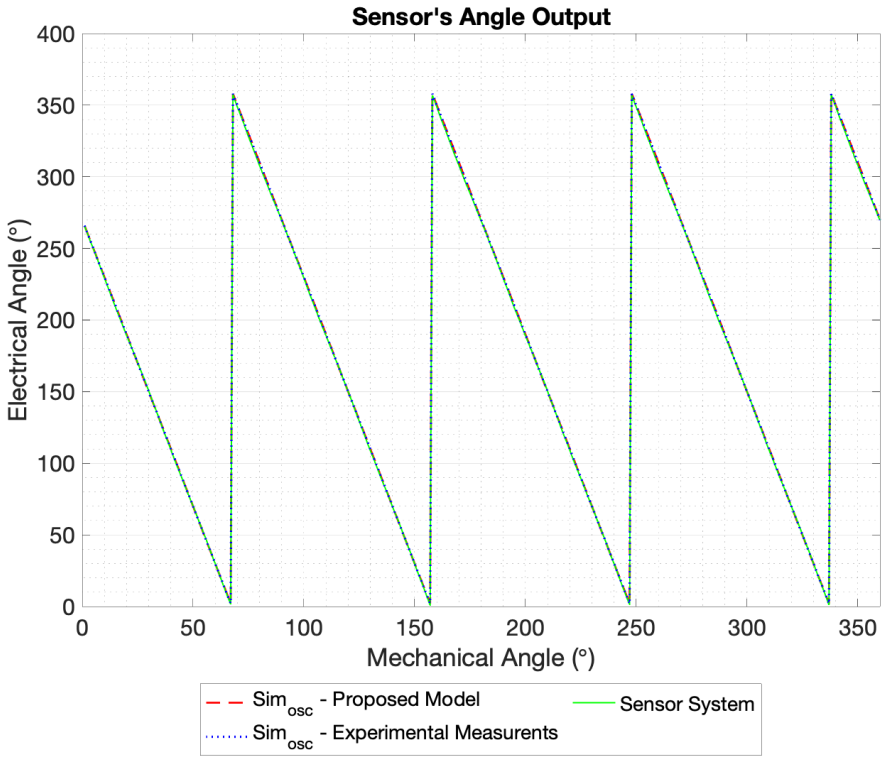

Figure 4.35: Sensor's angle output from the sensor system and the simulated oscillator with sinusoidal approximation.

the proposed model and data from experimental measurements). In view of this, it is possible to confirm the accuracy of the developed model and its versatility, as well as the accuracy of the experimental measurement setup and the simulated oscillator circuit. It is also possible to confirm the versatility of the developed model. Due to the simplicity of its use, it is easy to integrate its results in the simulation model of the sensor response. This results in a faster prediction of the sensor response than is currently obtainable.

4.6 Conclusions

Based on the results and comparing the performances between the methods used in the design phase of an eddy current sensor based with planar coils, several conclusions can be obtained. It can be noted that in addition to the intended resolution during this phase (errors lower than 10% when compared to the experimental results), the time taken to acquire the data is a predominant factor. During the development a simplified FEM model was used to reduce simulation time.

Comparing the average errors in relation to the complete FEM model with those obtained through the developed model, the difference is not significant.

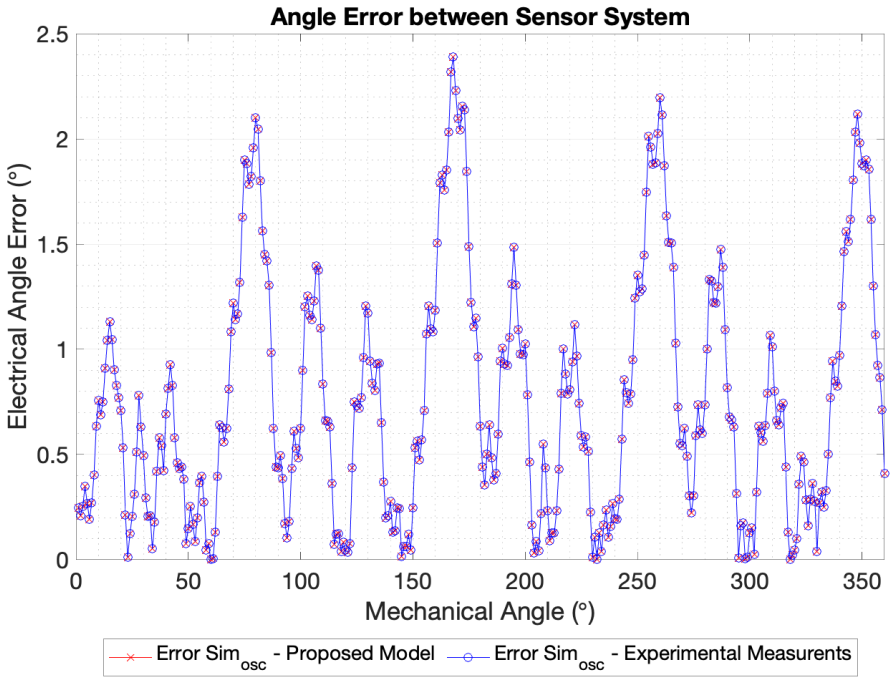

Figure 4.36: Error modulus graph of the simulated oscillator angles versus the sensor system.

With reference to the experimental measurements, the approximate FEM model is better than the proposed model by 1.86% in the case of the inner coil and worse than it by 4.37% in the outer coil. However, despite the small difference in the errors, in terms of the computational resources used and the time spent, the difference is significant. To have the sensor response for a target rotation from $0°$ to $90°$ with a step of $5°$, the approximated model needs 2 hours and 45 minutes (calculating two tasks simultaneously) and the developed model around 5 minutes.Another factor to consider is the difference in software cost, as the cost associated with a multi-core Ansys®license is much higher than a MATLAB®license.

Thus, integrating the results of the developed model in the program that simulates the differential output of the sensor and calculates its angles, it is possible to obtain a similar result to what is obtained by the experimental results. Faster, even using a normal computer, and without the need to use an expensive FEM simulator tool.

References

[4.1] S. Leidich, J. Oberlaender, and O. Krayl, WO2016055348A1: Sensoranordnung zur berührungslosen erfassung von drehwinkeln an einem rotierenden bauteil, 2014. [Online]. Available: `https://patents.google.com/patent/WO2016055348A1/de?oq=WO16055348+A1`.

[4.2] S. Leidich and R. AMELING, WO2016055301A1: Ensemble capteur pour la détection sans contact d'angles de rotation sur un élément en rotation, 2014.

[4.3] H. Aichele, D. Eichel, B. Baffoun, R. AMELING, S. Leidich, J. Strobel, R. Has, and O. Krayl, WO2016055300A1: Sensor arrangement for the contactless detection of rotational angles on a rotating component, 2014.

[4.4] L. M. S. D. d. Vale, "Eddy Currents Based Position Sensor", PhD thesis, University of Minho, 2021.

Chapter 5

Conclusions and Future Work

A novel analytical model for calculating the inductance of planar coils of arbitrary geometry is presented in this thesis. This open-source model is able to calculate the inductance of a multi-layer coil and the resulting change in its inductance when covered by a conductive target. As described in Chapter 1, there is market interest in inductive sensors. The angular sensors market is expanding and particularly in the automotive sector. A state-of-the-art review of the technologies used in angular position sensors was made in Chapter 2. Eddy current sensors, and others, based on planar coils were described and analyzed. In this chapter the analytical expressions commonly used to calculate the inductances of planar coils were also described. Thus, it is possible to identify the advantages and limitations of each analytical approach. Chapter 3 presents the development, implementation, and validation of the proposed analytical model. The validation of the model was done by comparing its results with commonly used analytical expressions (for the cases where they are valid), FEM model simulations, and experimental measurements, using PCB multi-layer coils. Chapter 4 shows the results of applying the model during the development of an automotive APS based on eddy currents. With the application of the tool on a sensor with irregular coils, it was possible to validate the significant advantages of using this tool, namely the execution time and the results precision. In this use case, it was also possible to identify some aspects to improve the proposed model, as the approximation made to the target.

Finally, this chapter summarizes the work developed, its goals, and conclusions. It also presents a proposal to improve the performance of the model for calculating the inductance resulting from a planar coil in the presence of a conductive target.

5.1 Conclusions

During the research work of this thesis, several research topics were addressed, reaching several conclusions. Through the analysis of the sensor market trend, it was possible to identify that there is interest in inductive angular position sensors in the automotive area.

Within angular position sensors, several technologies are used. Following the methodology described in RM1 (introduced on Chapter 1), a state-of-art was carried out focusing on the most used technologies. The strengths and weaknesses of each of the technologies were identified and typical applications for each ones were identified. This way the objective O1 (Review of the state-of-art of the technologies used in angular position sensors, highlighting their strengths and weakness) was achieved and answered partially to the research question RQ4 (Can an eddy current sensor be optimally designed?). Eddy currents was a logical choice for research, as it is a promising candidate for the area of application, the automotive industry, and the author's previous research experience with the technology. In addition, the research fields falls within the partnership between the University of Minho and the Bosch Car Multimedia, in which, the author's research team has filled several patents and scientific articles, contributing for Bosch technical roadmap in the inductive sensors. Also, considering its promising functional capabilities, the eddy currents technology presents several advantages over the traditional technologies, such as lower cost, as it uses common automotive components, does not require permanent magnets, and enables for a more compact solution. Cost is one of the most critical requirements in the automotive industry.

One of the critical aspects identified during the development of a sensor based on planar coils is the design of these coils. Defining the geometry and calculating the inductance of this type of coils can be quite challenging and time-consuming considering its requirements. Currently, for irregular geometry coils, FEM simulations are used to calculate its inductance values and thus determine the sensor configuration. For regular geometries there are some generic expressions that can be used, however, they are limited to some configurations. Thus, it becomes relevant to optimize this process to potentiate the appliance of sensors with planar coils in the APS market. Therefore, a review of the methods that are currently being used to calculate the inductances of planar coils was made. Each method was analyzed, identifying the conditions under which they can be used and in which scenarios their results are degraded. This review was done according to the description of the RM2 methodology, answering the research questions RQ1 (What are the methods more adequate to calculate self and mutual inductances of planar coils for an eddy current based automotive sensor?) and RQ2 (How can the performance of the several planar coil designing methodologies be compared?), and enabling the achievement of O2 (Review the current approaches to

simulate and calculate inductance of planar coils).

With the review of analytical methods for calculating self and mutual inductances, the Grover's method was identified and considered the most accurate. However, it is not usually used due to the complexity of its implementation. No tool uses this method to calculate the inductance of planar coils of arbitrary geometry, since it is time consuming and inappropriate to develop a model from scratch for each calculation of the inductance of a coil. Thus, an analytical model for calculating self and mutual inductance for multi-layer planar coils was developed and implemented based on this method, implementing the research methodology described in RM3. With the developed model it is possible to calculate not only the inductance of planar coils of arbitrary geometry with one or more layers but also the inductance of a coil covered by a conductive target. Thus achieving this thesis' objectives O3 (Implement an analytical method to calculate self and mutual inductance of planar coils) and O5 (Implement the best approach of the developed method to the calculation of the interference of a target on the coil's inductance).

The validation of the developed analytical model was carried out accordingly to the methodology described in RM4, while answering the research questions RQ2 and RQ3 (What are the main challenges in the designing phase of an eddy current based automotive position sensor and how can they be targeted?). The model developed was compared with the generic expressions identified in the state-of-the-art, the FEM simulations, and the experimental measurements made to a set of multi-layer planar coils, described in Chapter 3. Thus, the performance of the model in calculating the inductances of planar coils with and without the presence of a conductive target was validated, as described in Chapter 3. In Sections 3.1, 3.2, and 3.3, the results obtained by the various models and equations for regular coils of one and two layers, and for one layer coils in the presence of a conductive target, were compared. For the inductance values of regular coils of one and two layers, it was concluded that the developed model is well aligned with the standard existing current solutions (analytical models and FEM simulations). Although, with the advantage of calculating the results faster, being more intuitively, without any kind of limitation regarding the geometry of the coil, and without using a simulation program. For the inductance values of planar coils in the presence of a conductive target, the results are consistent with those obtained from the FEM simulations, since there are no analytical models for these scenarios. In some coil designs, where the number of turns increases and the internal radius decreases, the errors of the model increase when compared to FEM and experimental. This is because of the target approximation that was used, which considers the target as a one-turn coil. In these particular cases, the distribution of induced currents is more concentrated in the interior of the coil and not so much in the exterior, being the approximation not so adequate. The same happens when the distance between the target and the coil is lower than

0.75 mm. The currents will also concentrate more at the center of the coil and less in the extremities. This validation process allowed the achievement of objectives O4 (Evaluate the proposed tool within the existing state-of-the-art tools), O5 and O6 (Assess the proposed tool with FEM simulations and experimental measurements, for the case where planar coils are in the presence of a conductive target).

With the developed analytical model validated, its application in the design of an automotive sensor based on eddy currents, accordingly to RM5 was carried out. The main goal was to establish how the model stands out from the approach currently used in the design of planar coils for an automotive APS. The differential angular position sensor that is being developed in the research laboratory, in the partnership with Bosch Car Multimedia, was selected. Chapter 4 describes the sensor operation, and how the FEM simulations, the implementation of the developed model and the experimental measurements were made. The analysis and comparison betweeen the values obtained by the developed model, FEM simulations, and with the experimental measurements, for the case of planar coils (inner and outer) in the presence of two electrical grounded planes, proved to be in agreement and within tolerances, as described in Chapter 4. In the case of coils in the presence of a rotating conductive target, it is noted that the inductances obtained by the developed model and FEM simulations have a good match. The maximum error between the developed model and the FEM is below 7%, for both types of coils. By comparing these values with the experimental measurements, it is possible to notice that the developed model is closer to the real one for the case of the outer pair of coils, and the FEM simulations for the inner pair coils. This fact goes to the conclusion reached in the previous paragraph regarding the approach used for the target in the developed model. Nonetheless, the developed model has the advantage of being much faster and cheaper. Comparing the time that the approximate FEM model (used by the sensor development team) took, against that of the developed model, it took 33 times longer to get similar results. With this, the research question RQ4 was fully answered, and objective O7 (Compare the performance of the tool implemented with the currently used in the development of an automotive eddy current angular position sensor) was achieved.

In brief, there is no analytical toll in the state-of-the-art capable of calculating the inductance of coils in close proximity of conductive targets, with arbitrary geometry, in a fast way. This thesis analytical tool is capable to fill this state-of-the-art gap. As costs are a critical requirement in the automotive industry, the developed model presents an added value. This model calculates the coil inductance values (for the various scenarios) in a more efficient and cheaper way, without compromising the results precision. Thus, it is capable to replace the FEM tools that are currently being used during the designing phase of a sensor with planar coils based on eddy currents.

5.2 Future work

Taking into account the conclusions reached, an approach to be followed to improve the proposed model was identified. It was noticed that the model results deteriorate in cases where the current eddy density deviates from the geometric approximation used. Therefore, improving this approximation by considering the distribution of these currents should be explored. Figure 5.1 shows the inductance values for a pair of inner coils of the use case sensor. It is possible to visualize the values calculated by the model as presented in the document and with a correction. As in this type of coils, the magnetic field is concentrated at the coil's center, and these coils are smaller, the compensation factor used in Equation 3.5 turns out not to be the most adequate. By removing this factor, the difference between the errors of the proposed model and those measured experimentally and simulated via FEM is noticeable. The average error decreased from 8.38% to 1.34%.

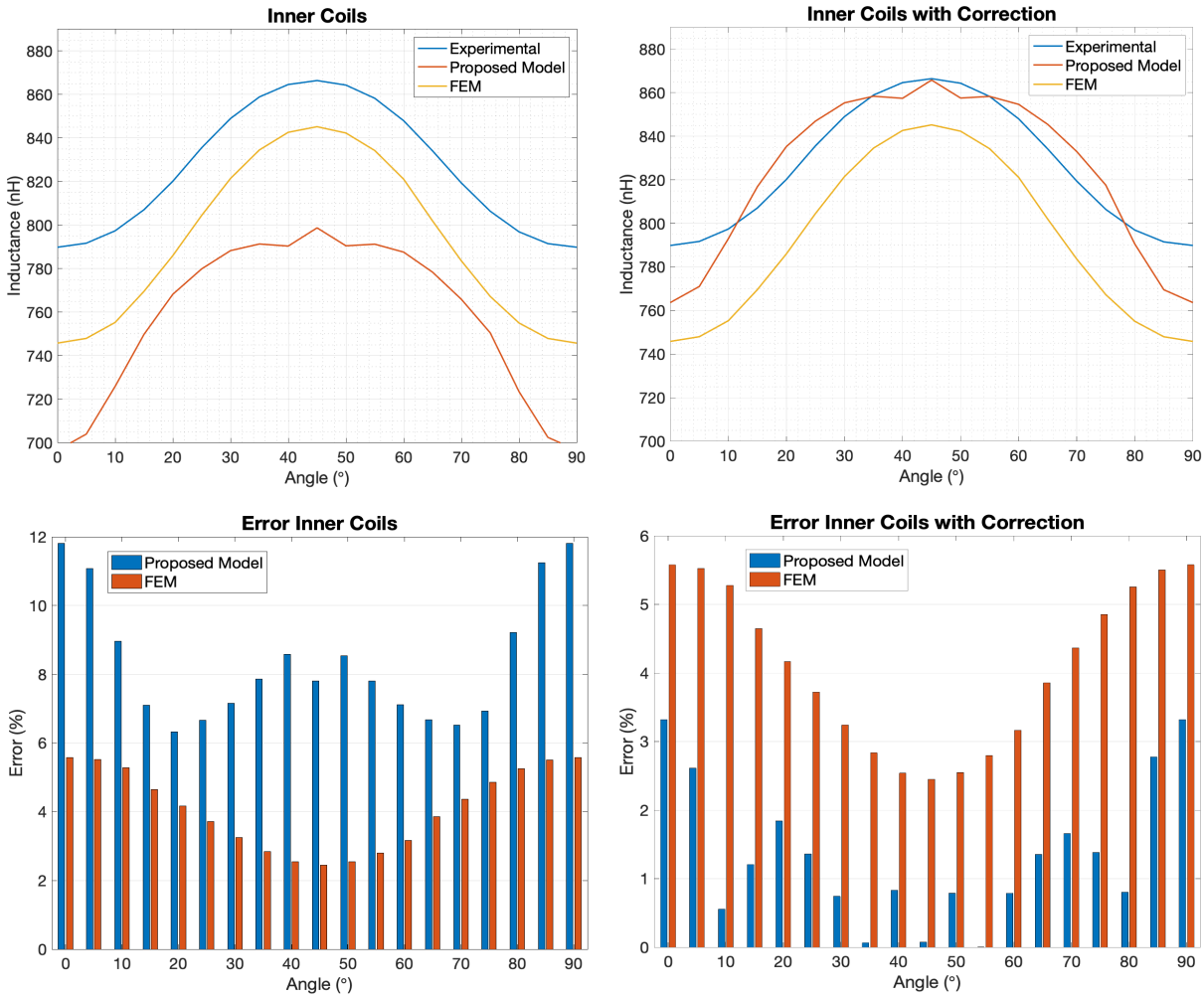

Figure 5.1: Graphics with the inductance values of a pair of inner coils for a target rotation from 0° to 90°. In the left side the data with the proposed model as presented in the document. In the right side the data with the modification proposed for improving the developed model.

Another improvement that can be made in the developed tool is the integration of an automatic tool for the designing of coils. Instead of importing the geometry, the user could define the coil parameters from a graphical interface. It would be possible to configure the coil shape, number of turns, wire width and thickness, space between turns, number of coil layers, and space between layers. For more dedicated geometries, it could also allow drawing the coil. In addition to designing the coil, the system could also create the scenario to be analyzed, such as e.g. two coils, or a multilayer coil in the presence of an conductive target. This new feature would make the developed tool even easier to use and completely independent from other software.

Appendix A

Use Case Inductance Graphs

This appendix shows the inductance graphs obtained for all the case studies defined in Table 3.1.

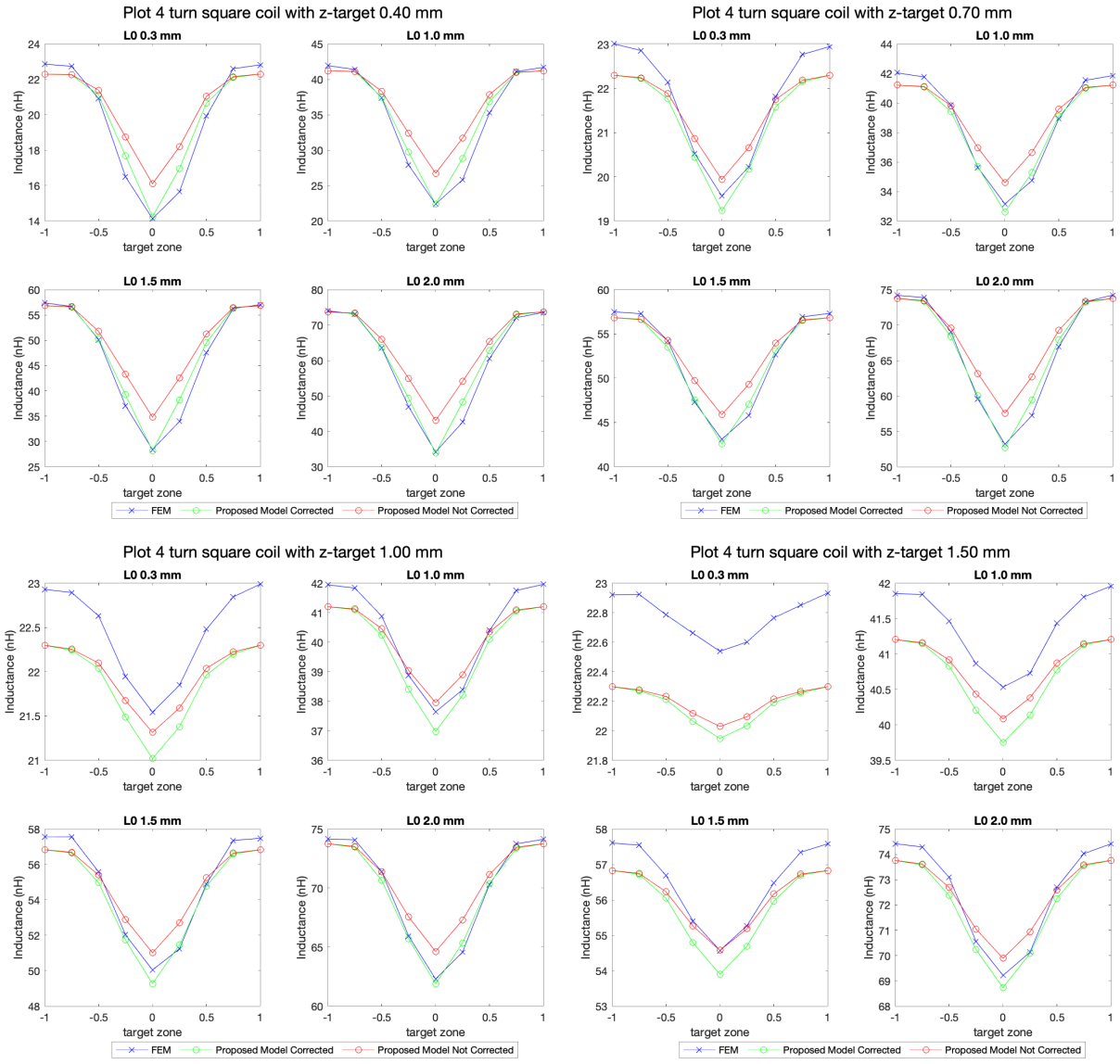

Figure A.1: Inductance values for a moving target over a 4-turn square coil for several configurations of l_0, y_{target}, and z_{target}.

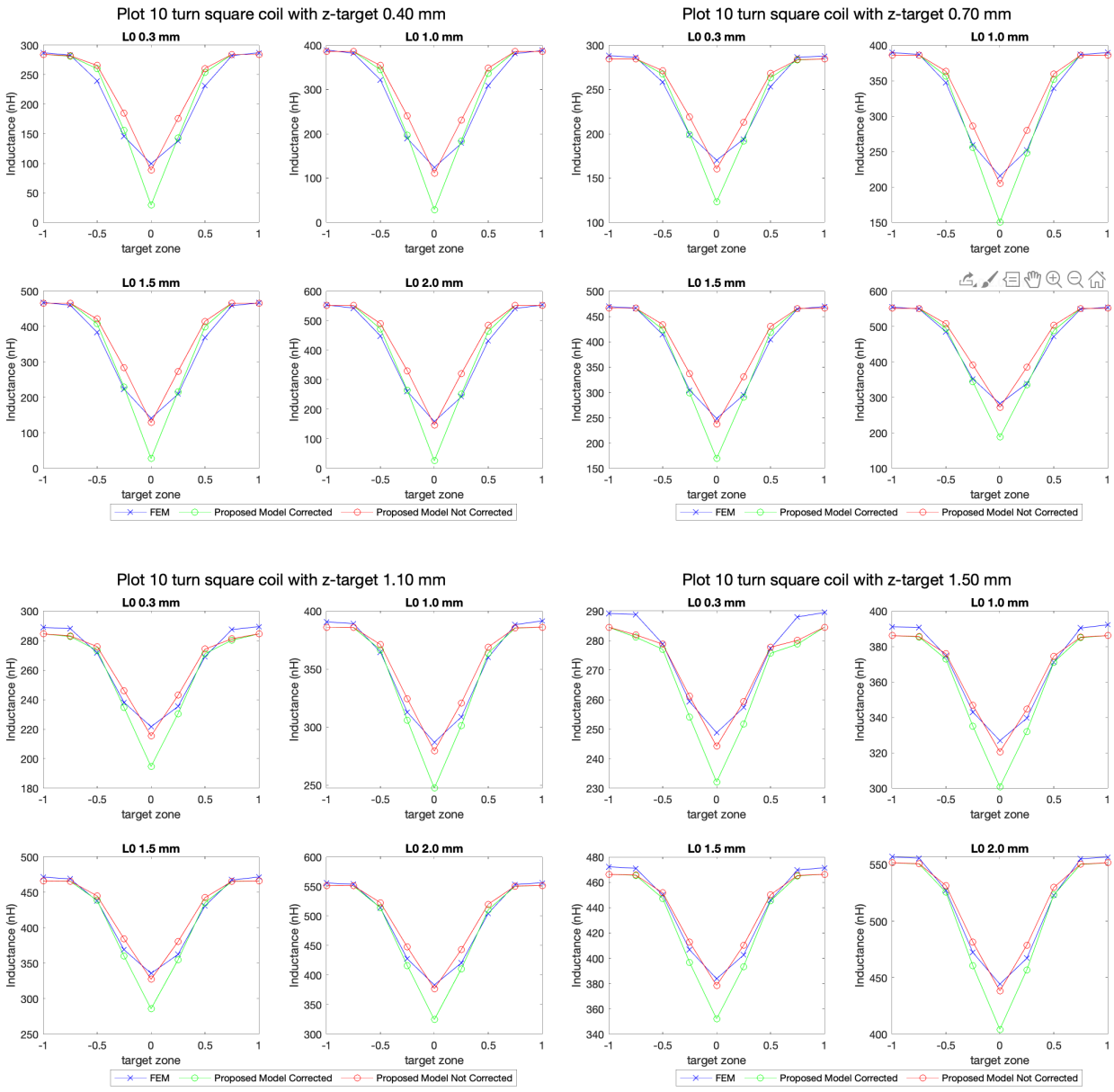

Figure A.2: Inductance values for a moving target over a 10-turn square coil for several configurations of l_0, y_{target}, and z_{target}.

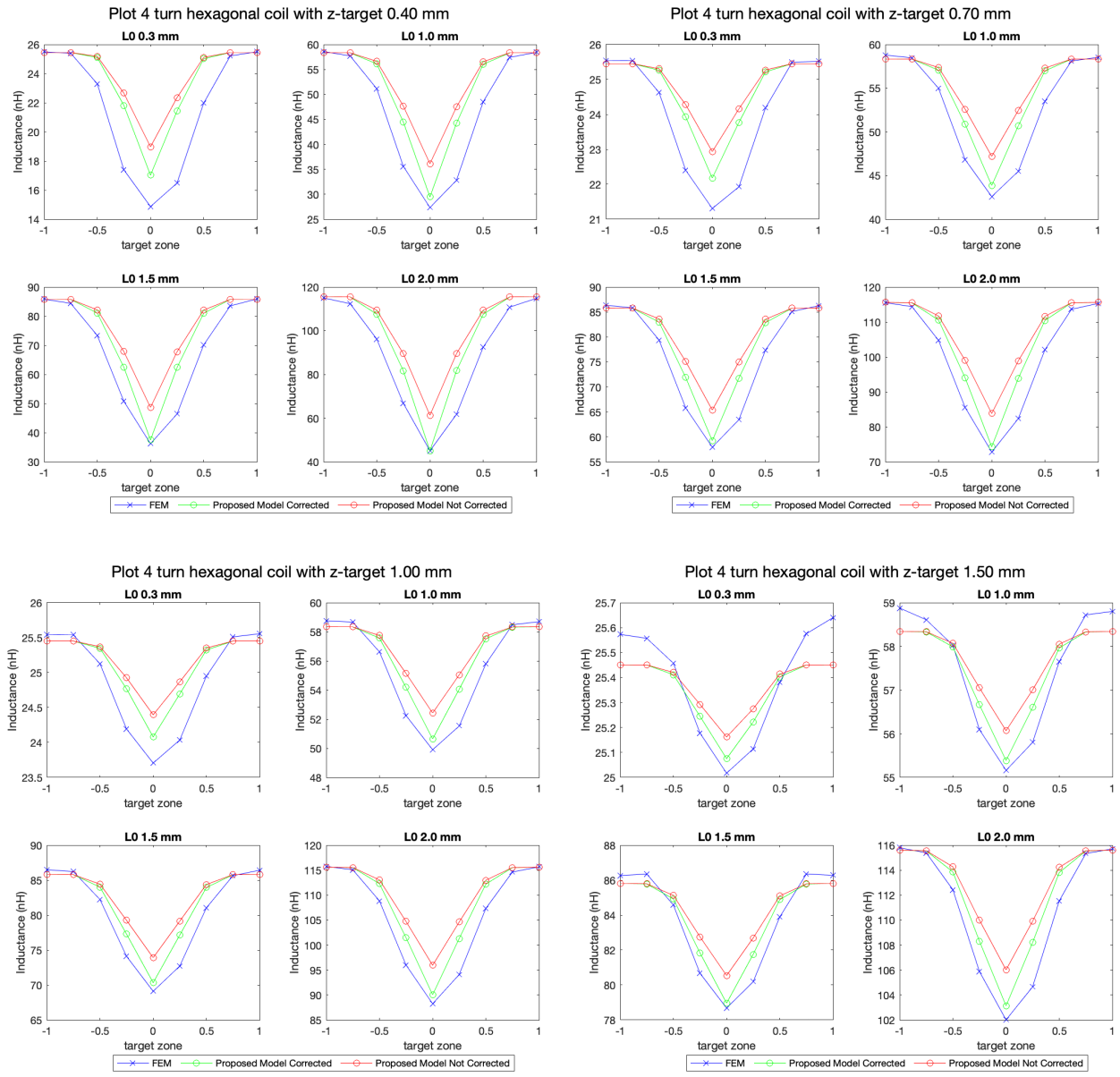

Figure A.3: Inductance values for a moving target over a 4-turn hexagonal coil for several configurations of l_0, y_{target}, and z_{target}.

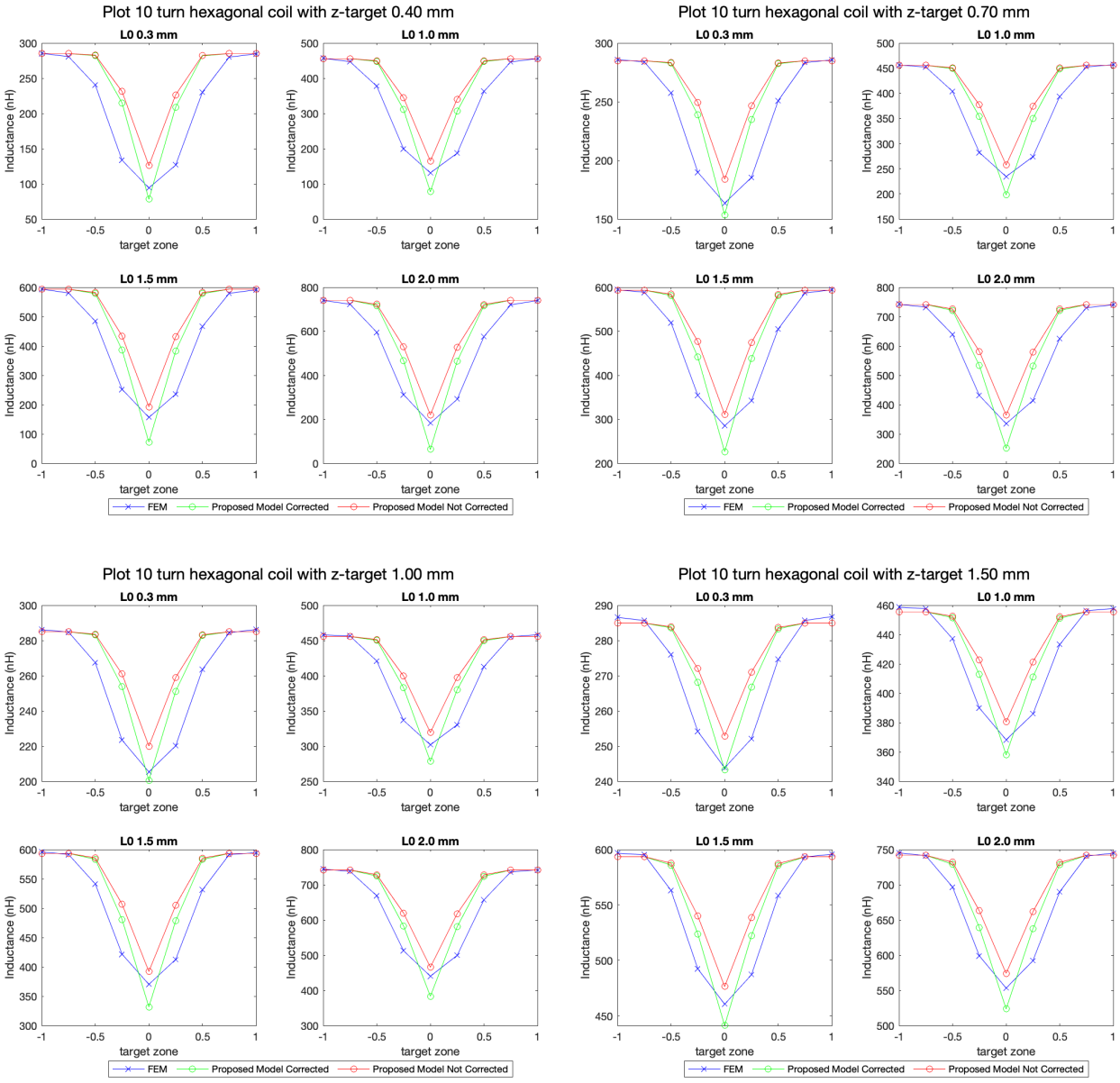

Figure A.4: Inductance values for a moving target over a 10-turn hexagonal coil for several configurations of l_0, y_{target}, and z_{target}.

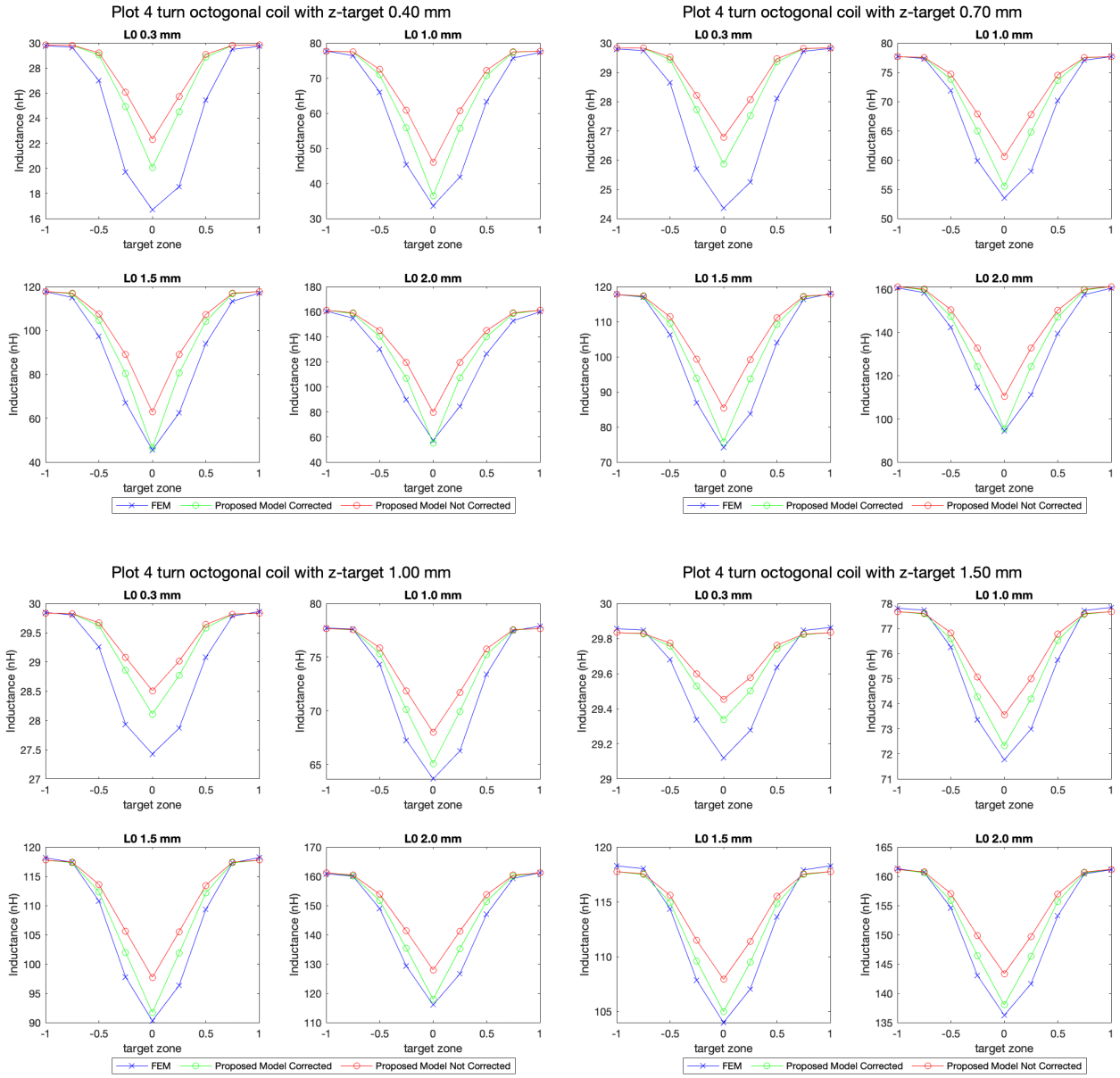

Figure A.5: Inductance values for a moving target over a 4-turn octagonal coil for several configurations of l_0, y_{target}, and z_{target}.

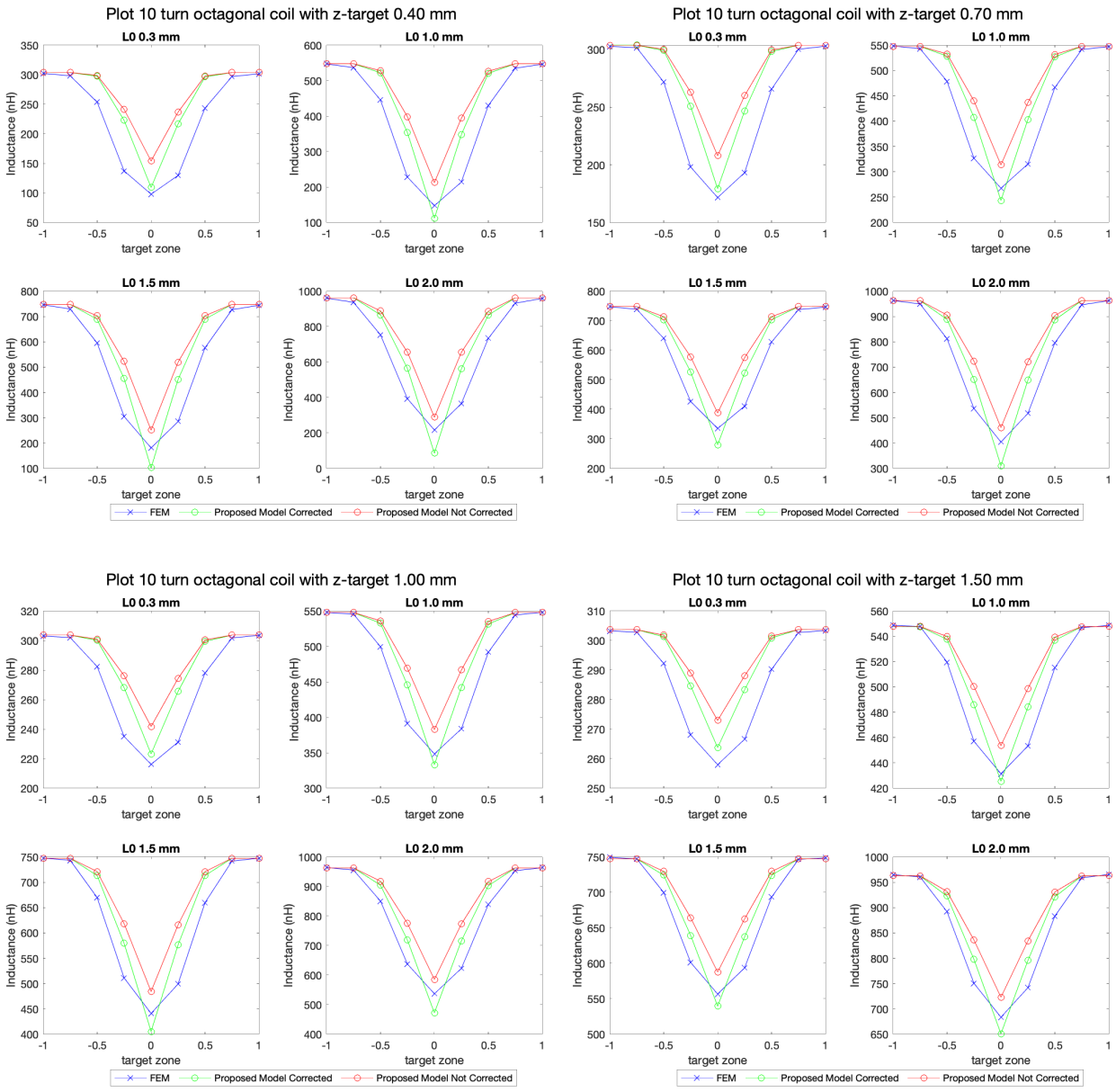

Figure A.6: Inductance values for a moving target over a 10-turn octagonal coil for several configurations of l_0, y_{target}, and z_{target}.

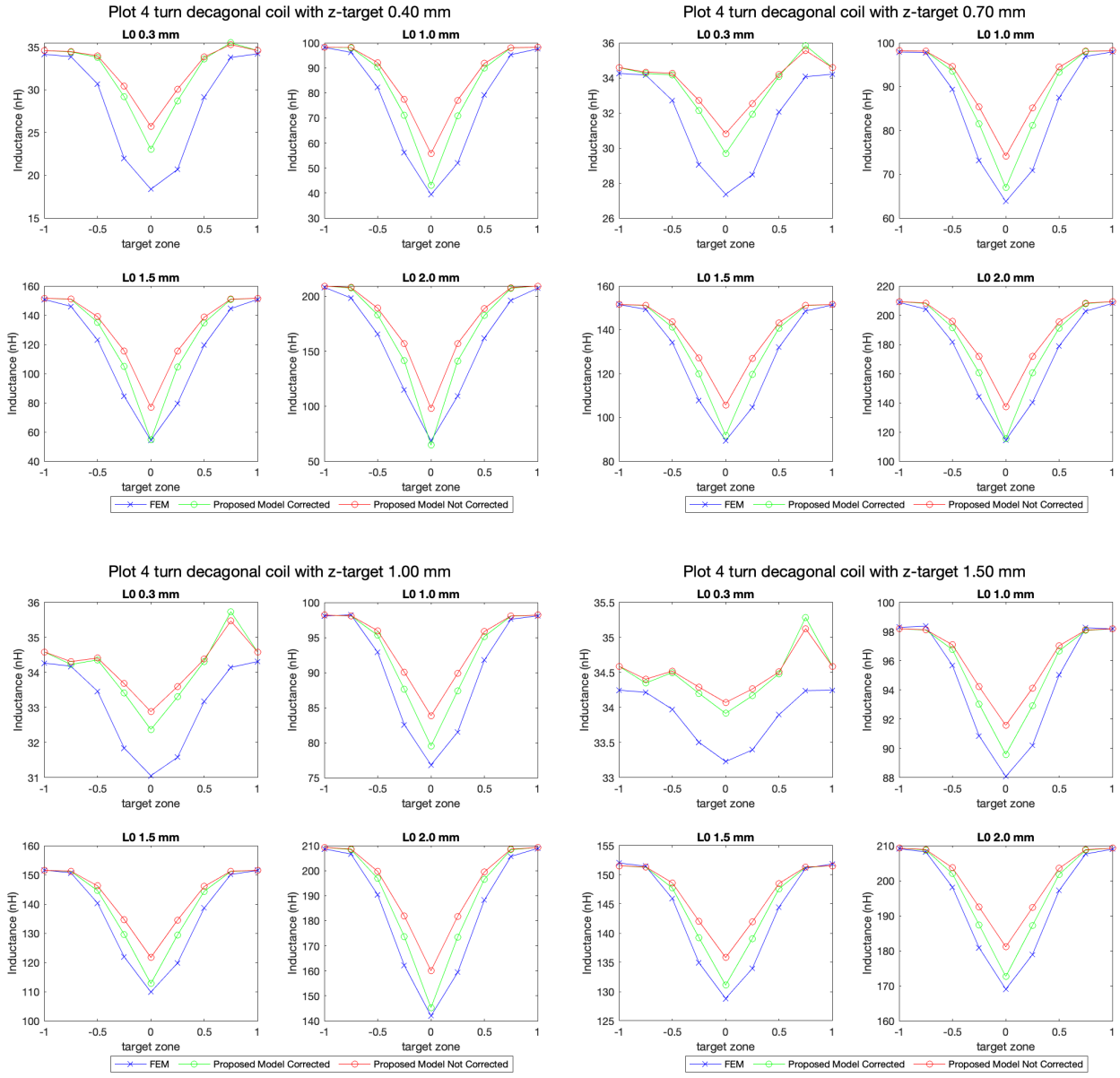

Figure A.7: Inductance values for a moving target over a 4-turn decagonal coil for several configurations of l_0, y_{target}, and z_{target}.

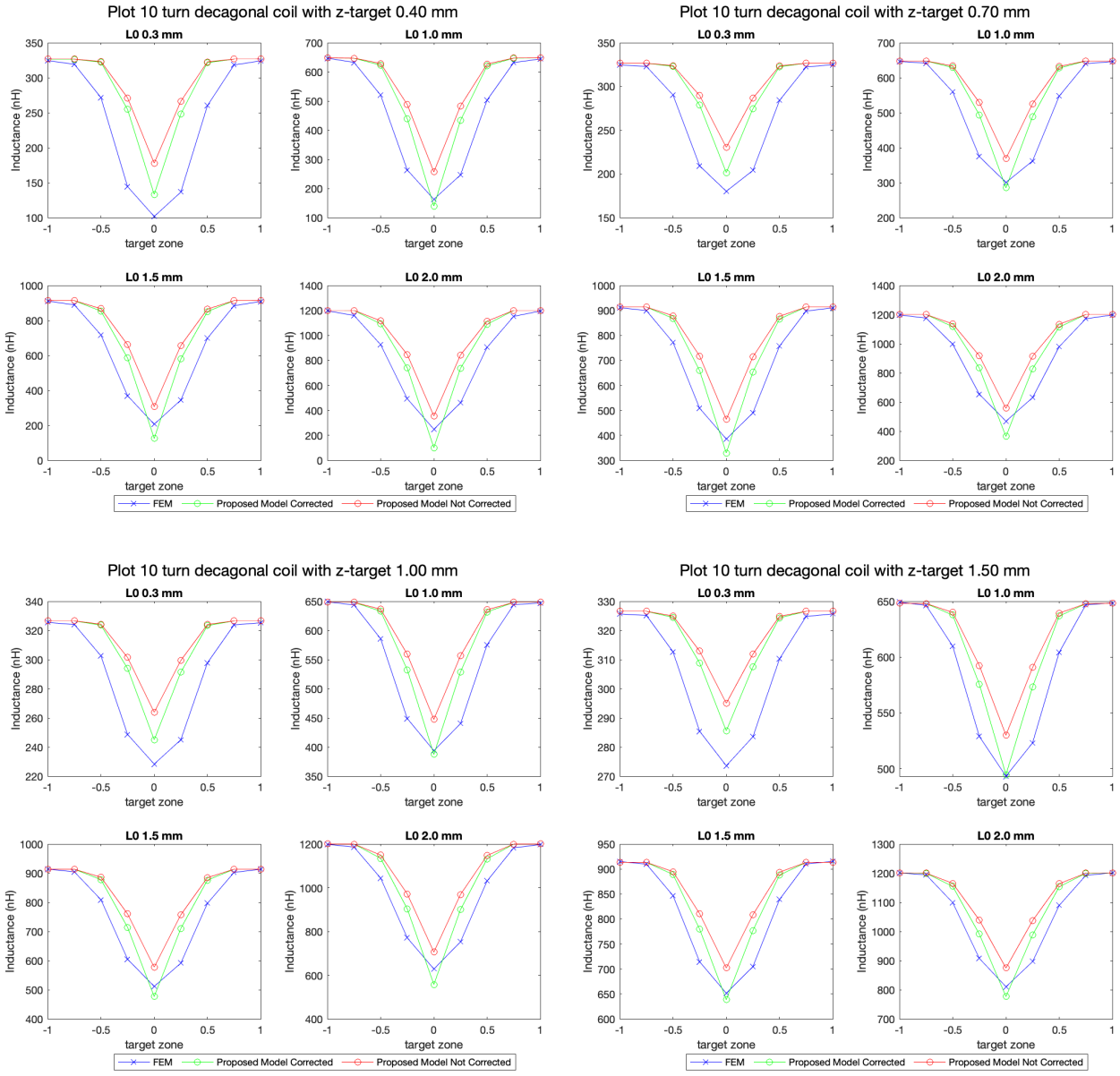

Figure A.8: Inductance values for a moving target over a 10-turn decagonal coil for several configurations of l_0, y_{target}, and z_{target}.

List of Publications

Journal Publications

1. A. Faria, L. Marques, C. Ferreira, F. Alves, and J. Cabral, “A Fast and Precise Tool for Multi-Layer Planar Coil Self-Inductance Calculation,” Sensors, vol. 21, no. 14, p. 4864, Jul. 2021. Under Approval:
2. A. Faria, L. Marques, L. Alves, F. Alves, and J. Cabral, “Analytical tool for optimization of position sensors based on eddy currents effect”, Sensors and Actuators, A: Physical (under approval).

Conference Proceedings

1. A. Faria, J. Cabral, L. Marques, F. Alves, and J. Gaspar, “High precision, geometry independent analytical method for self-inductance calculation in planar coils”, in Proceedings of the 2021 22nd IEEE International Conference on Industrial Technology (ICIT), Valencia, 2021.

About the Author

Andreia Raquel Sampaio Faria was born in Porto, Portugal in 1992. She received her BSc and M.Sc. degree in Electronic Engineering from the University of Minho, Portugal, in 2013 and 2015, respectively. Her master project was integrated into a collaborative project between the University of Minho and Bosch Car Multimedia, Braga, named HMIExcel. After graduating she worked as a researcher on the next collaborative project between the University of Minho and Bosch, the Innov-Car Project, for a year. In 2017, she started doing a PhD in Leaders for Technical Industries (LTI), from the MIT Portugal program, at the university where she graduated. Her research focus has been on the study and improvement of the designing process of angular position sensors based on eddy currents.